Title
Interaction between surface and atmosphere in a convective boundary layer

Author
Garai, Anirban

Publication Date
2013

UNIVERSITY OF CALIFORNIA, SAN DIEGO

Interaction between surface and atmosphere in a convective boundary layer

A dissertation submitted in partial satisfaction of the requirements for the degree Doctor of Philosophy

in

Engineering Sciences (Mechanical Engineering)

by

Anirban Garai

Committee in charge:

Professor Jan Kleissl, Chair
Professor Laurence Armi
Professor Keiko Nomura
Professor Sutanu Sarkar
Professor William Young

2013

The dissertation of Anirban Garai is approved, and it is acceptable in quality and form for publication on microfilm and electronically:

Chair

University of California, San Diego

2013

DEDICATION

Dedicated to my late grandfather, wife, parents and in-laws.

TABLE OF CONTENTS

LIST OF FIGURES

LIST OF TABLES

ACKNOWLEDGEMENTS

I would like to acknowledge Professor Jan Kleissl, as my advisor, for his guidance and support throughout my graduate studies. I am also thankful to my PhD committee members, Professor Sutanu Sarkar, Professor Laurence Armi, Professor William Young, and Professor Keiko Nomura, for their valuable suggestions during the preparation of different publications and dissertation.

I would like to thank my colleagues at Professor Kleissl's research laboratory, Solar resource assessment and forecasting laboratory, for a friendly and supportive atmosphere in the group. Special thanks to Dr. Long Sun, Dr. Matthew Lave, Neda Yaghoobian, Anthony Dominguez, Anders Nottrott, Patrick Mathiesen, Chi Chow for their valuable help during my PhD study.

I would like to show my appreciation to Boundary Layer Late Afternoon and Sunset Turbulence field campaign organizers, without them first part of my dissertation could not be finished. Special thanks to Professor Eric Pardyjak, Professor Marie Lothon, Professor Fabienne Lohou, Professor Fredérique Said, Professor Fabien Gibert, Professor Arnold Moene, Professor Gert-Jan Steeneveld, Professor Oscar Hartogensis, Professor Carlos Yagüe for field assistance, data sharing and discussion. I would also like to acknowledge the help of Daniel Alexander, Solene Derrien, Anneke Van de Boer, Carlos Román Cascón, Mariano Sastre Marugán during the field campaign.

For the second part of my dissertation, I am thankful to the NCAR-Wyoming Supercomputing Center provided by the National Science Foundation and the State of Wyoming and supported by National Center for Atmospheric Research's (NCAR) Computational and Information Systems Laboratory; and San Diego Supercomputer

Center provided by Extreme Science and Engineering Discovery Environment (XSEDE) and supported by National Science Foundation grant number OCI-1053575 for the computing resources.

The financial support was provided by NASA through a New Investigator Program award.

Finally, I thank my parents, my wife and in-laws for their support, sacrifice and patience during my doctoral study.

Content of Chapter III has been published in Garai A, & Kleissl J, 2011, Air and surface temperature coupling in the convective atmospheric boundary layer. *J. Atm. Sci.*, **68**, 2945-2954. The dissertation author was primary investigator and author of this paper.

Content of Chapter IV has been published in Garai A, & Kleissl J, 2013, Interaction between coherent structures and surface temperature and its effect on ground heat flux in an unstably stratified boundary layer, *J. Turbul.*, in press. The dissertation author was primary investigator and author of this paper.

Content of Chapter V has been published in Garai A, Pardyjak E, Steeneveld G-J, & Kleissl J, 2013, Surface temperature and surface-layer turbulence in a convective boundary layer, *Boundary-Layer Meteorol.*, **148**, 51-72. The dissertation/thesis author was primary investigator and author of this paper.

Content of Chapter VI is being under consideration for publication in Garai A, Kleissl J & Sarkar S, 2013, Heat transfer in a convectively unstable turbulent channel flow with solid conduction, *J. Fluid Mech.* The dissertation/thesis author was primary investigator and author of this paper.

VITA

2009	B. Tech. in Mechanical Engineering, Indian Institute of Technology Kharagpur, India
2009	M. Tech. in Thermal, Energy and Environmental Engineering, Indian Institute of Technology Kharagpur, India
2013	Ph. D. in Engineering Sciences (Mechanical Engineering), University of California San Diego, USA.

JOURNAL ARTICLES

8. **A Garai**, J Kleissl & S Sarkar; Heat transfer in an unstably stratified turbulent channel flow with solid conduction. *J. Fluid Mech.*, (under preparation).

7. **A Garai** & J Kleissl; Interaction between coherent structures and surface temperature and its effect on ground heat flux in an unstably stratified boundary layer. *J. Turbul.*, (in press).

6. **A Garai**, E Pardyjak, GJ Steeneveld & J Kleissl; Surface temperature and surface-layer turbulence in a convective boundary layer. *Boundary-Layer Meteorol.* (2013), 148:51-72.

5. **A Garai** & J Kleissl; Air and surface temperature coupling in the convective boundary layer. *J. Atmos. Sci.* (2011), 68:2945-2954.

4. **A Garai**, J Kleissl & SG Llewellyn Smith; Estimation of biomass heat storage using thermal infrared imagery: application to a walnut orchard. *Boundary-Layer Meteorol.* (2010), 137:333-342.

3. **A Garai** & S Chakraborty; Steric effect and slip-modulated energy transfer in narrow fluidic channels with finite aspect ratios. *Electrophoresis* (2010), 31:843-849.

2. **A Garai** & S Chakraborty; Micro-scale thermo-fluidic transport in two immiscible liquid layers subject to combined electroosmotic and pressure-driven transport. *Int. J. Heat Mass Transfer* (2009), 52:2660-2666.

1. S Bhattacharyya, **A Garai** & J Sarkar; Thermodynamic analysis and optimization of a novel N_2O-CO_2 cascade system for refrigeration and heating. *Int. J. Refrigeration* (2009), 32:1077-1084.

ABSTRACT OF THE DISSERTATION

Interaction between surface and atmosphere in a convective boundary layer

by

Anirban Garai

Doctor of Philosophy in Engineering Sciences (Mechanical Engineering)

University of California, San Diego, 2013

Professor Jan Kleissl, Chair

Solar heating of the surface causes the near surface air to warm up and with sufficient buoyancy it ascends through the atmosphere as surface-layer plumes and thermals. The cold fluid from the upper part of the boundary layer descends as downdrafts. The downdrafts and thermals form streamwise roll vortices. All these turbulent coherent structures are important because they contribute most of the momentum and heat transport. While these structures have been studied in depth, their imprint on the surface through energy budget in a convective atmospheric boundary layer has received little attention. The main objective of the present study is to examine the turbulence-induced surface temperature fluctuations for different surface properties and stratification.

Experiments were performed to measure atmospheric turbulence using sonic anemometers, fine wire thermocouples and LIDAR; and surface temperature using an infra-red camera over grass and artificial turf fields. The surface temperature fluctuations were found to be highly correlated to the turbulent coherent structures and follow the processes postulated in the surface renewal theory. The spatio-temporal scales and advection speed of the surface temperature fluctuation were found to match with those of turbulent coherent structures.

A parametric direct numerical simulation (DNS) study was then performed by solving the solid-fluid heat transport mechanism numerically for varying solid thermal properties, solid thickness and strength of stratification. Even though there were large differences in the friction Reynolds and Richardson numbers between the experiments and numerical simulations, similar turbulent characteristics were observed. The ejection (sweep) events tend to be aligned with the streamwise direction to form roll vortices with unstable stratification. The solid-fluid interfacial temperature fluctuations increase with the decreases in solid thermal inertia; and with the increase in solid thickness to attain a constant value for a sufficiently thick solid. The temperature fluctuation changes from a Gaussian distribution near the wall to a positively skewed distribution away from the wall. The turbulent temperature fluctuations influence the solid interfacial temperature by thermal conduction only.

These studies provided unique insights into the solid-fluid coupled heat transport in low and high Reynolds number flows. This turbulence induced surface temperature fluctuation can influence the performances of several satellite remote sensing models.

Chapter I

Introduction

The Earth atmosphere consists of gases arranged in layers with different stratification and is retained by gravity. The lowest part of it is known as troposphere, extending, on average, from the surface to 9 km at the poles to 17 km at the equator. The lowest part of the troposphere, varying in vertical extent from 100 m to 2000 m is affected by surface forcings such as surface topography and heating, and is known as the atmospheric boundary layer (ABL). The remainder of the troposphere is known as the free atmosphere. The ABL and the free atmosphere are usually separated by a capping inversion, across which potential temperature, and sometimes even temperature increase strongly with height. The difference in the diurnal temperature variation of the land surface versus the less variable air temperature in the ABL characterizes the ABL to be thermally stable or unstable.

I.1 Convective boundary layer

During the daytime, solar heating of the land surface causes convection to be the dominant source of turbulence, larger than turbulence production through the wind shear. These conditions in the ABL are known as convective boundary layer (CBL). Close to the sunset the ground cools, causing turbulence in the CBL to decay and eventually the ABL becomes stable. In this thesis our primary interest is on the behaviour of CBL.

I.1.1 Atmospheric surface layer

Regardless whether the ABL is convective or stable, in the bottom 10% or so of the boundary layer the turbulent fluxes and stresses vary by less than 10% and this “layer” is defined as the atmospheric surface layer (ASL). The ASL in a CBL is characterized by a decrease in temperature and moisture with height and strong wind shear. The turbulent fluxes of momentum, heat and mass can be well described by the Monin-Obukhov similarity theory and the wind, temperature and moisture can be described by a log profile with a stability correction. The dominant turbulent structures in the ASL of a convectively driven boundary layer are plumes. Plumes are coherent structures of rising warm air having diameters and depths on the order of the ASL height. These plumes occupy about 40% of the horizontal area, with weak cool downdrafts between them and are advected horizontally with mean wind speed averaged over depth

(Kaimal & Businger 1970; Wilczak & Tillman 1980). Thus when a plume moves past a measurement tower, the resulting temperature trace shows a characteristic ramp structure or sawtooth shape (Figure I.1a).

I.1.2 Surface renewal method

The temperature ramp structure can be explained by the surface renewal (SR) process. In the SR process (Figure I.1b) a cold air parcel approaches the ground during a sweep event. As it stays in contact with the ground, heat is transferred from the ground to the air parcel, until it has sufficient buoyant force. The heated air parcel then ascends during the ejection event. The heat flux from the surface to air is large during ejection and sweep events, but small while the air parcel is near the surface. This heat flux variation is manifested in the surface temperature by warm and cold coherent structures.

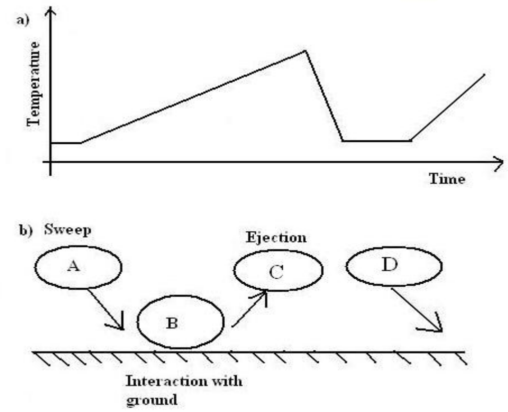

Figure I.1. Schematic of a) the temperature trace when a plume crosses over measurement tower and b) the idealized surface renewal process.

I.1.3 Mixed layer

Above the ASL, in the mixed layer, the plumes combine to form thermals which have larger length scales, of the order of the ABL. These thermals cause intense vertical mixing, resulting in constant wind, and potential temperature and moisture profiles in the mixed layer. Adiabatic buoyant thermals gain momentum as they pass through the mixed layer. Upon reaching the warmer free atmosphere, they overshoot a short distance because of their momentum. During this overshoot a sheet of warm free atmosphere is entrained into the mixed layer. The mixed layer grows because of this entrainment process. Thus the top of the mixed layer is often defined as the location of most negative heat flux, which is near the middle of the entrainment zone. The strength of mixing in the mixed layer also depends on strength of buoyancy and shear. Since convective anisotropy causes vertical motion while shear anisotropy causes horizontal motion buoyancy will cause a more uniformly (vertically) mixed layer.

I.1.4 Surface temperature fluctuations

These plumes and thermals in a CBL cause high frequency surface temperature variations, depending on the ground thermal property, distinct from the solar radiation driven diurnal cycle. Ground with higher thermal inertia homogenizes the high frequency surface temperature variation, through thermal diffusion and storage process. Many videos of thermal images of a homogeneous surface proof the existence of such surface temperature fluctuations. This kind of surface temperature variation deteriorates the representativeness of satellite surface temperature retrievals; rather than capturing the desired surface temperature that is a function of soil properties only, the satellite measures a snapshot of surface temperature with a turbulence signal superimposed. Just like with measurements in a fluid the surface temperature would have to be measured and averaged over the integral time scale Moreover, the evolution of surface temperature affects the energy and water balance and stability of the atmosphere.

I.2 Literature review

I.2.1 Laboratory observations

Flow visualization techniques employed by Kline et al. (1967); Corino & Brodkey (1969) of a neutral turbulent boundary layer reveal that, it consists of streamwise oriented elongated low speed fluid streaks (1000 viscous lengths in the streamwise direction and 100 viscous lengths apart in the spanwise direction). As these low speed streaks migrate away from the wall they show signs of oscillation and breakup in the buffer region. This phenomenon is known as “burst” or “ejection”. Similarly high speed fluid outside the boundary layer is entrained into the low speed region, which is known as “sweep”. These events are the largest contributors to the Reynolds stress and can be characterized by the streamwise or quasistreamwise vortices. An experiment by Head & Bandyopadhyay (1981) proofs the existence of the streamwise vortices near the wall region. Most often they are characterized by horseshoe or hairpin vortices which exhibit a slope angle of 40-50^0 versus the horizontal in streamwise direction (this angle is consistent with the principal strain direction). Outer layer flow structures move over the bulges created by the hairpin vortices and penetrate deep into the boundary layer at an angle of $\sim 20^0$. The ejection event occurs in between the counter rotating legs of the horseshoe vortices while bulges at the outer edge of the boundary layer are collocated with the horseshoe head. Spanwise vortices can also be observed downstream of these streamwise vortices (Bernard & Wallace, 2002).

When fluid is heated from below, it experiences buoyant forces that can produce vigorous turbulent motion. Experiments on turbulent convection over a heated horizontal surface were analyzed by Thomas & Townsend (1957), Townsend (1959). They found that temperature fluctuations, gradients, and rate of change of temperature all show periodic activity, characterized by large fluctuations and alternating periods of quiescence. Both the proportion and frequency of these periodic activities decrease with distance from the surface. According to Howard (1966) these periodic processes consist of a conductive phase, followed by a break-off and mixing phase. At the beginning of conductive phase the cold fluid adjacent to heated plate is heated up. This heating process continues until the corresponding Rayleigh number exceeds a critical value; after that the layer becomes unstable and breaks up. This theory was validated by the experiment by Sparrow et al. (1970). They found that these periodic activities are caused by appearance of the mushroom-like structures of hot fluid ascending through the environment over the surface, known as thermals.

Deardorff et al. (1969) studied the non-steady penetrative convection in water in a circular cylinder of diameter 0.548 m and height 0.355 m. The experiment was initiated with zero velocity and a continuous, almost linear temperature increase with height. Thermal convection was then initiated by replacing cool water near the lower boundary with warm water. Results show the horizontally averaged temperature remains almost constant with height below the inversion base, undergoes a slight cooling just above the inversion base, and then increases with height above the inversion height. This cooling is related to downward heat transport at the inversion base, which is only about 1.5% of the vertically integrated upward flux. Similar experiments were also carried out by Willis &

Deardorff (1974, 1979), and Deardorff & Willis (1985) in a convection chamber with length of 1.14 m, width of 1.22 m and height of 0.76 m, and average mixed layer height of 0.18 m. These studies showed that statistics of the fluctuations scale with inversion height, convection velocity and temperature scales as predicted by Deardorff (1970). Flow visualization reveals that at small heights the dominant pattern are irregular open cells with dimension of 1.2 times the inversion height and near the surface smaller scale convection features are superimposed on these open cells. The major limitation of these studies was the small aspect ratio of the convection tank, which affect what of? the flow statistics and features.

Hetsroni & Rozenblit (1994); Kowalewski et al. (2000); Hetsroni et al. (2001); Kowalewski et al. (2003); Gurka et al. (2004) experimentally studied the evolution of surface temperature due to turbulent motions in neutrally stratified channel and open channel flows using infra-red imagery and particle image velocimetry (PIV). Infra-red imagery of the surface temperature reveals warm and cold streaky like structures corresponding to the low and high momentum fluid region observed using the PIV measurements.

For turbulent convection, Rayleigh scaling law is not applicable since it depends on the molecular properties. Townsend (1959) and Deardorff (1970) proposed two alternative scaling laws. Near the boundary in the conduction layer vertical turbulent motion will follow conduction scaling based on thermal diffusivity, thermal expansion coefficient and heat flux, whereas far from boundary vertical turbulent motion will scale with the convective scale based on thermal expansion coefficient, heat flux and boundary layer depth. These two scaling variables are related to each other by the turbulent Peclet number. Adrian et al. (1986) performed an unsteady convection experiment with water in a 1.4 x 1.5 m horizontal cross-sectioned and 0.2 m high tank electrically heated from below. Results from the experiment proofed the validity of the two different scaling laws.

I.2.2 Atmospheric observations

The CBL is dominated by the convection in a region sandwiched between a relatively thin shear dominated layer above the ground and the capping inversion. The cloud structures can often be correlated to coherent structures such as roll vortices (Etling & Brown 1993; Young et al. 2002) in the CBL. Satellite observations show that the aspect ratio (ratio between crosswind length and inversion height) of these cloud structures, which appear as streamwise streaks, is often in the range of 4-6. Aircraft observations like LeMone (1973, 1976); Kaimal (1978); Lenschow & Boba Stankov (1986); Young (1987, 1988a,b); Mahrt (1991) etc. reveal that the cloud streaks are only present in moderately unstable conditions ($-25 < \frac{z_i}{L} < -5$), where z_i and L are inversion height and Obukhov length, respectively.

The most dominant coherent structures in the surface layer are the updrafts of warm buoyant air, commonly known as plumes and the downdrafts of cold air. Based on time series of velocity and temperature fluctuations and fluxes of heat and momentum measurements at the Kansas field site, Kaimal & Businger (1970) proposed a two-dimensional model for the plumes and dust devils. Using field measurements over a flat site in northwestern Minnesota (Kaimal et al. 1976) and Colorado (Wilczak & Tillman 1980; Wilczak & Businger 1983) three-dimensional structures driven by convection in the surface layer and the ‘energetics’ of them over the entire boundary layer were studied.

Renno et al. (2004) found that dust devils are responsible for two to five times the average vertical flux of heat and dust.

Gao et al. (1989) observed organized turbulent structures with ram patterns in and above a deciduous forest canopy at an experimental site in Ontario, Canada. Similar flow structures were also reported by Paw U et al. (1992); Braaten et al. (1993); and Raupach et al. (1996). Utilizing the characteristics of these coherent structures Paw U et al. (1995); Snyder et al. (1996); Spano et al. (1997, 2000); Castellvi et al. (2002), Castellvi (2004) and Castellvi and Snyder (2009) proposed and validated the SR method to estimate sensible and latent heat flux over canopies given the statistics of high frequency temperature measurements.

In most of the cited studies reviewed so far, surface temperature is typically assumed to be constant and not measured. However, the variability in surface layer heat flux is expected to cause local variations in surface temperature. Paw U et al. (1992) observed surface temperature fluctuation of around 0.5^0 C over 2.6 m high maize crops under unstable condition. Katul et al. (1998) collected high frequency infrared temperature, atmospheric surface layer temperature and velocity over a 1 m high grass covered forest clearing. They found that turbulent velocity induces skin temperature fluctuation of > 2^0 C within a time interval of less than 1 min. Using wavelet spectra they also established that velocity–skin temperature interaction has a length scale of comparable to atmospheric boundary layer. Renno et al. (2004) also studied structures of plume and dust devil and reported temperature fluctuations over $2\text{-}4^0$ C over a desert area. Balick et al. (2003) studied transient spatial and temporal variation of surface temperature at the Mauna Loa caldera using thermal IR satellite data. They noticed non repetitive spatial patterns with 1–6^0 C magnitude. Vogt (2008); Christen & Voogt (2009, 2010) visualized the spatial surface temperature field over a bare field and in a suburban street canyon, Canada using 1 Hz thermal infrared imagery, respectively. Christen et al. (2012) reported different surface temperature standard deviations over different surfaces (metallic roofs > lawns > roads > building walls) for an urban measurement location. These studies show that atmospheric turbulence causes high frequency ground temperature fluctuations that cannot be explained by variability in solar irradiance alone.

Kustas et al. (2002) studied the heat and water exchange rates using the eddy covariance method at a riparian corridor along the Rio Grande. In their study they used remotely sensed radiometric surface temperature data to estimate partitioning of net radiation into sensible and latent heat flux. Their results indicate that instantaneous variations of sensible heat flux are strongly correlated with fluctuations in net radiation. Under near constant net radiation surface temperature perturbations also contribute to sensible heat flux variation, but the variations are an order of magnitude smaller.

I.2.3 Analytical model

Based on the flow visualizations of neutral and convective boundary layer, Liu & Businger (1975); Brutsaert (1975) proposed an analytical model for heat transfer in a turbulent atmosphere from rough and smooth surfaces. Brutsaert (1975) assumed that the eddies responsible for plume-like structures are of the order Kolmogorov scale for smooth walls and roughness height for rough walls. In these studies surface temperature was assumed to be constant and air temperature was not allowed to imprint itself on the surface. Balick et al. (2003) extended the Brutsaert-Liu-Businger surface renewal approach by allowing interaction between air and surface temperature. According to this model surface temperature (T_{sfc}) becomes

$$\frac{T_{sfc}-T_{g,0}}{T_{a,0}-T_{g,0}} = \frac{TAR}{1+TAR} \tag{1.1}$$

where $T_{g,0}$ and $T_{a,0}$ are ground and air temperature below and above and far away from? the surface-air interface at the start of a renewal event and $TAR = \frac{k_a}{k_g}\sqrt{\frac{\alpha_g}{\alpha_a}}$, (where k_g, k_a, α_g, α_a are thermal conductivity of ground and air and thermal diffusivity of ground and air respectively) is the surface conductance parameter that represents the diffusion assisted solid-fluid coupling for a given renewal event.

I.2.4 Numerical models

Large-eddy simulation (LES) is the most attractive method for simulating atmospheric turbulence. In LES, the large scale three dimensional unsteady turbulent field is calculated directly, whereas the effect of the small scales - the subgrid scale (SGS) - is modeled. The SGS fluxes are modeled using resolved scale variables, principles of Galilean invariance, and/or adding additional transport equations.

Schmidt & Schumann (1989) studied the coherent structures for purely CBL. Instantaneous flow fields show evidence of a spoke like pattern near the surface, which is generated due to flow convergence towards the updrafts. Small-scale plumes far from strong updrafts do not merge together and diffuse out while rising. The typical spacing of strong updrafts is 1 to 2 times the boundary layer height. Sykes & Henn (1989) performed LES of a purely convective and shear dominated convective ABL. The ratio between friction and convective velocity influences the structures in the CBL, rolls exists for a ratio greater than 0.35. Williams & Hacker (1993) studied the interactions between coherent eddies and found that near the surface a divergent flow pattern is created by downdraft arms of mixed layer roll vortex causing a convergence line of updraft for the mixed layer thermals. Moeng & Sullivan (1994) performed LES for different stability conditions (purely convective, purely shear and intermediate) of CBL. They found that a neutral boundary layer exhibits streaky like structures and a purely convection dominated boundary layer exhibits roll like structures. Glendening (1996) studied the structures for a shear dominated CBL with LES. Results show that linear rolls exist with lifetimes of around 8 hours and these rolls influence momentum and moisture fluxes near the mid, and heat flux near the top of the boundary layer. Both roll and non-roll fluxes are 2-3 times larger in ascending regions compared to descending regions. Wilson (1996) used the empirical orthogonal function (EOF) technique to study the coherent structures for weakly CBL. They found that the dominant structures are convective rolls and thermal modes and gravity waves in the capping inversion. Wilson & Wyngaard (1996) then studied energetics of the different EOF modes. They found that the main source of turbulent kinetic energy (TKE) for roll vortices is shear. Khanna & Brasseur (1998) performed LES of CBL for a wide range of stabilities. Roll vortices with horizontal scales of several boundary layer heights are prevalent for convection and streak like structures are prevalent for shear dominated CBLs. Streak-like structures near the surface are influenced by outer layer eddies. Warm fluid accumulates at the low speed streaks generating sheet like updrafts, which turn at the capping inversion giving streamwise roll vortices. In a sheared convective ABL Lin (2000) found that strong pressure transport is correlated with vertical structures embedded in the updraft.

For wall bounded flows, small scale turbulence is most energetic near the wall. Since LES can only resolve scales larger than the filter size, typically on the order of inertial length scale, the effect of near-wall small-scale anisotropic turbulence on the mean profiles are modeled using wall functions. Hence, albeit LES has been extensively used for simulating CBL and provides important information on coherent structures, LES is ill-suited to study the near-surface turbulence for wall bounded flows. The other alternate Direct Numerical Simulation (DNS) provides great details of the flow physics, but it is limited to small Reynolds number (*Re*) flows as the computing resource requirements scale as $Re^{2.7}$ (Pope, 2003).

Lida & Kasagi (1997) studied the unstable stratification effect on a turbulent channel flow using DNS. The friction Reynolds number and Grashoff number for the simulated flow was 150 and 0 - 4.8×10^6, respectively. They observed that the buoyant plumes are aligned in the streamwise direction while high vorticity regions and low speed streaks are concentrated in the thermal plume regions. The near wall coherent vortices are swept by the spanwise flow due to buoyant plumes for unstably stratified channel flow. Thus the near wall coherent structures are concentrated in a confined region near the wall. The Reynolds stress terms are transported by pressure diffusion and the strength of turbulent mixing is stronger than in neutrally stratified conditions.

Tiselj et al. (2001); and Hunt et al. (2003) studied the effect of solid conduction on the turbulent heat transport process for a neutrally stratified channel flow and

Rayleigh-Bérnard convection case using DNS. Tiselj et al. (2001) found that the solid-fluid heat transport process can be characterized by the thermal activity ratio (*TAR*) and the solid thickness. Hunt et al. (2003) observed different characteristics of thermal coherent structures (plumes, puffs etc.) depending on the solid thermal properties.

I.3 Objective

Although a considerable amount of study has been conducted on plumes, thermals, air temperature ramps and coherent turbulent structures of the convectively driven atmospheric boundary layer, only a limited number of studies focused on their effect on surface temperature. The main objectives of the present study are to:

i) study the solid-fluid heat transport mechanism in a CBL,

ii) study the effect of roll vortices, thermals, plumes, downdrafts and sweeps on the surface temperature,

iii) characterize the change in the scales of surface temperature fluctuations with stratification,

iv) quantify the effect of the surface temperature fluctuations on the surface heat flux.

I.4 Outline of the thesis

The thesis is organized as follows: Chapter II is dedicated to characterizing statistically stationary 30-min periods from different field experiments. Chapter II.3 describes the field experiments conducted and the meteorological conditions during the field experiments. Chapter II.5 then describes the data post-processing procedures employed to characterize the atmospheric turbulence. We then explain the observed surface temperature fluctuations in the context of the surface renewal method in Chapter III. Chapter IV presents the effect of surface layer turbulent structures (surface layer plumes and sweeps) and mixed layer turbulent structures (thermals and downdrafts) on the surface temperature as observed during the field experiments. In Chapter V we compare different surface layer turbulence parameters (length scales, advection speed, footprint function etc.) estimated using surface temperature data with the observed air turbulence data. The effect of the solid thermal properties and thickness on the surface temperature is then studied using direct numerical simulation method. Chapter VI describes the numerical technique and results from the DNSs of a solid coupled unstably stratified channel flow. A summary and conclusions are then presented in Chapter VII.

Chapter II

Field Experiments

II.1 Introduction

To study the air turbulence induced surface temperature fluctuations, a series of field experiments was conducted. The experimental sites were chosen carefully (homogeneity in roughness, irrigation water application, surface thermal properties) to ensure statistically homogeneous condition. The sites with near-by buildings, canyons, hills etc. will affect the turbulence shear production; hence will introduce length scales associated with the roughness. Also, heterogeneity in surface thermal properties and irrigation water application causes inhomogeneous surface temperature. Generally absence of vegetation (e.g. parking lot) makes the thermal admittance of the surface too low to detect temperature fluctuation. If the vegetation is too high, ‘honamis’ or ocean-wave-like motion of crops will occur and the resulting shading and varying solar incidence angle pattern will complicate the analysis (Finnigan 2010). Clear sky conditions are preferred during the experiments; otherwise variation in global horizontal irradiance (GHI) due to clouds will manifest itself on the surface temperature. The experimental sites were equipped with different atmospheric turbulent measurement sensors.

A short description of different sensors used in the field experiments is provided in the Chapter II.2. Chapter II.3 then describes different field experiments with the observed meteorological conditions. Different data post-processing techniques are described in the Chapter II.4. Finally details of the selected 30-min stationary periods, which will be used in following chapters, are then described in Chapter II.5.

II.2 Measurement sensors

A wide variety of sensors were employed to measure different atmospheric turbulent variables (wind velocity, temperature), atmospheric profiles (wind speed, potential temperature), atmospheric conditions (solar radiation, surface albedo), and surface temperature. The working principles of these different sensors are discussed in this section.

II.2.1 Infra-red camera

The surface temperature (T_s) was measured using an infra-red (IR) camera, FLIR A320 Thermacam, operated at 1 Hz frequency. The IR camera measures and images the emitted infra-red radiation (8 – 14 μm) from the object in 320 x 240 pixels with 25^0 x 18.8^0 field of view (FOV) or 45^0 x 33.8^0 FOV for wideangle configuration, which is a function of object temperature and emissivity. However the radiation measured by the camera also includes (i) radiation from the object surroundings, (ii) radiation from the atmosphere, and (iii) reflected radiations from the object. These radiations (known as atmospheric path radiance) are independent of object surface temperature and are present even without the object. This back ground radiation depends on the average atmospheric temperature, the direction of observation, the altitude and the meteorological conditions. For present filed experiments, we have assumed the surface emissivity (grass) to be 0.95, and neglected the atmospheric path radiance due to close proximity of the camera and surface. The reported accuracy of the camera is 0.08 K. A coordinate system transformation and interpolation was performed to map the original IR camera image to a Cartesian coordinate system with uniform resolution.

II.2.2 Sonic anemometers

The turbulent wind speeds (u, v and w for streamwise, spanwise and vertical velocity components) and air sonic temperature (T_a) were measured using Campbell Scientific sonic anemometer-thermometers (CSAT), uSonic-3 Scientific anemometer, Gillmaster pro 3D sonic anemometers. Sonic anemometer measures the wind speed using the Doppler shift effect. Its each axes pulses two ultrasonic signals in opposite directions to measure the wind speeds from the time of flight. Temperature is also estimated by measuring the speed of sound. As speed of sound depends on the air pressure, density and moisture content, the measured temperature by sonic anemometer is not the "true" air temperature. A coordinate system rotation was conducted to ensure that vertical velocity fluctuations were perpendicular to the mean flow by enforcing $|\langle w\rangle/M| < 1\%$ (angeled bracket denotes temporal averaging and M is the mean horizontal wind speed) following Wilczak et al. (2001) and to orient the CSAT winds to the IR-camera coordinate systems.

II.2.3 Finewire thermocouples

The "true" air temperature (T_a) was measured using finewire thermocouple (FWTC) at the same location of sonic anemometers. FWTC, consists of two dissimilar metals, generates voltage when subject to temperature difference across its junctions, following the Seebeck effect. Thus by measuring the generated voltage and using the calibration chart for a given pair of dissimilar metals, one can measure temperature of one junction, if the other junction temperature is known. For present study FWTCs of type E (Chromel-Constantan) and 12.7 μm diameters were used.

II.2.4 Windcube 200 LIDAR

The mixed layer wind speed was measured using a pulsed lidar system, Windcube 200 LIDAR. The lidar systems estimate the wind velocity from the Doppler shift frequency (induced by atmosphere's aerosol motion) of the backscatter signal. In pulsed lidar, short pulses are sent to the atmosphere, illuminating only a limited part of the line of sight at a given instant. Therefore, the backscatter signal received by the detector comes from a given range of distance at a given time. The time delay, between the start and receive of the pulse, estimates the distance of analyzed zone. For present study the lidar was operated in vertical mode, so that only vertical velocity can be measured. The lidar data quality was verified by recovering classical –5/3 power-law spectra and by successfully comparing the vertical velocity variance with the mixed layer similarity theory, $\frac{\langle w^2\rangle}{w_*^2} = 1.8\left(\frac{z}{z_i}\right)^{2/3}\left(1 - 0.8\frac{z}{z_i}\right)^2$, Lenschow & Wyngaard (1980). Data for the lowest 100 m are not reliable due to the zone of incomplete overlap between telescope and laser. Only data with high carrier to noise ratio (> -15 dB) were considered, eliminating measurements above 400 m.

II.2.5 Solar radiometers

Different solar radiation sensors were used during experiments depending on their availability. For RIMAC and TPHS experimental sites (discussed later) GHI was measured by a LICOR 200SZ pyranometer and surface albedo was measured by a Kipp & Zonen CM6 thermopile albedometer. For BLLAST experimental site (discussed later) different solar radiation components were measured separately. In this field campaign, the radiation measurements were obtained using Kipp & Zonen CM22 and CM21 pyranometers for shortwave up- and down-welling irradiances, and an Eppley_PIR and a Kipp & Zonen CG4 pyrgeometers for longwave up- and down-welling irradiance.

II.2.6 Radiosondes

A radiosonde station was used to measure the atmospheric wind speed, direction and potential temperature profiles upto 20 km with a vertical resolution of 5 m for every 3 – 6 hours. Inversion height, z_i, was then estimated visually by locating increases in potential temperature of greater than 1 K per 100 m from the measured profiles.

II.3 Experimental sites

Three different locations of different surfaces (grass, artificial turf) were chosen to perform the atmospheric observations with some or all of the above mentioned sensors. Details of the experimental sites and meteorological conditions are as followed.

II.3.1 RIMAC experiment

First experiment was conducted over the grass field at RIMAC arena ($32^0$53’ N, $117^0$14’ W) of University of California, San Diego on 29 January, 2010 (Figure II.1a). The IR camera was mounted at 16 m above ground level (a.g.l.), resulting camera field of site of 100x20 m with resolutions of 0.5x0.06 m. Inside the camera field of site, two CSATs and FWTCs were mounted at 1.5 m a.g.l. to measure turbulent wind velocity and temperature at two different locations. The IR camera was operated at 1 Hz, whereas the CSATs and FWTCs were operated at 10 Hz. The GHI and the surface albedo were also measured during the experiment.

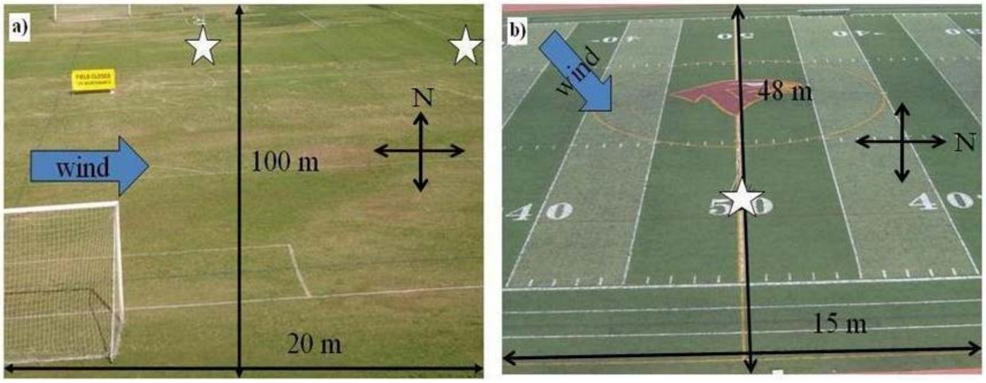

Figure II.1. Field of view of the thermal IR camera images at a) RIMAC and b) TPHS. White stars in the images represent the position of the tripod. Prevalent wind directions and dimensions of the footprint are also shown.

Partly cloudy sky and westerly wind prevailed at RIMAC. Fluctuations in GHI due to the clouds at RIMAC were reflected in mean T_s. The increasing wind speed resulted in a decrease in air temperature due to the sea breeze effects (Figure II.2). The surface temperature time-averaged spatial variation was observed of about 8 K at RIMAC due to irrigation non-homogeneity. Surface albedo for the grass field was measured to be 0.23 during the experiment.

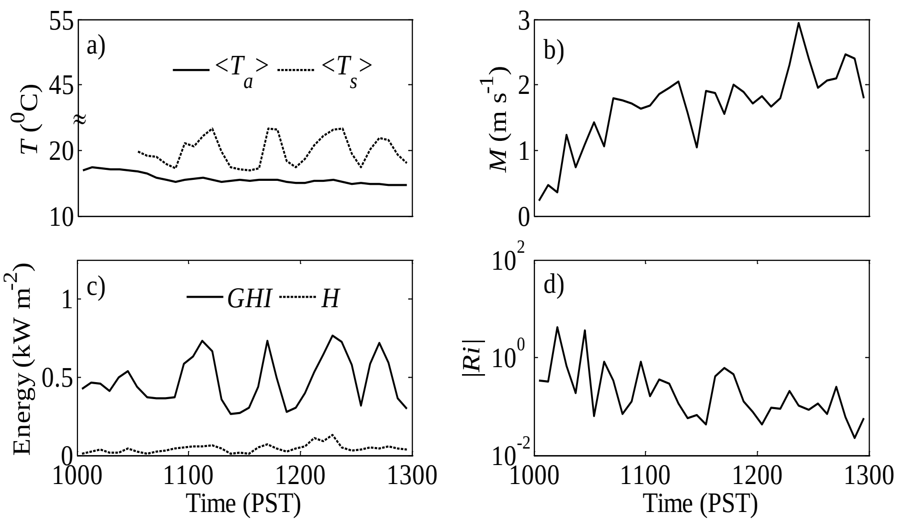

Figure II.2. Time series of the 5-min averaged meteorological conditions, a) air and surface temperature ($<T_a>$, $<T_s>$), b) wind speed (*M*), c) global horizontal irradiance (*GHI*) and sensible heat flux (*H*) and d) Richardson number (*Ri*), for the RIMAC experiment.

II.3.2 TPHS experiment

Another experiment was conducted over an artificial turf field ($32^0$57’ N, $117^0$23’ W) of Torrey Pines High School (TPHS) on 1 May, 2010 (Figure II.1b). The IR camera was mounted at 15 m above ground level (a.g.l.), resulting camera field of site of 48x15 m with resolutions of 0.15x0.08 m. Inside the camera field of site, one CSAT and one FWTC were mounted at 1.5 m a.g.l. to measure turbulent wind velocity and temperature.

The IR camera was operated at 1 Hz, whereas the CSAT and FWTC were operated at 10 Hz. The GHI and the surface albedo were also measured during the experiment.

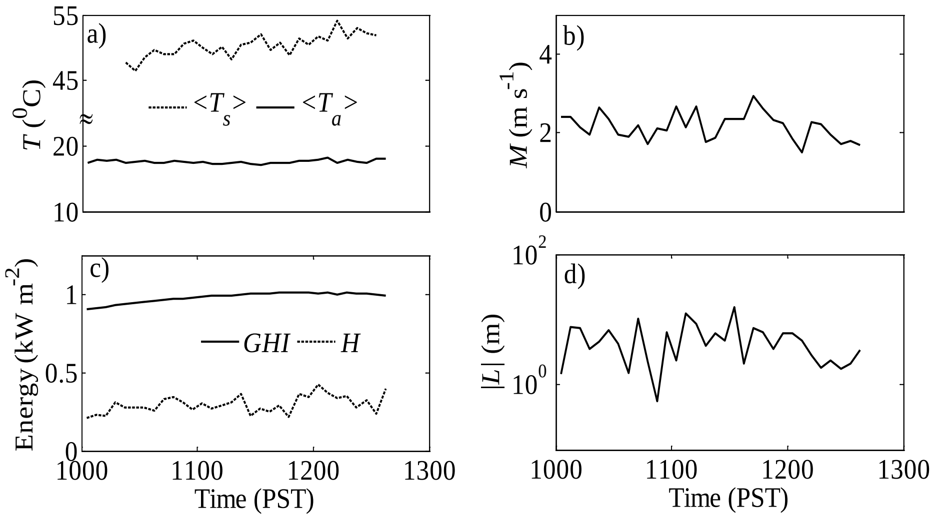

Figure II.3. Time series of the 5-min averaged meteorological conditions, a) air and surface temperature ($<T_a>$, $<T_s>$ averaged over the TIR image), b) wind speed (M), c) global horizontal irradiance (GHI) and sensible heat flux (H) and d) Obukhov length (L), for the experiment at TPHS.

Clear skies with south-westerly winds prevailed at TPHS (Figure II.3). The sensible heat flux was 200 to 400 W m^{-2}, $<T_s>$ was 45-55 ^{0}C, horizontal wind speed was 1.5 to 3 m s^{-1}, and $<T_a>$ was about 18 ^{0}C. Due to lack of the latent heat flux contribution over the artificial turf field, the sensible heat flux and surface temperature was higher in TPHS compared to RIMAC. Surface albedo for TPHS was measured as 0.06 (both for the visually lighter and darker 5 yard stripes).

II.3.3 BLLAST experiment

A month long experiment was conducted in collaboration with Boundary Layer Late Afternoon and Sunset Turbulence (Lothon et al. 2012) field campaign at Centre de Recherches Atmosphériques, Lannemezan, France from 14 June to 8 July, 2011 (Figure

II.4) to measure surface temperature and air turbulence at different height. The IR camera was mounted at 59 m above ground level (a.g.l.) on a 60 m tall tower (43°07’25.15” N, 0°21’45.53” E) looking towards 55° N with an inclination of 2° from 16 to 29 June, 2011 (Case L for “large” field of view of the IR camera) and looking towards 115° N with an inclination of 45° from 30 June to 8 July, 2011 (Case S for “small” field of view of the IR camera). For Case L the camera overlooked a homogeneous 90 mm high grass field with a solar reflectance (albedo) of 0.19 (from radiation measurements) and for the Case S the camera overlooked a less homogeneous field with bare soil, grass, small bushes and small puddles with an average albedo of 0.19. The coordinate transformation resulted in a camera field of site of 450 m x 207 m with a uniform resolution of 4.5 m x 0.65 m for Case L and 92 m x 59 m with a uniform resolution of 0.38 m x 0.18 m for Case S. The main motivation for using two different camera field of sites was to be able to vary the largest and smallest surface temperature scales that can be studied. 1 hr daytime average of the surface temperature from the IR camera shows road, buildings and bare soil to be warmer and a small pond to be cooler than the grass regions in both Case L and Case S (Figure II.4). Thus to limit the effect of surface heterogeneity we ignored the $y > 275$ m region for Case L during the detailed study.

Inside the camera field of view for Case L, four CSATs were mounted on the sonic tower (43°07’39.2” N, 0°21’37.3” E, sonic tower in Figure II.4) at 2.23 m, 3.23 m, 5.27 m and 8.22 m a.g.l. to measure turbulent velocity (u, v, w) and sonic temperature (T_a) at 20 Hz. For Case S, one ultrasonic wind sensor was deployed inside the camera field of view (43°07’26.77” N, 0°21’46.96” E, microbarometer in Figure II.4) at 2.4 m a.g.l. sampling at 20 Hz. For both cases, on the 60 m tower two CSATs at 29.3 m and 61.4 m, and one Gill master pro 3D sonic anemometer at 45.8 m a.g.l. were sampling at 10 Hz to measure turbulent velocity and sonic temperature. These instruments will be referred to as 2, 3, 5 and 8 m sonics for Case L and 2.4, 30, 45 and 60 m sonics for Case S. Five FWTCs were mounted at 0.09, 0.13, 0.19, 0.57 and 1.12 m above ground level at the sonic tower in Case L. Due to insects frequently swarming and breaking the wires of the thermocouples, they were only operated during late afternoon, night and early morning periods. For measurement of outer layer turbulence, the LIDAR (Figure II.4) was operated near the IR camera field of view for Case L at 43°07’32.16” N, 0°21’52.20” E with temporal and vertical resolution of 5 s and 50 m, respectively were measured. The experimental site was also equipped with a radiosonde station at 43°07’41” N, 0°22’01” E (“Sounding” in Figure II.4) to measure vertical profiles of wind speed, direction, temperature, humidity. A radiation tower at 43°07’26” N, 0°21’50.4” E near the 60 m tower was instrumented to report radiation measurements as 1 min averages. All measurement platforms were GPS synchronized to Coordinated Universal Time (UTC) which lags local standard time by 2 hour.

The clear days (19, 20, 24, 25, 26, 27 and 30 June; and 1, 2 and 5 July) were selected for detailed study. There were some early morning clouds during 24 and 30 June and late afternoon clouds during 27 June. Rain (about 2-2.5 mm each) occurred on 18, 22-23, 28-29 June and 3-4 July as cold fonts from the Atlantic Ocean crossed the site. After the rain, the peak air and surface temperature dropped to 20 and 25 °C respectively and thereafter it started to increase. Potential temperature measurements from the radiosondes showed that the inversion height did not exhibit strong diurnal variation except for 20, 26, 27 June and 5 July. It was about 1.25 km for 30 June and 1July; 1 km for 19, 24 June and 2 July; and 600 m for 25 June. It increased from 750 m to 1 km on 20 June, increased from 500 m to 1 km and then dropped to 750 m on 26 June, increased from 750 m to 1 km and then dropped to 450 m on 27 June and increased from 400 m to 700 m to 1 km on 5 July for the 1050, 1350, and 1650 UTC soundings, respectively. Net radiation (the sum of all longwave and solar fluxes at the surface) reached up to 700 W m^{-2} during midday for these clear days. Wind near the surface was 2.5 m s^{-1} for 19, 20, 24 June, 1 July; 3 m s^{-1} for 25-27 June and 1.5 m s^{-1} for 30 June, 2, 5 July. Mixed layer wind speed was close to 8 m wind speed except for 25, 26 and 30 June, when the mixed layer wind speed was at least 25% higher. Wind direction was northerly to easterly during daytime, which is typical for the mountain-plain circulation in the area (Figure II.5 for case L and Figure II.6 for Case S).

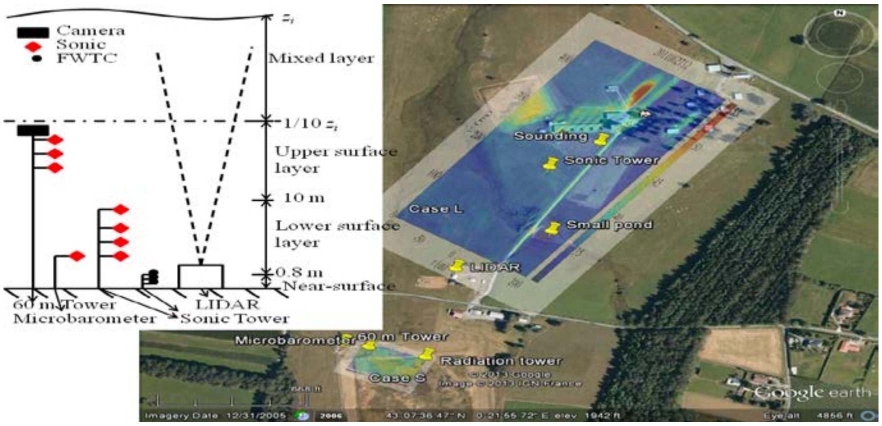

Figure II.4. Google Earth view of the experimental sites (Case L and Case S), with the locations of different instruments. 1-hr averaged surface temperatures for 1200-1259 UTC on 27 June, 2011 for Case L and on 2 July, 2011 for Case S are overlaid. Arrangement and measurement heights for different sensors with respect to the typical boundary layer structure are shown on the in-set of the figure.

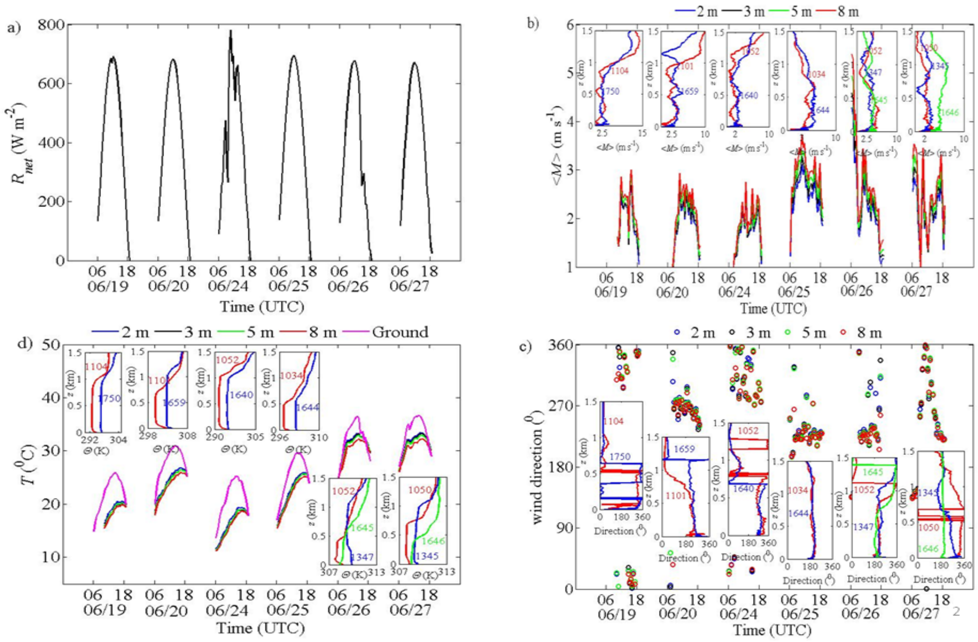

Figure II.5. 30-min averages of (a) net radiation, (b) mean wind speed, <*M*>, (c) temperatures and (d) wind direction for Case L. Radiosonde profiles are show in the insets of (b,c,d), where the release time (HHMM UTC) is shown in color. The wind direction is calculated against the IR image coordinate.

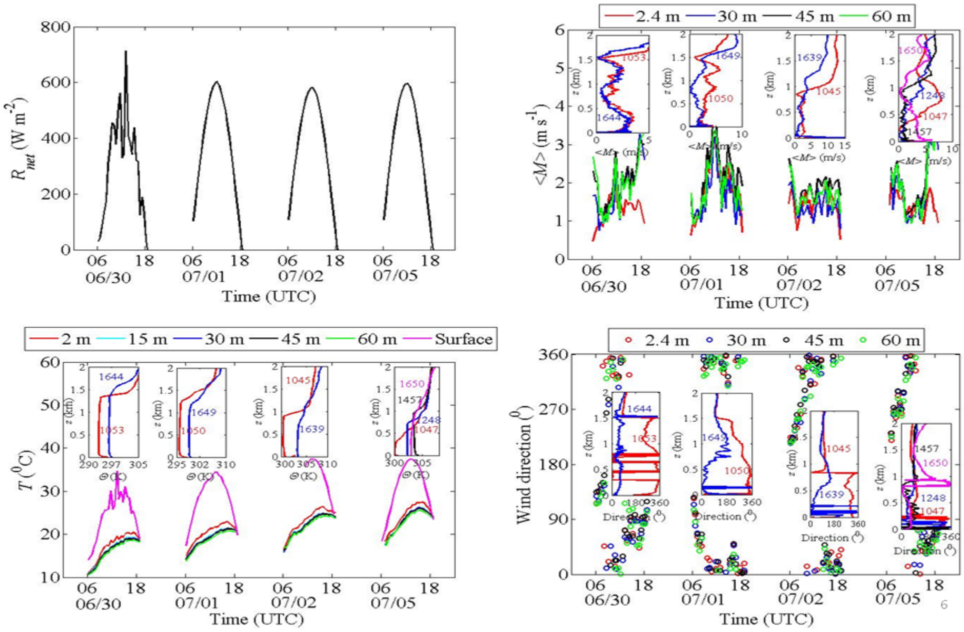

Figure II.6. 30-min averages of (a) net radiation, (b) mean wind speed, <*M*>, (c) temperatures and (d) wind direction for Case S. Radiosonde profiles are show in the insets of (b,c,d), where the release time (HHMM UTC) is shown in color. The wind direction is calculated against the IR image coordinate.

II.4 Data post-processing

Collected data from the previously mentioned field experiments were then analyzed using different data post-processing techniques. Some of the post-processing techniques are discussed below.

II.4.1 Ogive function

The ogive function (Foken et al. 2006) was employed to estimate the sufficient averaging period for calculation of turbulent fluxes using the eddy-covariance method. Ogive ($og_{w.X}(f_o)$) is a cumulative integral of the cospectrum, $Co_{w,X}$, of a variable, X, with vertical velocity, w, starting with the highest frequency, f_0, $og_{w.X}(f_o) = \int_{\infty}^{f_o} Co_{w,X}(f)df$. Ideally the ogive function increases during the integration from high frequency to small frequency, until reaching a constant value. Hence the period corresponding to the frequency at which the ogive reaches the constant value is considered to be sufficient to capture the largest turbulence scales. For an example, we presented the ogive function for Case L of BLLAST experiment in Figure II.7. It was found that a 5-min and 10-min averaging period accounts for 90% (85%) of the maximum value of ogive for CSATs with height < 10 m a.g.l. and lies between 10 m and 70 m, respectively, for the sensible heat-flux (the momentum-flux). Thus an averaging period of 5-min for CSATs with height < 10 m a.g.l., and 10-min for CSATs with height in between 10 m and 70 m were selected.

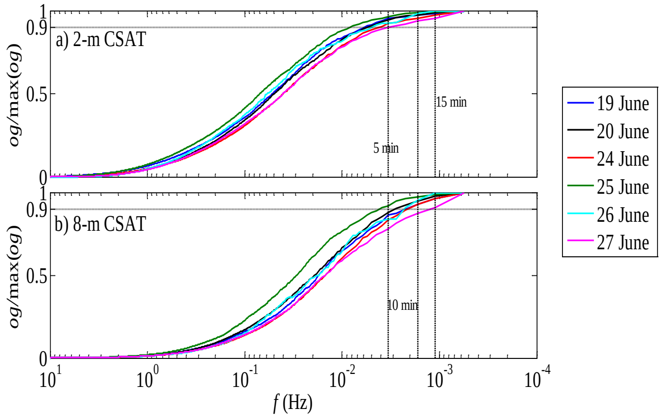

Figure II.7. The normalized ogive by its maximum value for heat-flux calculation at 2-m and 8-m CSAT of all the clear days during Case L of BLLAST experiment.

II.4.2 Scalar footprint

Footprint functions estimate the relative contribution of scalar sources from different ground locations to the measurement location of the scalar. To calculate the footprints of different CSATs, we used the scalar footprint derived from the flux footprint model of Hsieh et al. (2000). In this model, temperature is treated as a passive scalar and the 1-D flux footprint function (*f*) for the unstable boundary layer is

$$f(\tilde{x}, z_m) = \frac{1}{\kappa^2 \tilde{x}^2} 0.28 z_u^{0.59} |L|^{1-0.59} \exp\left(\frac{-1}{\kappa^2 \tilde{x}} 0.28 z_u^{0.59} |L|^{1-0.59}\right) \qquad \text{(II.1a),}$$

where $\tilde{x}$, z_m and z_u are the streamwise distance from the measurement tower, the measurement height and a scaled measurement height defined as $z_u = z_m\left(\log\left({}^{z_m}/_{z_o}\right) - 1 + {}^{z_o}/_{z_m}\right)$, where z_o is the roughness length. The flux footprint (*f*) is related to scalar footprint (*C*) by (Kormann and Meixner, 2001)

$$M \frac{\partial C}{\partial \tilde{x}} = -\frac{\partial f}{\partial z} \qquad \text{(II.1b),}$$

The 1-D scalar footprint function (C) was then used to calculate the 2-D scalar footprint function (C_{2D}) assuming a Gaussian distribution of zero mean and standard deviation of the wind-direction (σ_θ) using

$$\sigma_{\tilde{y}} = \frac{\sigma_\theta \tilde{x}}{1+\sqrt{\frac{\tilde{x}}{400\langle M\rangle}}} \qquad \text{(II.1c),}$$

$$C_{2D} = \frac{C}{\sqrt{2\pi}\sigma_{\tilde{y}}} e^{-\frac{\tilde{y}^2}{2\sigma_{\tilde{y}}{}^2}} \qquad \text{(II.1d),}$$

where $\tilde{y}$ is the spanwise distance.

II.4.3 Wavelet function

To study the lower frequency evolution of the temperature fluctuations we will use wavelet analysis (Hudgins et al. 1993). For a time series, x, its wavelet function, W_x can be calculated by

$$W_x(s,\tau) = \int x(t)\psi_s(t-\tau)dt \qquad \text{(II.2)}$$

where s, τ, ψ_s are scale, time and mother wavelet function respectively. Thus wavelet analysis not only gives the spectral measure of variance, but also the time instant when it appears. So wavelets can be used to detect when a surface renewal event is occurring and analyze wind speeds and temperatures during the event. In this study Morlet was used as the mother wavelet.

II.4.4 Principal orthogonal decomposition

Taking advantage of the spatial information provided by TIR camera, spatial structure of surface renewal events can be analyzed. For that one can employ Principal Orthogonal Decomposition (POD; Pope 2003). Orthogonal decomposition of a function, y, in the interval, $0 \leq x \leq L$, can be written as

$$y(x) = \sum_{n=1}^{\infty} a_n \varphi_n \tag{II.3}$$

where φ_n is the orthogonal basis function such that $\frac{1}{L}\int_0^L \varphi_n(x)\varphi_m(x)dx = \delta_{mn}$ and a_m is the basis function coefficient $a_m = \frac{1}{L}\int_0^L f(x)\varphi_m(x)dx$. From the high energy modes one can reconstruct the large structures, and from rest of the nodes one can reconstruct the residual structures. Thus the spatial evolutions of large and small structures during the surface renewal event can be analyzed using POD technique.

II.4.5 Ground heat flux modeling

A unique aspect of our study is that the ground temperature and heat flux can be forced independently with the measured surface temperature. The ground heat flux, *G* is estimated from the transient 3-D heat conduction equation

$$\frac{\partial T_g}{\partial t} = \alpha_g \left(\frac{\partial^2 T_g}{\partial x^2} + \frac{\partial^2 T_g}{\partial y^2} + \frac{\partial^2 T_g}{\partial z^2}\right), \tag{II.4a}$$

where α_g and T_g are thermal diffusivity and temperature of the ground, respectively. The boundary conditions are the IR camera measured surface temperature at the top (*z* = 0 m) and adiabatic conditions ($\frac{\partial T_g}{\partial z} = 0$) at the bottom boundary (*z* = -5.5 m). The conduction equation was discretized horizontally using a spectral method with periodic boundary conditions; vertically using a second order finite difference scheme; and then time was advanced by the Euler implicit scheme. The numerical solution of Equation II.4a was successfully validated against the analytical solutions of constant and sinusoidally varying surface temperature (not shown). The ground temperature in the domain was initialized by $T_g(x, y, z, t = 0) = T_\infty + \frac{\langle G \rangle}{k_g}\left\{2\left(\frac{\alpha_g \tau}{\pi}\right)^{1/2} \exp\left(-\frac{z^2}{4\alpha_g \tau}\right) + \frac{z}{2} \operatorname{erfc}\left(-\frac{z}{2\sqrt{\alpha_g \tau}}\right)\right\}$, where $\langle G \rangle = \langle R_{net} - \left(1 + \frac{1}{B}\right) H \rangle$ is the mean surface heat flux obtained from the surface energy balance, $\tau = \left[\frac{k_g(\langle T_s \rangle - T_\infty)}{2\langle G \rangle}\right]^2 \frac{\pi}{\alpha_g}$ is a dummy time (Carslaw & Jaeger 1959), T_∞ (= 288 K) is the soil temperature at $z \to -\infty$ (corresponding to the mean annual air temperature) and erfc is the complementary error function. To minimize the effect of unrealistic initial conditions, we neglected the first 100 time steps for simulation spin-up. Since the ground temperature gradient peaks near the surface, the vertical grid resolution was set to 1.5 mm there; below z = -0.05 m the vertical grid was stretched uniformly to 0.1 m resolution. The heat flux at the surface (G) was then computed from T_g as:

$$G = \left[\frac{\Delta z}{2\Delta t} \int_{\Delta t} \rho_g C_{p_g} \frac{\partial T_g}{\partial t} dt\right] - \left[\frac{\Delta z}{2\Delta x} \int_{\Delta x} k_g \frac{\partial^2 T_g}{\partial x^2} dx + \frac{\Delta z}{2\Delta y} \int_{\Delta y} k_g \frac{\partial^2 T_g}{\partial y^2} dy\right] + \left[k_g \frac{T_s - T_{g,-\Delta z}}{\Delta z}\right], \tag{II.4b}$$

where ρ_g, C_{pg}, k_g, Δx, Δy, Δz are density, specific heat, and thermal conductivity of the ground and grid size in horizontal and vertical directions respectively.

II.5 Stationary periods

From the experimental data, the 30-min. periods which satisfy the stationary conditions (standard deviation of six 5 min mean wind speed less than 15% of the mean wind speed and standard deviation of six 5 min wind direction less than 20^0) were considered for detailed analysis in following chapters. These stationary periods were characterized by evaluating the friction velocity (Equation II.5a), the convective velocity (Equation II.5b), the surface layer temperature scale (Equation II.5c), the mixed layer temperature scale (Equation II.5d), the Obukhov length (Equation II.5e), and the flux Richardson number (Equation II.5f):

$$u_* = (\langle u'w' \rangle^2 + \langle v'w' \rangle^2)^{1/4}, \tag{II.5a}$$

$$w_* = \left(\frac{g z_i}{\langle T_a \rangle} \frac{H}{\rho_a C_{p,a}}\right)^{1/3}, \tag{II.5b}$$

$$T_*^{SL} = \frac{\frac{H}{\rho_a C_{p,a}}}{u_*}, \tag{II.5c}$$

$$T_*^{ML} = \frac{\frac{H}{\rho_a C_{p,a}}}{w_*}, \tag{II.5d}$$

$$L = -\frac{\langle T_a \rangle u_*^3}{\kappa g \frac{H}{\rho_a C_{p,a}}}, \tag{II.5e}$$

$$Ri_f = \frac{\frac{g}{\langle T_a \rangle} \frac{H}{\rho_a C_{p,a}}}{u_*^2 \frac{dM}{dz}}, \tag{II.5f}$$

where κ, g and $\frac{H}{\rho_a C_{p,a}}$ are von Kármán constant, gravitational constant and turbulent sensible heat flux (estimated using $\frac{H}{\rho_a C_{p,a}} \approx \frac{\langle w T_a' \rangle}{(1+0.06/B)}$, where ρ_a, $C_{p,a}$ and B are the dry air density, dry air specific heat and the Bowen ratio , defined as the ratio between sensible and latent surface heat fluxes), using the lowest CSAT data. These parameters have been tabulated in Table II.1.

Table II.1. Characteristics for the stationary periods chosen for detailed analysis ordered by stability conditions for the three experiments. Time for RIMAC and TPHS is reported in Pacific Standard Time, and that for BLLAST is reported in Coordinated Universal Time.

Experiment	Time	L (m)	Ri_f (-)	$\boldsymbol{u_*}$ (m s^{-1})	$\boldsymbol{w_*}$ (m s^{-1})	$\frac{\boldsymbol{H}}{\boldsymbol{\rho_a C_{p,a}}}$ (K m s^{-1})	z_i (km)
RIMAC	1210-1240, 29 Jan	-16.84	-0.13	0.22	0.94	0.051	0.5
TPHS	1215-1245, 1 May	-2.33	-2.00	0.19	1.64	0.270	0.5
	1130-1200, 1 May	-5.66	-0.46	0.26	1.62	0.255	0.5
BLLAST	1230-1300, 2 July	−1.12	−5.11	0.12	1.56	0.116	1.0
	0625-0655, 1 July	−1.77	−2.54	0.10	1.04	0.033	1.2
	0925-0955, 5 July	−5.21	−0.77	0.19	1.50	0.102	0.5
	0930-1000, 27 June	−5.49	−0.66	0.15	0.95	0.045	0.6
	1125-1155, 5 July	−5.71	−0.65	0.21	1.58	0.119	0.7
	0900-0930, 5 July	−6.16	−0.63	0.19	1.42	0.086	0.5
	0800-0830, 5 July	−6.22	−0.64	0.18	1.30	0.066	0.5
	0830-0900, 26 June	−6.68	−0.52	0.15	0.71	0.028	0.4
	0825-0855, 5 July	−7.19	−0.52	0.19	1.34	0.072	0.5
	1100-1130, 20 June	−7.27	−0.47	0.22	1.38	0.113	0.7
	1100-1130,27 June	−8.45	−0.39	0.19	1.15	0.058	0.8
	1030-1100, 27 June	−8.45	−0.39	0.18	1.06	0.053	0.7
	1530-1600, 20 June	−8.84	−0.37	0.19	1.31	0.062	1.1

Table II.1. Cont.

Experiment	Time	L (m)	Ri_f (-)	$\boldsymbol{u_*}$ (m s^{-1})	$\boldsymbol{w_*}$ (m s^{-1})	$\frac{\boldsymbol{H}}{\boldsymbol{\rho_a C_{p,a}}}$ (K m s^{-1})	z_i (km)
	0935-1005, 26 June	−9.40	−0.35	0.17	0.82	0.043	0.4
	0825-0855, 27 June	−10.22	−0.31	0.15	0.76	0.027	0.5
	1200-1230, 25 June	−11.74	−0.27	0.26	1.23	0.112	0.5
	1000-1030, 1 July	−11.98	−0.28	0.25	1.49	0.099	1.2
	1600-1630, 5 July	−12.48	−0.27	0.18	1.05	0.035	0.4
	1030-1100, 25 June	−12.49	−0.25	0.27	1.23	0.112	0.5
	1500-1530, 1 July	−13.51	−0.25	0.25	1.39	0.080	1.2
	0700-0730, 5 July	−14.22	−0.23	0.18	1.01	0.031	0.3
	0900-0930, 25 June	−14.33	−0.21	0.27	1.18	0.098	0.5
	1000-1030, 25 June	−14.73	−0.20	0.28	1.22	0.109	0.5
	0830-0900, 25 June	−15.60	−0.19	0.26	1.10	0.079	0.5
	1000-1030, 26 June	−19.46	−0.15	0.22	0.81	0.042	0.4
	1115-1145, 26 June	−19.49	−0.15	0.24	1.00	0.053	0.6
	1530-1600, 25 June	−19.61	−0.15	0.23	0.93	0.049	0.5
	1000-1030, 27 June	−22.32	−0.13	0.26	1.10	0.059	0.7
	1130-1200, 26 June	−22.81	−0.12	0.25	0.98	0.049	0.6
	1130-1200, 25 June	−23.57	−0.12	0.33	1.25	0.117	0.5
	1700-1730, 20 June	−36.49	−0.07	0.21	0.88	0.019	1.1
	1025-1055, 26 June	−37.23	−0.07	0.29	0.87	0.051	0.4

Chapter III

Surface temperature and Surface Renewal analysis

III.1 Introduction

In a convective boundary layer (CBL), due to solar heating air near the surfaces heats up and ascends through the atmosphere. In laboratory experiments of turbulent free convection over a heated horizontal surface by Townsend (1958), Howard (1966), Kline et al. (1967) and Corino and Brodkey (1967) the temperature fluctuations showed periodic activity, characterized by alternating large fluctuations and periods of quiescence. Flow visualization by Sparrow et al. (1970) reveals that these periodic activites are due to mushroom-like structures of ascending hot fluid. In the CBL, the ascending warm air in the surface layer (ASL) is known as surface layer plumes. Kaimal and Businger (1970), Kaimal et al. (1976), Wilczak and Tillman (1980) and Wilczak an Businger (1983) found that surface layer plumes have diameters and depths on the order of the ASL and an advection velocity that is close to the average wind speed over their depth (Renno et al. 2004). Wind shear causes them to tilt by about 45^{o} in the flow direction (Stull 1997). Above the ASL these plumes become more diffuse and combine to form thermals which have larger length scales, of the order of the atmospheric boundary layer (Caughey and Palmer 1979; Young 1988c; Deardorff and Willis 1985). Based on the flow visualizations by Corino and Brodkey (1967) and Sparrow et al. (1970), Liu and Businger (1975) and Brutsaert (1975) proposed analytical models for heat transfer during forced and free convection. They assumed that the eddies responsible for plume-like structures are of the order Kolmogorov scale for smooth walls and roughness height for rough walls.

Gao et al. (1989), Paw U et al. (1992), Braaten et al. (1993) and Raupach et al. (1996) studied coherent turbulent structures, known as surface renewal (SR) events, in different canopies. In the SR process a cold air parcel approaches the ground during a sweep. As it stays in contact with the ground heat is transferred from the ground to the parcel, until it has sufficient buoyant force. The heated air parcel then ascends during the ejection event. Thus the air temperature time series contains sawtooth or ramp like features. These ramp patterns were most clearly seen in the middle and upper portion of the canopy. Utilizing the characteristics of these coherent structures, Paw U et al. (1995), Snyder el at. (1996), Spano et al. (1997, 2000), Castellvi et al. (2002), Castellvi (2004) and Castellvi and Snyder (2009) proposed and validated the SR method to estimate surface sensible and latent heat fluxes given the statistics of high frequency air temperature measurements.

Plumes and thermals like coherent structures in CBL will then cause high frequency ground temperature fluctuation. Paw U et al. (1992), Katul et al. (1998) and Renno et al. (2004) observed such surface temperature fluctuation of around 0.5 ^{0}C over 2.6 m high maize crops under unstable condition, greater than 2 ^{0}C over a 1 m high grass covered forest clearing and 2-4 ^{0}C over a desert area, respectively. The fluctuations were attributed to inactive eddy motions (Katul et al. 1998) and convective mixed layer processes (Reno et al. 2004). According to Townsend (1961) turbulent motion in the inner layer of the boundary layer is composed of i) “active” motion due to the shear near the surface, and ii) “inactive” motion due to outer region turbulence. The inactive eddy motion can be detected from the near surface pressure fluctuations and in the lower wavenumber part of the longitudinal velocity spectra (Katul et al. 1996).

Vogt (2008) and Christen and Voogt (2009, 2010) visualized the spatial surface temperature field over a bare field and in a suburban street canyon using 1 Hz thermal infrared (IR) imagery, respectively. Heat transport from urban lawns was qualitatively attributed to coherent structures and small scale turbulence. Balick et al. (2003) studied spatial variation of surface temperature from satellite imagery and modified the Brutsaert-Liu-Businger surface renewal approach to couple surface temperature with turbulent heat flux. From 1 Hz IR data Kustas et al. (2002) studied the energy budget at a riparian corridor.

While turbulent coherent structures in the convective boundary layer are well-understood, their effect on the surface skin temperature is less studied. Our objective is to connect these different research areas by analyze the spatio-temporal structure of skin temperature fluctuations and their coupling to atmospheric turbulent coherent structures. Ultimately this research could lead to a more fundamental understanding of land-atmosphere interaction and heat transfer at the earth's surface.

III.2 Results

Data from TPHS experiment was used for this study. Details of the observed meteorological condition are discussed in Chapter II.3.2. A 30-min stationary period during 1130-1200 PST, 1 May 2010 ($L = -5.66$ m, Chapter II.5) was chosen to present the detailed results.

The statistics of velocity and temperature fluctuations (standard deviation σ, skewness, kurtosis) are reported in Table III.2.1. Figure III.1a-c depicts a typical 5-min time series of ground and air temperature, heat flux and (u', w') velocity. Ejection events (updrafts with positive w') occur less frequently but are associated with large heat fluxes than sweep events (downdrafts with negative w'). To study the lower frequency evolution of the temperature fluctuations we used wavelet analysis (Hudgins et al., 1993). For a time series, f, its wavelet function, W_f can be calculated by $W_f(s,\tau) = \int f(t)\psi_s(t-\tau)dt$ where s, τ, ψ_s are scale, time and mother wavelet function respectively. Thus wavelet analysis not only gives the spectral measure of variance, but also the time instant when it appears. We can use wavelets to detect when a surface renewal event is occurring and analyze wind speeds and temperatures during the event. In this study we will use Morlet as a mother wavelet.

Table III.1. Standard deviation σ, skewness, and kurtosis of the velocity components, air temperature and ground temperature fluctuations during the 1130-1200 PST.

	u	v	w	T_a	T_s
$\boldsymbol{\sigma}$	1.00 m s^{-1}	1.20 m s^{-1}	0.40 m s^{-1}	1.60 K	1.12 K
Skewness	0.40	0.10	-0.30	1.30	-0.14
Kurtosis	3.25	3.01	4.34	4.80	3.48

Figure III.1d-e shows the wavelet scalogram of the air and ground temperature fluctuation. There is a similarity between the $T_a{}'$ and $T_s{}'$ scalogram for scales of 60-sec and longer and the $T_s{}'$ time series lags $T_a{}'$ by about 20-sec. Consistent with the time series plot of $T_s{}'$and $T_a{}'$ (Figure III.1a) and energy spectra (not shown), smaller scale $T_a{}'$ fluctuations (< 20 sec) have more energy than $T_s{}'$. This is due to the fact that the ground has a larger thermal mass than air and also due to the spatial averaging over the footprint. Consequently, the ground temperature signature of small eddies fall below the 0.08 K noise level of the IR camera. The 1 Hz IR data acquisition frequency (the highest possible with this IR camera model) was sufficient to resolve the majority of T_s fluctuations. The large scale fluctuations (scale > 60 s) are correlated but out of phase: $T_s{}'$ lags $T_a{}'$.

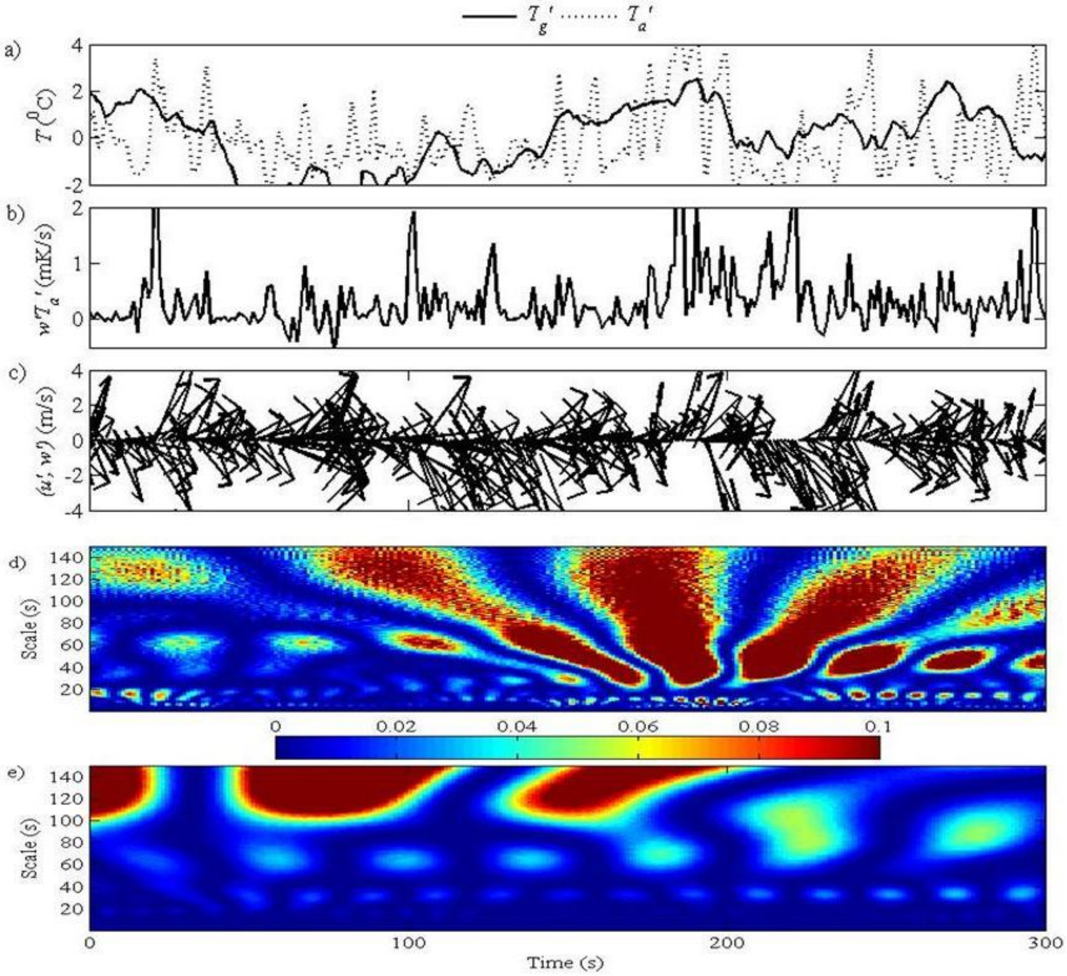

Figure III.1. Time series of a) air and ground temperature fluctuations (average over footprint), b) kinematic heat flux, c) *u*-*w*-velocity vector and scaled wavelet scalogram of d) air and e) ground temperature fluctuations for 1147-1152 PST.

One would expect a correlation between $T_a{}'$ and $T_s{}'$ within the footprint of the CSAT (as seen in Figure III.1a). The temperature of an air parcel is affected by the temperature within its upwind ground footprint. Thus, the correlation between them should be maximum when the $T_a{}'$ time series is lagged by the time it takes for air parcels to be advected from the footprint. On the other hand as air moves downstream, it will affect the downstream ground temperature causing high correlation with positive lag. Figure III.2 shows the maximum correlation and corresponding lag between $T_s{}'$ and $T_a{}'$, where a negative lag means that $T_s{}'$ preceded $T_a{}'$. The maximum correlation region aligns with the mean wind direction. Both the upstream and downstream region show high correlation in a region that extends up to 5 to 10 m in the streamwise direction, with negative lag upstream and positive lag downstream. While this is an expected result, this is the first time that this could be shown explicitly with spatial surface temperature data.

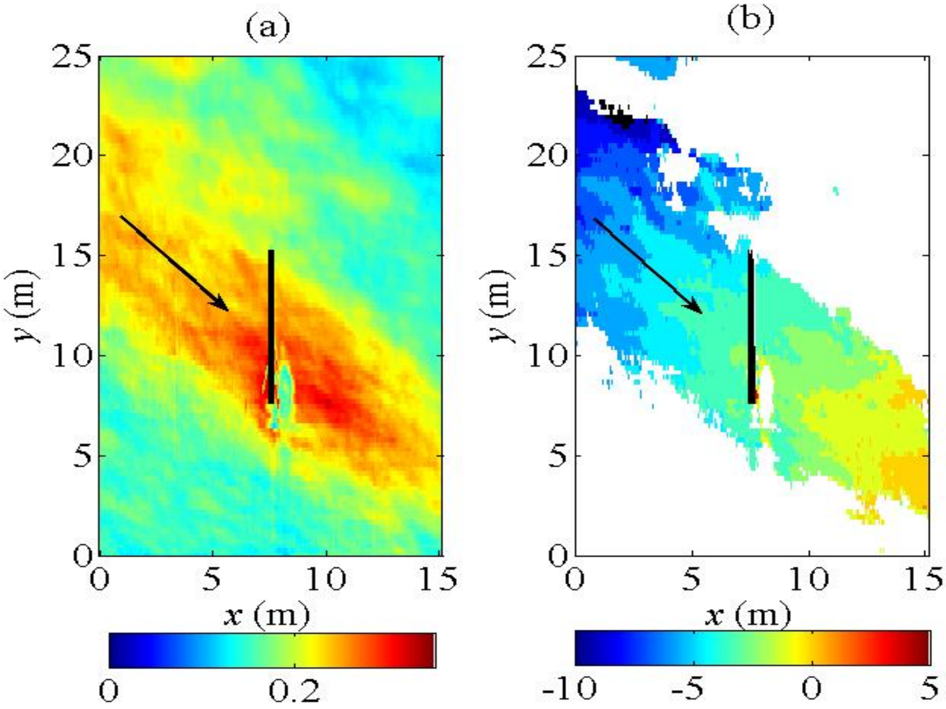

Figure III.2. Spatial dependence of (a) maximum correlation and (b) corresponding time lag [sec] between air and ground temperature for 1130-1200 PST. The black vertical bar marks the location of the tripod and the black arrow represents the mean wind direction. The white region in Figure III.2b indicates a ground-air temperature correlation of less than 0.2.

Figure III.3 shows only the upstream correlation between $T_s{}'$ and $T_a{}'$. The air temperature measurements are conducted at the coordinate origin (0-sec lag and 0 m distance). Upwind (negative distance) the lag with maximum correlation becomes negative. Consequently, this graph is a 2-dimensional depiction of correlation value

(Figure III.2a) and lag (Figure III.2b) along a line upwind of the $T_a{}'$ measurements. The slope of the line of maximum correlation indicates the velocity of the coherent structures. From the horizontal and vertical separation between a ground pixel and the $T_a{}'$ sensor, the horizontal advection and vertical dispersion velocity of the coherent structures can be estimated, respectively. The estimated horizontal velocity is 3.30 m s^{-1}, which is greater than the mean wind speed at 1.5 m a.g.l. and the vertical velocity is 0.48 m s^{-1}, which is close to standard deviation of *w* (Table III.1). The upwind maximum correlation region also is qualitatively consistent with the flux footprint function of Hsieh et al. (2000).

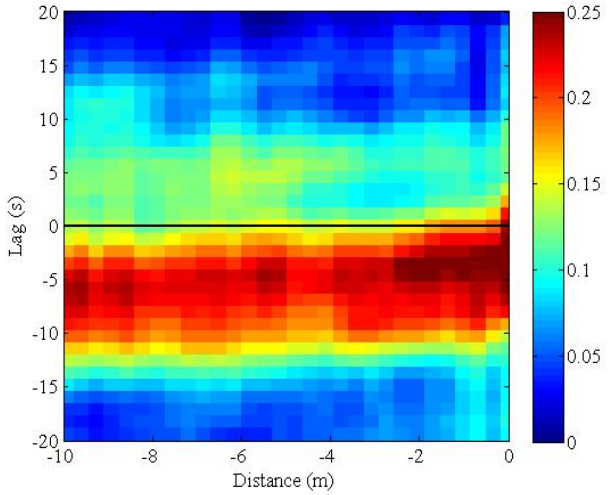

Figure III.3. Correlation map between air temperature and upwind ground temperature at different distances (*x* axis) and time lags. The horizontal white line represents zero lag.

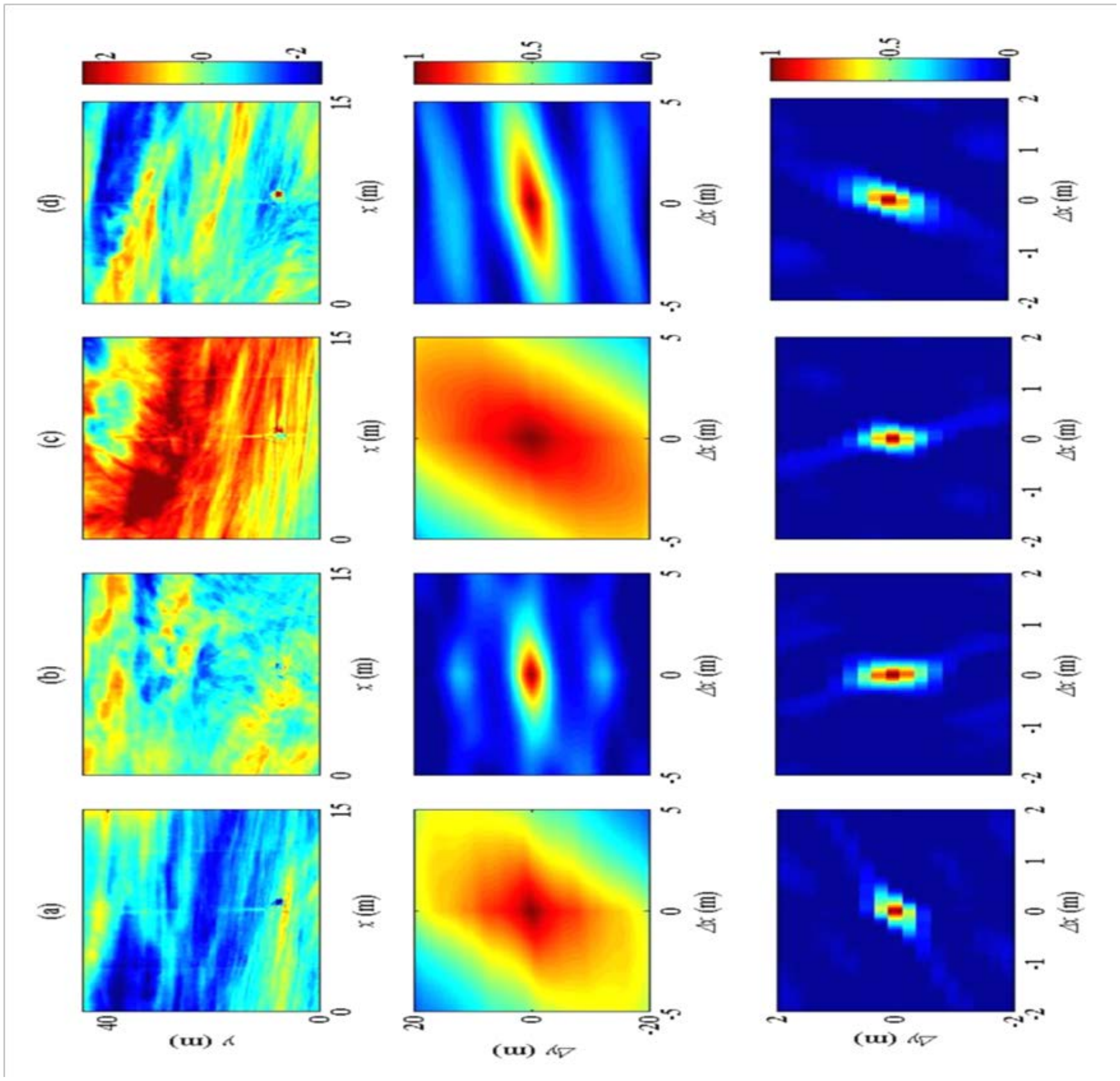

Figure III.4. Snapshots of ground temperature fluctuation (K) (upper panel) at Δt = a) 0 s, b) 10 s, c) 55 s and d) 90 s during a renewal event starting at 114924 PST. Spatial correlation map for large (middle panel) and residual small (lower panel) structures are obtained from Principal Orthogonal Decomposition. The wind direction is from upper left (south-westerly).

We now take further advantage of the spatial information provided by IR camera to explore the manifestation of a renewal event. A sequence of snapshots of $T_s{}'(x,y)$ during a renewal event is shown in the upper panel of Figure III.4 for 114924-115054 PST (from 144 to 234 sec in Figure III.1). Initially $T_s{}'$ is negative over the footprint

(Figure III.4a) which can be attributed to a sweep event, when cold air comes in contact with ground. Shortly thereafter, several small hot spots appear (Figure III.4b). These hot spots grow, combine, and move in the wind direction. At the subsequent time $T_S{}'$ in the entire image becomes positive (Figure III.4c) initiating an ejection event. As the heated air rises from the ground due to its buoyancy, the ground starts to cool (Figure III.4d) again.

To study these spatial structures we employ Principal Orthogonal Decomposition (POD, Pope, 2003). Large structures are reconstructed using the ten most energetic POD modes and small structures are constructed using the residual nodes (Figure III.4 middle and lower panels). We caution that since the size of the structures exceeds the size of the IR camera image, the structures depicted here are not the largest structures. When the ground is either hot or cold (Figure III.4a,c), i.e. during sweep and ejection, the large structures are larger compared to the time when ground is heating up or cooling down (Figure III.4b,d). Following the model of coherent eddies by Williams and Hacker (1992) and Vogt (2008), hot or cold ground (Figure III.4a,c) can be attributed to a transition between two roll vortices near the ground leading to large updrafts or downdrafts. The ground heating up or cooling down (Figure III.4b,d) can be attributed to a roll vortex being centered over the site leading to sweeping away of small eddies. On the other hand the residual small structures do not depend on the phase of the renewal event. Also the orientation of the large structures is more aligned with the wind direction compared to the residual small structures (Figure III.5).

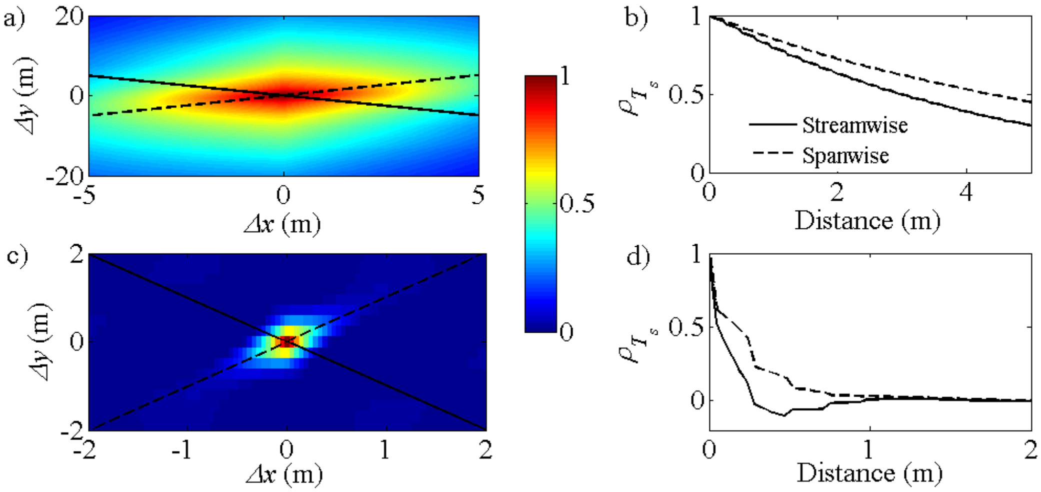

Figure III.5. Average from 1130-1200 PST of the spatial correlation (colorbar) map for a) large and c) residual small T_s' structures based on POD with streamwise and spanwise correlation for b) large and d) residual small structures. Solid and dashed lines represent the mean streamwise and spanwise wind directions, respectively.

Our analysis has shown that the dimensions of the surface temperature scales are larger than the IR camera image (Figure III.4a,c) and their temporal scale is several advection time scales through the image (Figure III.1). Ideally the IR camera footprint should be greater than the large scales, but even with our wide-angle lens this would require flying the camera on a stabilized balloon at several 100 m in altitude. To illustrate the spatio-temporal evolution of the structures, we draw a line through the image in streamwise direction and plot the time evolution of $T_s{}'$ along this line for 1147-1152 PST in Figure III.6a. Most large events indeed last tens of seconds and are larger than 20 m in scale. Based on Figure III.6a, but considering all lines aligned in the streamwise direction, Figure III.6b provides the mean of the correlation statistics across space and time. The advective nature of the structures can be seen from the upward slope of the hot and cold ‘stripes’ of $T_s{}'$ in Figure III.6a and the downward slope of the spatio-temporal correlation profile in Figure III.6b. The estimated horizontal velocity from the slope of spatio-temporal correlation profile for the structures is 3.18 m s^{-1}, which is also close to the estimated horizontal velocity from the ground-air correlation (Figure III.3). Also the high correlation region in Figure III.6b indicates both the temporal and spatial extent of a structure in the downwind direction.

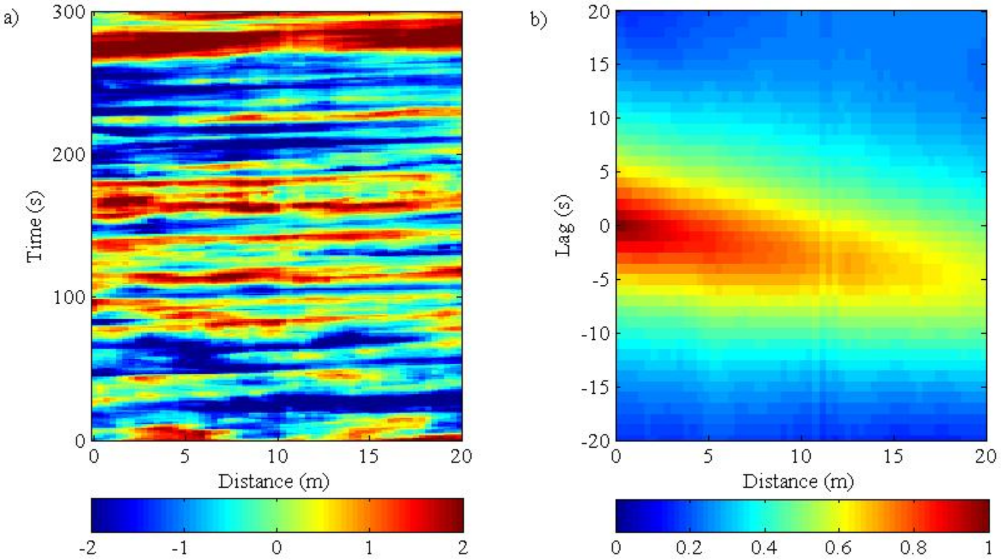

Figure III.6. a) Temporal evolution of T_s' along a line through the image oriented in the stream wise direction. b) Spatio-temporal correlation of T_s' at a point to points upstream in the streamwise direction at distances of 0 to 20 m for different time lags.

III.3 Conclusions

In this proof-of-concept study we evaluate the ground and air temperature interaction for the convective atmospheric boundary layer using IR imagery. With only data from one day presented, the analysis is not exhaustive and more extensive studies on the topic are needed, but practical issues (since the thermal camera is not waterproof and expensive it cannot be left unattended) and lack of funding make long-term studies difficult. Most existing eddy covariance sites are not suitable to conduct the experiment since short vegetation is required. In the absence of vegetation (e.g. over a parking lot), the thermal admittance is too small and $T_s{}'$ cannot be detected (not shown). If the vegetation is too high, 'honamis' or ocean-wave-like motion of crops will occur and the resulting shading and varying solar incidence angle pattern complicate the analysis (Finnigan, 2010). The ideal site for this experiment would be a dry (large buoyancy), flat and homogeneous surface (no roughness or inhomogeneity effects) with small vegetation (eliminating honami effects of tall vegetation yet preserving large thermal admittance of vegetation versus sand or asphalt) and a high viewpoint for camera. Our site fulfilled all criteria except for the large scale homogeneity. Nearby berms and buildings may have led to shedding of eddies, but the low wind speed reduced the effect of eddies shed by surrounding building. Surface temperature spectra did not show an increase in energy at frequencies near the expected shedding frequency of eddies from nearby obstacles. While other researchers have examined T_s variability, our study is the first to provide a thorough quantitative spatial analysis of surface-atmosphere exchange using IR imagery.

The speed of the coherent structures was 1.5 times the wind speed at 1.5 m a.g.l. and consistent with a velocity at 6.5 m a.g.l. (estimated from the stability corrected log-profile). Christen and Voogt (2010) reported the speed of these coherent structures to be twice the wind speed at ~ 0.5 m a.g.l. This difference in ratio between the speed of the coherent structure and wind may be due to the fact Christen and Voogt (2010) gathered their measurement closer to the surface and inside a street canyon, compared to our open field. Katul et al. (1998) found that T_s fluctuations are driven by inactive eddy motion, which scaled as mixed layer turbulence. Our wavelet analysis showed that only large coherent structures leave a T_s signature and these structures (time scale > 60 s) are responsible for the majority of the sensible heat flux. Also air temperature at 1.5 m a.g.l. was correlated to upwind and downwind T_s in a region of width of about 5 m (about 3 times the measurement height).

In a convective atmospheric boundary layer, mixed layer roll vortices are the large-scale eddies responsible for transport of momentum, heat and mass. While we can only observe the manifestations of atmospheric turbulence on surface temperature, we believe that the observed patterns are consistent with the following concepts. The downward flowing part of this mixed layer roll vortex will cause cold air to approach the ground during a sweep event. This cold air in contact with the warm ground will cause a large heat flux from ground to the air, causing large portions of the IR imagery to cool. With time the air heats up, causing heating up of the ground. This phenomenon manifests itself by small hot patches. As the air and ground heat up, the warm air will result in an updraft due to its buoyancy, which represents the thermal or upward flowing part of mixed layer roll vortices or 3-D cells. After the updraft, the surrounding cold air will approach the ground and the cycle repeats. As these roll vortices or 3-D cells are advected by the wind, the ground temperature footprint of these structures moves in the wind direction. Thus turbulence in the unstable atmospheric boundary layer induces coherent patterns of T_g fluctuations that can be visualized through IR imagery. An additional experiment was conducted for stable conditions at the 285x150 m irrigated grass field (RIMAC) at University of California, San Diego ($32^0$53’ N, $117^0$14’ W) on 10 August 2010. At RIMAC, the surface temperature variability consisted only of white noise, presumably because surface temperature variations were below the noise level of the IR camera. This finding is consistent with the fact that coherent structures and air temperature variances are smaller in stable conditions.

We observed within-image temporally averaged standard deviations of 0.7 K, which is 0.7 times the convective temperature scale, T_*, consistent with the value measured for a high resolution satellite image by Balick et al. (2003). The temporal standard deviation of T_s (Table III.1) is also comparable with the studies carried out by Katul et al. (1998) and Renno et al. (2004). T_s fluctuations driven by atmospheric turbulence have practical implications for remote sensing e.g. of land mine signatures or evapotranspiration (ET) for irrigation management. Hydrologic energy balance models (e.g. SEBAL by Bastiaansen et al., 1998a,b) derive the sensible heat flux (and ET) through the surface energy balance from spatial differences in surface and air temperature. The large coherent structures can introduce physical ‘noise’ in ET estimates especially if single-image satellite or aerial IR imagery at high spatial resolution is used.

Acknowledgements: Content of this chapter has been published in Garai A, & Kleissl J, 2011, Air and surface temperature coupling in the convective atmospheric boundary layer, *J. Atm. Sci.*, **68**, 2945-2954. The dissertation author was primary investigator and author of this paper.

Chapter IV

Surface temperature and turbulent coherent structures

IV.1 Introduction

Coherent structures play an important role for turbulent momentum, heat and mass transport processes in an unstably stratified boundary layer. Laboratory experiments of turbulent free convection (Thomas & Townsend 1957; Townsend 1959; Howard 1966; Sparrow et al. 1970; Deardorff et al. 1969; Willis & Deardorff 1974, 1979; Deardorff & Willis 1985) and classical Rayleigh-Bénard convection (Ahlers et al. 2009; Lohse & Xia

2010; and the references therein) show that in purely thermally driven turbulence most observed coherent structures are warm fluid ascending mushroom-like from the warm surface, cold fluid descending mushroom-like from the cold surface, and resulting large scale circulation. The qualitative nature of these coherent structures can be modified by adding background shear. In the shear-dominated forced convective regime, temperature acts as a passive scalar and the coherent structures become long and streaky with alternating high and low speed fluid (Kline et al. 1967; Head & Bandyopadhyay 1981; Adrian 2007). In a convective atmospheric boundary layer (CBL), the observed coherent structures show different characteristics based on the relative strengths of buoyancy and background shear.

In the logarithmic layer of the CBL, known as surface layer, both shear and buoyancy play dominant roles in turbulent transport. Intermittent warm rising air, known as surface layer plume, is the most common coherent structure (Kaimal & Businger 1970; Wynagaard et al. 1971; Kaimal et al. 1976; Wilczak & Tillman 1980; Wilczak & Businger 1983; Renno et al. 2004). These plumes are tilted by about 45° due to shear, move with the averaged wind speed over their depth, and have diameters on the order of the surface layer height. They are separated from each other by weaker cold downdrafts. Thus the temperature trace across them shows a sawtooth like pattern (Schols 1984; Schols et al. 1985; Gao et al. 1989; Paw U et al. 1995), which acts as a genesis of the surface renewal method. According to the surface renewal method, a cold air parcel descends to the ground during the sweep event, as it remains close to the ground it is heated, and when it achieves sufficient buoyancy the warm air parcel ascends during the ejection event.

As the surface layer plumes ascend to the ‘outer layer’ of the CBL, known as the mixed layer, they merge with each other to create thermals with diameters on the order of CBL depth. These thermals cause intense vertical mixing, resulting in constant wind speed, potential temperature and moisture in the mixed layer. The warm updraft and cold downdrafts together constitute roll vortices in the mixed layer (LeMone 1973; Lenschow & Boba Stankov 1986; Young 1988a,b; Cohn et al. 1998; Drobinski et al. 1998; Lothon et al. 2006) with time scales on the order of the convective eddy turnover time scale.

These coherent structures of the CBL, i.e. surface layer plumes, thermals, downdrafts, roll vortices, imprint themselves onto the surface through modification of heat transport between the surface and the air. For example, Schols et al. (1985); Derksen (1974) measured streaky surface temperature patterns along the wind direction with 2 °C temperature heterogeneity using an airborne thermal infra-red (IR) camera. Renno et al. (2004); Gao et al. (1989); Katul et al. (1998) observed surface temperature fluctuations with an amplitude of 0.5 °C over 2.6 m high maize crops, greater than 2 °C over 1 m high grass, and 2-4 °C over a desert area respectively using an IR temperature sensor. Using an IR camera mounted on a tall tower, spatial heterogeneities in the magnitude of surface temperature fluctuations were also observed by Ballard et al. (2004); Garai et al. (2013) in a grass canopy, Vogt (2008) in a bare field, Christen & Voogt (2009, 2010) in an urban street canyon, Garai & Kleissl (2011) in an artificial turf field, and Christen et al. (2012) in an urban environment. Hetsroni & Rozenblit (1994); Hetsroni et al. (2001); Gurka et al. (2004) observed similar surface temperature coherent patterns in laboratory experiments.

Ballard et al. (2004) postulated that high frequency surface temperature fluctuations are caused by turbulent mixing. Katul et al. (1998) and Renno et al. (2004) hypothesized that surface temperature fluctuations are caused by inactive eddy motion governed by convective mixed layer processes. Christen & Voogt (2009, 2010) qualitatively attributed the vertical heat transport to coherent structures whose imprints were observed in the surface temperature field moving along the wind direction. Garai & Kleissl (2011) studied temporal and spatial evolution of surface temperature patterns in the context of the surface renewal concept. The surface temperature patterns showed large cold structures during sweep events, small patches of warm structures in a cold background during the transition from sweep to ejection, large warm structures during the ejection events and small patches of cold structures in a warm background during the transition from ejection to sweep. Christen et al. (2012) reported different surface temperature standard deviations over different surfaces (metallic roofs > lawns > roads > building walls) for an urban measurement site. Direct numerical simulation of solid-fluid coupled turbulent heat transport (Tiselj et al. 2001) and land-atmosphere coupled heat transport model (Balick et al. 2003) revealed that the imprint of fluid temperature fluctuations on the surface depends on the relative thermal properties of the fluid and solid. Hunt et al. (2003) observed different forms of coherent structures (plumes, puffs etc.) by varying surface thermal properties in their direct numerical simulation of solid-fluid coupled turbulent heat transport process.

The main objective of the present experiment is to study the influence of different coherent structures with widely varying scales in the CBL on the surface temperature and ground heat flux at different levels of thermal instability. A unique dataset was collected that spans from thermal imagery of the surface to wind and temperature measurements through the CBL. Spectral density and probability density functions were employed to study the evolution of air temperature fluctuations with height and compare them against surface temperature fluctuations. The solid-fluid coupled heat transport mechanism was then studied by identifying coherent structures at different heights.

IV.2 Results

Data from BLLAST field experiment was used for this study. Details of the experimental campaign and meteorological condition are discussed in Chapter II.2.3. We have chosen $L = -6.68$ m (0830-0900, 26 June 2011) and -14.33 m (0900-0930, 25 June 2011) as representative periods for more stable and less unstable boundary layer to illustrate our findings, as high quality data from most sensors were available. Since mixed layer (LIDAR) data ($0.1 \leq z/z_i \leq 1$) for $L = -6.68$ m were not available a period with $L = -6.22$ m (0800-0830, 5 July 2011) was chosen instead for the comparison with mixed layer, which had surface temperature measurement with upper surface layer turbulence measurements. All other stationary periods reveal qualitatively similar findings.

IV.2.1 Spatial evolution of temperatures

At a given time the surface temperature shows large warm and cold structures aligned with the mean wind (Figure IV.1). Animations of these structures reveal that they grow in size, combine with each other and continue to move with the wind (see the supplemental material). Previous studies (Renno et al. 2004; Schols 1985; Derksen 1974; Katul et al. 1998; Ballard et al. 2004; Garai et al. 2013; Vogt 2008; Christen & Voogt 2009, 2010; Garai & Kleissl 2011; Christen et al. 2012; Balick et al. 2003) attributed these surface temperature structures to turbulence in the overlying flow. To test this hypothesis, in Figure IV.1, time series of air temperature over different heights were mapped on the surface temperature along the mean wind direction using the advection speed of the surface temperature structures and assuming Taylor's frozen turbulence hypothesis. Autocorrelation of the surface and air temperature reveal that they have similar characteristic time scales. By calculating cross-correlations between the air and the surface temperature, previous studies by Katul et al. (1998) and Garai & Kleissl (2011) showed that the surface temperature structures are advected by higher level winds. The cross-correlation between the air temperature of 8 m sonic and the surface temperature showed correlations up to 0.3 – 0.4 for the moderately unstable regions considered. The upwind surface temperature precedes the air temperature at the measurement location, and vice-versa. The advection speeds were shown to be similar to the 8 m a.g.l. wind speed by cross-correlating the air temperature of different heights with the surface temperature along the mean wind direction Garai et al. (2013). Figure IV.1 shows that warm (cold) air is generally associated with positive (negative) vertical velocity due to its buoyancy, as expected in a CBL. Air temperature is correlated with the surface temperature. Small discrepancies in the air and surface temperature structures can be attributed to variations in the wind direction violating Taylor's hypothesis. Also the air and surface temperature structures are of the same order in space and time. The mean size of the surface temperature structures increases with the decrease in the instability of CBL. The measured standard deviation of surface temperature revealed that the surface temperature fluctuations are representative of a grass surface.

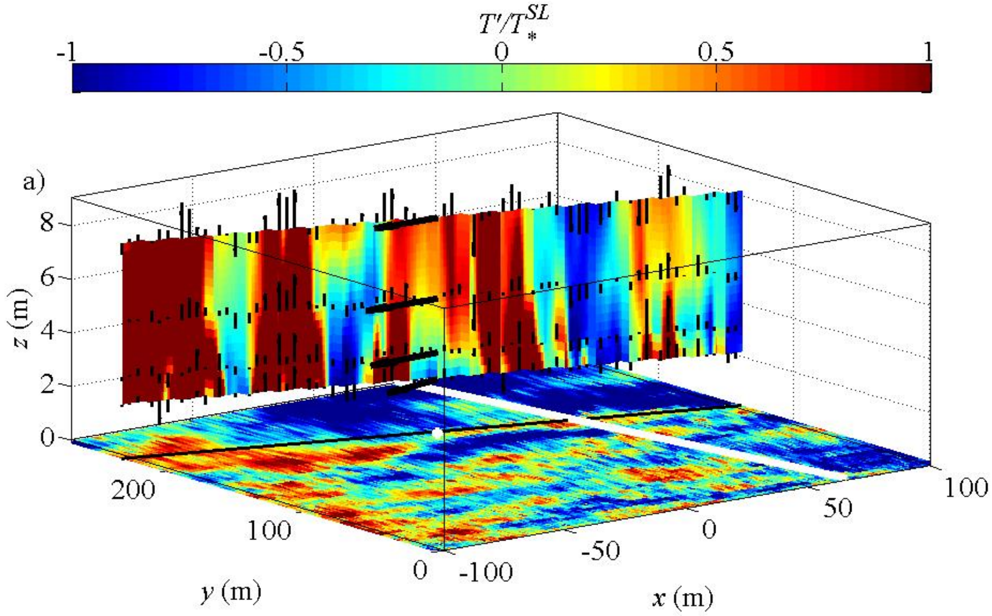

Figure IV.1. Spatial behavior of the surface temperature and air temperature (normalized by surface layer temperature scale) at different heights for (a) $L = -6.68$ m at 26 June 0849 UTC and (b) $L = -14.33$ m at 25 June 0921 UTC. The thick white line represents the road, the white circle represents the position of the turbulence measurement tower, and the black line represents the 30 min mean wind direction in the $z = 0$ plane. The thick black vectors represent wind speed at 2, 3, 5 and 8 m a.g.l. (large vector is 2.5 m s^{-1}), and thin black vectors represent vertical velocity normalized by the convective velocity scale (largest vertical vector represents 1 m s^{-1}) in the vertical plane. Please note that the viewing angle for (a) and (b) are different for better visualization as the wind directions are different.

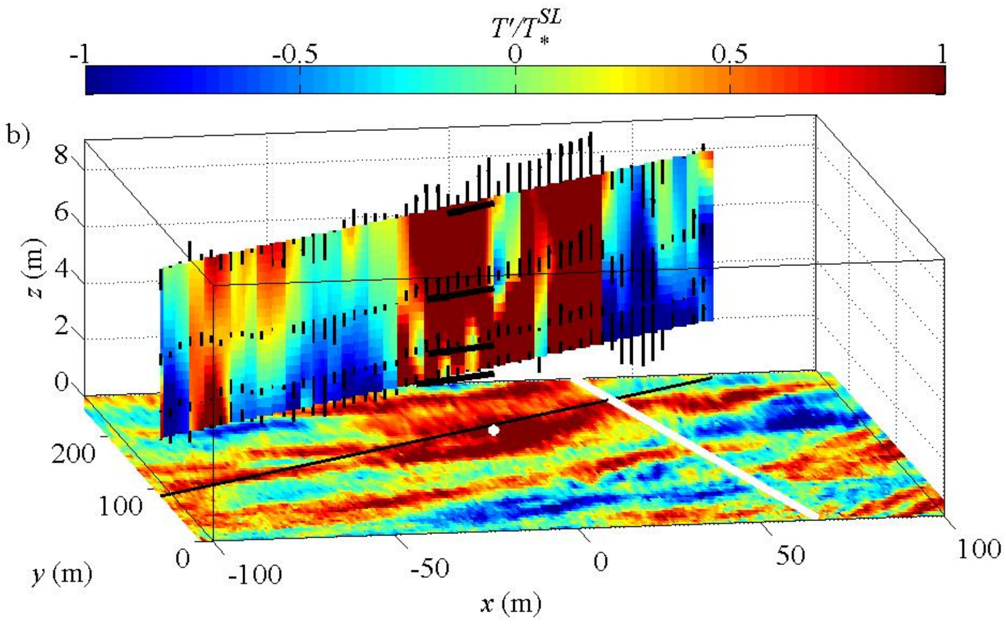

Figure IV.1. Cont.

IV.2.2 Temperature spectra

The statistical behavior of the air and surface temperature fluctuations was then studied using spectral analysis. To reduce the noise of the spectral density, ensemble averages of three 10 min intervals in a 30 min stationary period were computed. In addition, a linear fit was applied to spectral densities for smaller frequencies ($f < 0.005$ Hz); spectral densities at higher frequencies were filtered with logarithmically spaced windows (Figure IV.2).

The air temperature spectral density closely follows the classical −5/3 Kolmogorov law in the inertial range (Figure IV.2c) except near the surface ($z < 0.8$ m). Near the surface, small scale fluctuations of the air temperature become more energetic, causing it to decay slower than the −5/3 Kolmogorov law. The strength of higher frequency air temperature fluctuations decreases with height, while that of low frequency fluctuations remains of the same order. Near the surface (Figure 3-aii and 3-bii, $z < 0.8$ m for our data) the temperature spectral density does not change with height.

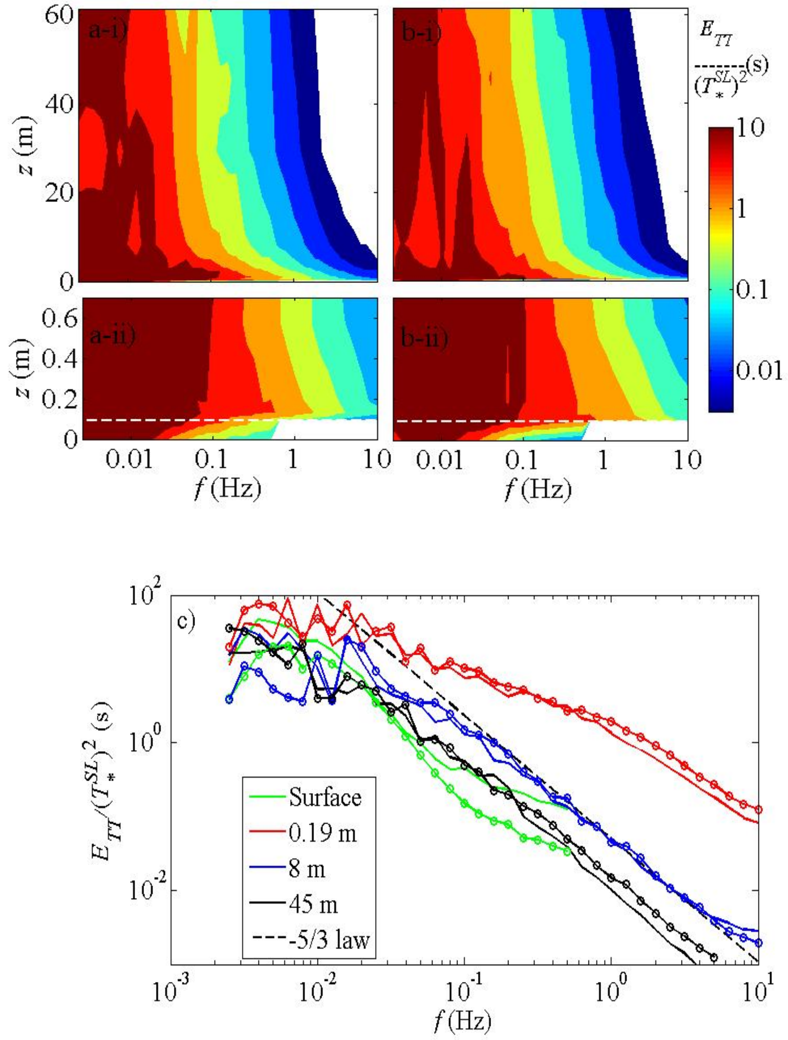

Figure IV.2. Normalized spectral density $\left({}^{E_{TT}}/_{(T_*^{SL})^2}\right)$ of temperature with height for L = a) −6.68 m and b) −14.33 m. The upper panel (i) shows normalized E_{TT} in the surface layer (both the lower and upper surface layer region) and the lower panel (ii) emphasizes the near-surface region. Since the operating frequencies of the temperature sensors were different at different heights, the regions with missing spectral components are marked white. The lowest available air temperature measurement is marked by a broken white line. (c) Comparison of normalized spectral density at four heights with classical −5/3 law for L = −6.68 m (without marker) and −14.33 m (with marker).

IV.2.3 Scaling of r.m.s. temperature

The normalized air temperature standard deviation (the integral of the temperature spectral densities) also decreases with height (Figure IV.3) following the surface layer similarity theory: ${\sigma_{Ta}}/{T_*^{SL}} = 0.95\left(-{z}/{L}\right)^{-1/3}$ (Wyngaard et al. 1971). Very close to the surface (0.09 m < z < 0.8 m) where the spectral density does not change with height, the normalized air temperature standard deviation deviates from similarity theory. Previous studies also reported the deviation of ${\sigma_{Ta}}/{T_*^{SL}}$ from similarity theory for small $-z/L$. In a less unstable (larger $-L$, such that $-z/L$ smaller) CBL, (De Bruin et al. 1993; Andreas et al. 1998; Liu et al. 1998; Tampieri et al. 2009) reported that ${\sigma_{Ta}}/{T_*^{SL}}$ asymptotes to about 3, whereas Ramana et al. (2004) reported the asymptote value to be 6.56. Our measurements close to the ground (smaller z), show that the asymptote value of ${\sigma_{Ta}}/{T_*^{SL}}$ is larger than 3 for smaller $-z/L$. Thus, the discrepancy of ${\sigma_{Ta}}/{T_*^{SL}}$ very close to the surface, while consistent with the spectra analysis in section 3b, indicates a failure of Monin-Obukhov similarity theory.

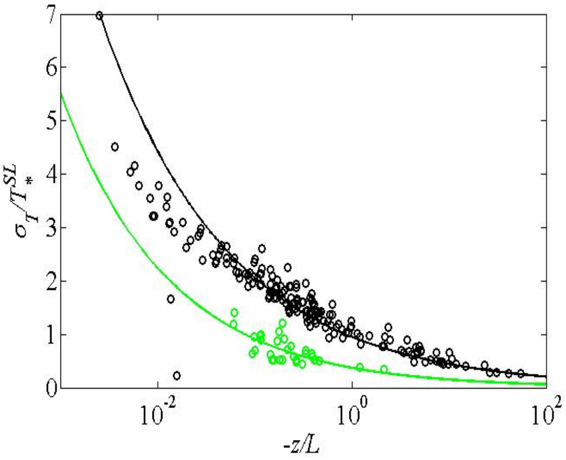

Figure IV.3. Normalized temperature standard deviation for air (black circles) and surface (green circles) as a function of stability parameter. The black solid line represents the surface layer similarity theory (Wyngaard et al. 1971); the green solid line represents the fitted equation for surface temperature. De Bruin et al. (1993); Andreas et al. (1998); Liu et al. (1998); Tampieri et al. (2009) and Ramana et al. (2004) reported ${\sigma_T}/{T_*^{SL}}$ asymptotes to 3 and 6.56 for less unstable boundary layer, i.e. smaller $-z/L$ value.

Since the spectra for surface temperature decay fast with frequency compared to very near surface air temperature, ${\sigma_{Ts}}/{T_*^{SL}}$ is smaller (Figure IV.3), but it follows a power law exponent (${\sigma_{Ts}}/{T_*^{SL}} = -0.36(-\zeta)^{-0.39}$, where ζ = 2.23 m/L for Case L and 2.4 m/L for Case S) comparable to the one predicted by similarity theory. The measured σ_{Ts} for a solid-fluid coupled heat transport depends on the thermal activity ratio, *TAR* (= $\frac{k_f}{k_s}\sqrt{\frac{\alpha_s}{\alpha_f}}$, where k and α are thermal conductivity and thermal diffusivity of the fluid, subscript "*f*", and the solid, subscript "*s*") (Tiselj et al. 2001; Balick et al. 2003). Assuming thermal properties of air (k_f = 0.025 W m^{-1} K^{-1}, α_f = 20 mm^2 s^{-1}), the homogeneous clay soil with 40 % volumetric water content (k_s = 0.8 W m^{-1} K^{-1}, α_s = 0.4 mm^2 s^{-1}) and the grass with 1000 leaves m^{-2} and a weight of 10^{-3} kg per leaf (k_s = 0.38 W m^{-1} K^{-1}, α_s = 19.62 mm^2 s^{-1})

gives *TAR* = 0.0044 for the soil-air and = 0.07 for the grass-air heat transport mechanisms. Although DNS results by Tiselj et al. (2001); Hunt et al. (2003) should be compared with field experiment data cautiously due to the disparity in the Reynolds number, the strength of instability, and the moisture transport, the estimated values of σ_{Ts} by Tiselj et al. (2001); Hunt et al. (2003) revealed that the present σ_{Ts} is more consistent with the heat transport from grass to air Garai et al. (2013).

IV.2.4 Temperature probability density function

To investigate the cause of the behaviour of temperature spectral density with height in the surface layer, we move our attention towards the evolution of the temperature probability density function (pdf) and vertical velocity with height (Figure IV.4). The temperature pdfs above $z \approx 1$ m show distinct characteristics: i) the high probability density region is concentrated towards negative temperature, ii) a short tail for negative temperature, and iii) a long tail for positive temperature fluctuations (Figure IV.4i). The most probable value (mode) increases with measurement height. The *magnitude* of vertical velocity corresponding to the negative temperature fluctuations is smaller than that corresponding to the positive temperature fluctuations. As cold fluid descends, the temperature difference to the warm superadiabatic background increases, but the close proximity to the surface causes the magnitude of its vertical velocity to decrease. This phenomenon results in the slow downdraft of cold fluid parcels. On the other hand, warm fluid ascends and accelerates through the boundary layer due to buoyancy. Thus the warm fluid near the surface causes larger velocities and more intermittent updraft events. Similar characteristics of air temperature probability density functions were observed by Liu et al. (2011).

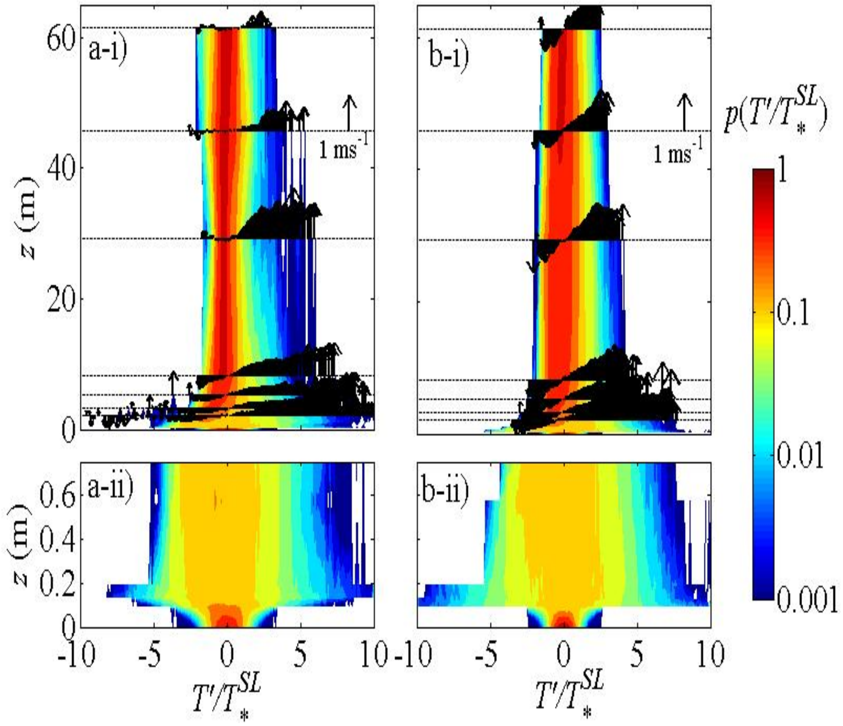

Figure IV.4. Evolution of the temperature probability density function with height for *L* = a) −6.68 m and b) −14.33 m. The upper panel (i) shows the probability density function in the surface layer (both the lower and upper surface layer region)and the lower panel (ii) emphasizes the near-surface. Vertical velocity averaged over each temperature bin is overlaid.

Very close to the surface (z < 0.8 m), the characteristics of the temperature pdf change (Figure IV.4ii). Since more of the total variance is due to small scale events (Figure IV.3), the temperature fluctuations become almost normally distributed. Likewise at the surface the temperature pdf is normally distributed, but the spread of the surface temperature distribution is smaller compared to the very near-surface air temperature distribution.

Comparing Figure IV.4a with IV.4b, the spread of the temperature fluctuations for different stationary periods also depends on stability. As the boundary layer becomes less unstable, the spread decreases, irrespective of the height considered. This is a result of the decrease in relative strength of buoyancy compared to shear, which reduces the occurrence of large intermittent buoyant events.

IV.2.5 Conditional averaging to identify interaction of sweeps and ejections with surface temperature

To explain the characteristics of temperature spectral density and pdf, conditional averaging was employed to study the dominant coherent structures. The ejection events in the surface layer were identified using turbulence signals at a height h by $w'T_a{}'_h > 0.5\langle w'T_a{}'\rangle_h$ with positive w' and the sweep events are identified by $w'T_a{}'_h > 0.25\langle w'T_a{}'\rangle_h$ with negative w'. The chosen cut-off values ensure positive identification of large events, yet select enough events to achieve statistical convergence. The higher cut-off value for ejection events compared to sweep events is motivated by the increased strength of ejection events compared to sweep events (Wilczak & Tillman 1980; Wilczak & Businger 1983). Since temperature data was not available for z > 60 m, coherent structures were identified through the LIDAR vertical velocity signal w, which results in the detection of similar events as below 60 m since vertical velocity and temperature are highly correlated in an unstably stratified boundary layer. From the LIDAR data, ejection and sweep events are identified by $w'_h > 0.4\sqrt{\langle w^2\rangle_h}$ and $w'_h < -0.4\sqrt{\langle w^2\rangle_h}$ respectively. Additional requirements for an event were: (i) a minimum duration, (ii) a minimum separation between two consecutive events (criteria varied as a function of height *h*) as described below, and (iii) passing a visual inspection. Since the duration of each ejection (sweep) event is different, time was normalized by the individual ejection (sweep) time scale such that $t = 0$ and 1 indicates the start and end of the ejection (sweep) event respectively. Though the quantitative value of the statistics derived from the ejection and the sweep events will depend on the definitions (i.e. the thresholds), the qualitative nature of the statistics is independent of the definitions.

IV.2.5.a Lower surface layer and near-surface

The ejection and sweep events in the lower surface layer (0.8 m < z < 10 m) and near-surface (z < 0.8 m) were identified using the turbulence signals at 8 m a.g.l. with a minimum time scale of 3 s and minimum separation between events of 5 s. These criteria result in 20 to 30 ejection events (30 to 40 sweep events) per stationary period with time scales ranging from 3 s to 45 s (3 s to 60 s). The separation between the ejection and sweep events is about 5 – 15 s, whereas that between the sweep and ejection events is about 15 – 45 s. The ejection and sweep events together represent 60% of the 30 min periods with most of the air temperature (80%) and vertical velocity (70%) variance, and are solely responsible for the sensible heat flux (about 100%) for all the stationary periods (Table IV.1).

During the initiation of ejection events, as the air warms, it gains buoyancy. With sufficient buoyancy the warm air parcel ascends from the surface to constitute surface layer plumes and as they rise further, they combine with each other to create larger plumes. When the plumes ascend through the boundary layer, convergence near the surface causes cold air to descend. Hence, the air temperature trace through plumes in the lower surface layer shows a ramp-like pattern; air temperature slowly increases during the initial part of the ejection, attains a maximum at the end of ejection event, and drops quickly during the transition from ejection to sweep event (Figure IV.5). Small scale ramps are overlaid on the large ramp and the number of small ramps was found to decrease with height (visual examination on individual ejection events revealed about 4 to 5 small ramps at 0.5 m a.g.l. and 2 to 3 small ramps at 8 m a.g.l. on a large ramp) as small scale fluctuations decrease with height (Figure IV.2).

Table IV.1. Contribution of the ejection and sweep events at different a.g.l. towards the vertical velocity, air temperature variances and turbulent heat flux. For event identification criteria at different a.g.l. please refer to the text. Since at 200 m a.g.l. no temperature measurements were available the respective columns are empty.

Conditional averaging height, *h*	Contribution to 30 min. period (%)		Contribution to *w'* variance (%)		Contribution to T_a' variance (%)		Contribution to *w'*T_a' (%)	
	Ejection	Sweep	Ejection	Sweep	Ejection	Sweep	Ejection	Sweep
8 m a.g.l.	20-25	30-40	30-40	30-40	45-55	25-35	60-70	30-40
45 m a.g.l.	15	20-30	30	30-35	30	25-35	50-60	40-50
200 m a.g.l.	35-40	50-60	25	20	-	-	-	-

The interaction between surface and air during the event also offers unique insights. As the near-surface air warms up during the initial phase of the ejection event ($t < 0.5$), the heat flux from the surface to air decreases. Thus the surface energy budget causes warming of the surface and an increase in ground heat flux. When the warm air ascends from the surface ($0.5 < t < 1$), the majority of the heat exchange between the surface and air occurs, resulting in cooling of the surface. The surface temperature is only influenced by the large scale plume (Figure IV.5ii) and not by smaller plumes apparent in the air temperature. As the probability density functions and spectra from the two different camera fields of views (and associated difference in horizontal resolution) of the IR camera are similar, we conclude that the lack of small scale plume signatures is not an artifact of insufficient spatial resolution. It might be due to the larger thermal inertia of the surface or insufficient temporal resolution of the measurements, as mentioned earlier.

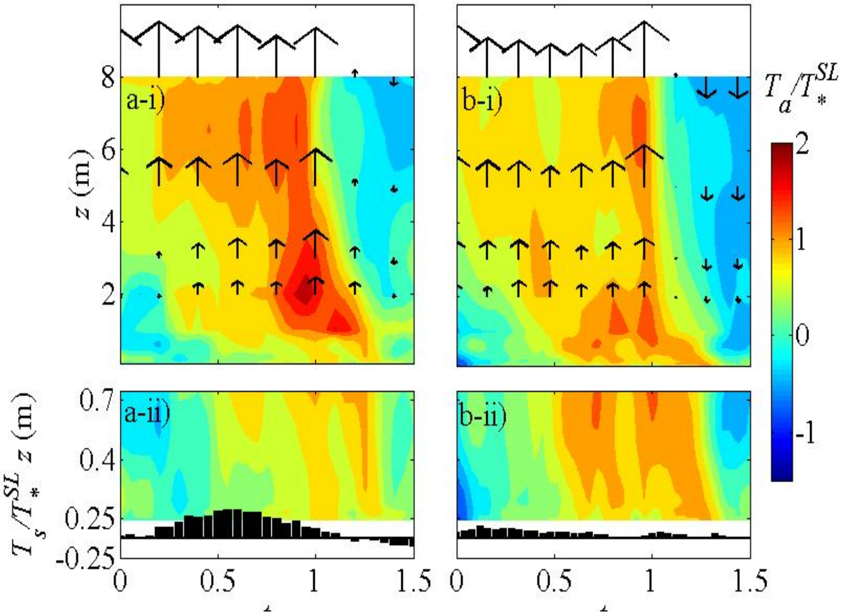

Figure IV.5. Evolution of ejection events in the near-surface ($z < 0.8$ m, lower panel (ii)) and the lower surface layer (0.8 m $< z < 10$ m, upper panel (i)) for L = a) −6.68 m and b) −14.33 m. The colour scale represents air temperature and black bars (in ii) represents surface temperature (both normalized by the surface layer temperature scale) and black arrows indicate conditionally averaged vertical velocity (largest vector corresponds to 0.42 w_*). The time axis is normalized by the length of individual ejection events such that $t = 0, 1$ represents the start and end of the ejection event at 8 m a.g.l.

In a sweep event (Figure IV.6) cold air approaches and cools the surface. As the cold air parcel descends, its vertical velocity decreases due to the proximity of the surface. At ($t > 0.5$) the heat transport from the surface to air starts to decrease, resulting in an increase in surface temperature and ground heat flux. Also note that the 8 m air temperature during sweep events ($0 < t < 1$ in Figure IV.6) remains almost constant compared to during ejection events ($0 < t < 1$ in Figure IV.5). During the transition from sweep to ejection ($t > 1$), the air temperature slowly increases, in contrast with the sharp transition from ejection to sweep.

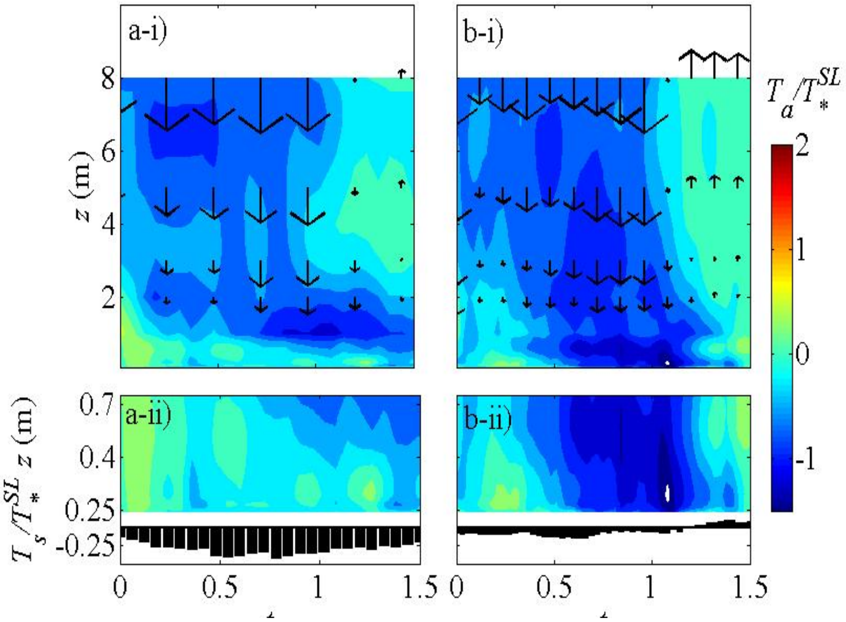

Figure IV.6. Evolution of the sweep events in the near-surface ($z < 0.8$ m, lower panel (ii)) and the lower surface layer ($0.8 \text{ m} < z < 10$ m, upper panel (i)) for L = a) −6.68 m and b) −14.33 m. The colour scale represents air temperature and black bars (ii) represent surface temperature (both normalized by the surface layer temperature scale) and black arrows indicate conditionally averaged vertical velocity (magnitude of the largest vector corresponds to 0.3 w_*). The time axis is normalized by the length of individual sweep events such that t = 0, 1 represents the start and end of the sweep event at 8 m a.g.l.

Consequently, the combination of sweeps and ejections causes the air temperature trace in the lower surface layer to be sawtooth-like: almost constant during the sweep, gradual increase until the end of the ejection, and thereafter a sharp drop. On the other hand the surface temperature increases and decreases smoothly. With increase in stability, background shear increases and thus the tilt of the plumes is also expected to increase especially near the surface as confirmed in the figures.

IV.2.5.b Upper surface layer

The coherent structures in the upper atmospheric surface layer (10 m $< z <$ 0.1z_i) were detected using the turbulence measurements at h = 45 m. As larger scale turbulent motions become more energetic with height (Figure IV.2), we used 15 s as minimum timescale of an event and 5 s as minimum separation between events. These criteria result in 8 to 10 ejection events (about 12 sweep events) per stationary period with time scales ranging from 15 s to 60 s (15 s to 90 s). The separation between the ejection and sweep events is about 5 – 10 s, whereas that between the sweep and ejection events is about 10 – 20 s. The ejection and sweep events together represent about 45% of the 30 min periods with most of the air temperature (about 50%) and vertical velocity (about 60%) variance, and are solely responsible for turbulent heat flux (about 100%) (Table IV.1).

For the upper surface layer events, the plumes also imprint on the surface as warm structures, whereas the cold sweep events imprint on the surface as cold structures (Figure IV.7). As the IR camera field of view was smaller during Case S, the pixel size is smaller compared to that during Case L, which may be the cause of more small scale fluctuations in the conditionally averaged surface temperature. However, the smaller number of events may also be a contributing factor.

In the upper surface layer the magnitude of temperature fluctuations decreases compared to the lower surface layer. Compared to the lower surface layer, the plume characteristics in the upper surface layer are that i) the increase in air temperature across the plume is smaller and ii) the drop in air temperature after the ejection event is sharper. The sharper drop of temperature after the ejection event can be attributed to the increase in vertical velocity with height, causing stronger convergence of the flow at the ejection-sweep transition.

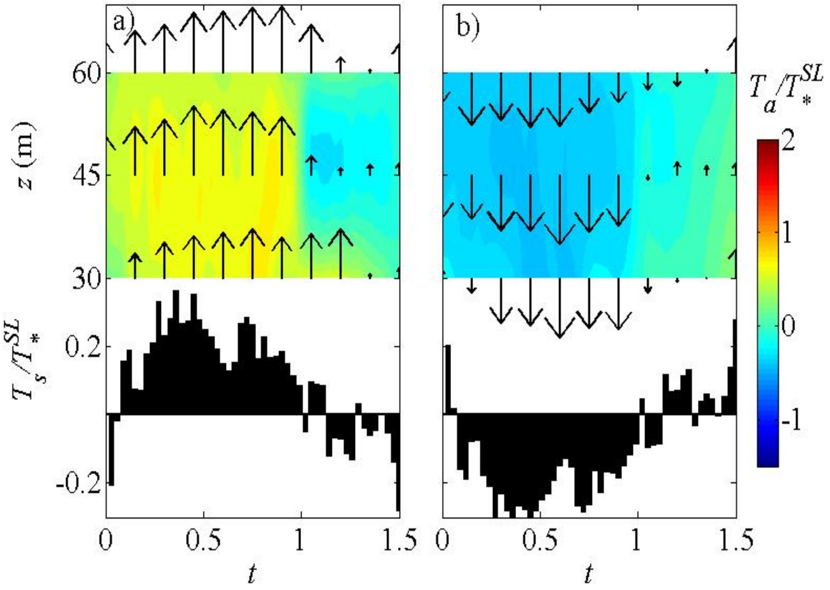

Figure IV.7. Evolution of the a) ejection and b) sweep events in the upper surface layer for *L* = −6.22 m. The colour scale represents normalized air temperature and the black bars represent normalized surface temperature (both normalized by the surface layer temperature scale) and black arrows indicate conditionally averaged vertical velocity (the largest vectors correspond to 0.75 and 0.4 w_* for ejection and sweep event, respectively). The time axes are normalized by the length of individual ejection and sweep events such that *t* = 0, 1 represents the start and end of the ejection and sweep event at 45 m a.g.l. for panels (a) and (b) respectively.

As the small scale plumes ascend from the lower surface layer to the upper surface layer, they merge with each other to create large plumes, which results in almost constant temperature inside the plumes in the upper surface layer, in contrast with the lower surface layer. Thus the characteristic ramp-like pattern of the air temperature trace also changes with height: constant during the sweep, gradual increase during the transition from sweep to ejection, *constant during the ejection*, and *rapid decrease during* *the transition from ejection to sweep*. The tilt of the plumes is reduced due to the decrease in background shear with height.

IV.2.5.c Mixed layer

To study the mixed layer ($0.1 < z/z_i < 1$) turbulent structures, h = 200 m ($h/z_i = 0.4$ for the stationary period considered) with 60 s as minimum time scale and minimum separation between two consecutive events was used. These criteria result in about 4 ejection and sweep events (accounting for 45% of vertical velocity variance) in the 30 min stationary periods (Table IV.1) and the separation between them is about 5 – 10 s. The average time scale (of about 3 – 5 min) for ejection or updrafts and sweep or downdrafts is consistent with the eddy turn-over time scale (z_i/w_*) for the CBL.

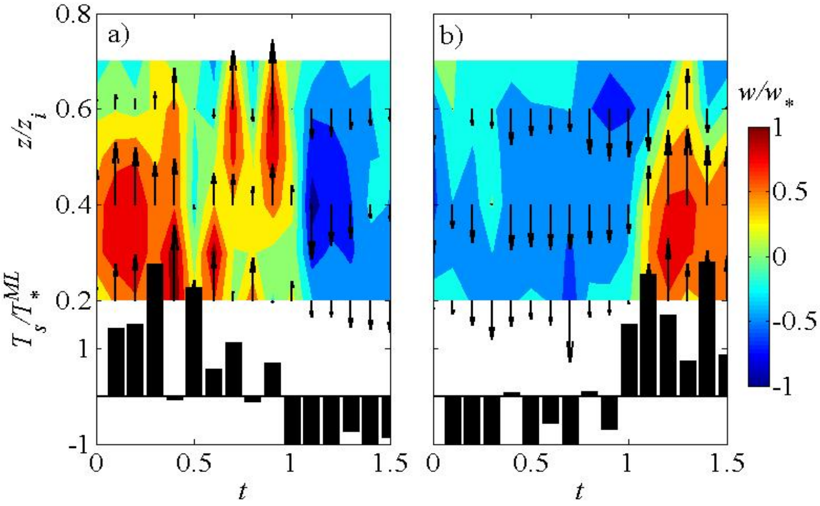

Figure IV.8. Evolution of the a) thermals and b) downdraft events in the mixed layer for $L = -14.33$ m. The time axes are normalized by the length of individual thermals and downdraft events such that t = 0, 1 represents the start and end of the thermals and downdraft event at 200 m a.g.l. for panels (a) and (b) respectively. The colour scale represents vertical velocity normalized by the convective velocity scale, black bars represent surface temperature normalized by the mixed layer temperature scale, and black arrows indicate conditionally averaged vertical velocity.

Thermals in the mixed layer are formed from the merging of several surface layer plumes and surface layer sweep events are caused by cold downdraft from the mixed layer. Thus the surface temperature shows warm structures beneath the thermals and cold structures beneath the downdrafts (Figure IV.8). Since the boundary layer is well mixed in this region, the background shear is negligible. Thus the thermals and downdraft in the mixed layer show almost no tilt. The magnitude of the vertical velocity decreases with height ($z/z_i > 0.5$) due to stably stratified capping inversion. The vertical velocity standard deviation peaks at $z/z_i \approx 0.3 - 0.4$, consistent with other experimental observations and numerical simulations of the CBL (Deardorff & Willis 1985; Lenschow & Boba Stankov 1986).

IV.2.6 Heat fluxes at the earth's surface

The effect of the plumes and sweeps in the surface layer; and thermals and downdrafts in the mixed layer on the surface energy budget is now investigated

$$R_{net} - G = H + LE + S, \qquad \text{(IV.1a)}$$

where R_{net}, G, H, LE and S are the net radiation, ground heat flux, sensible heat flux, latent heat flux and heat storage by the canopy, respectively. Since our experimental site is covered only by grass and our stationary periods occur well outside of sunrise and sunset, the canopy storage term is negligible (Garai et al. 2010). Also, since high frequency humidity measurements were not available near the surface, we have estimated the latent heat flux from the Bowen ratio, B, at 29.3 m a.g.l. Thus Equation 3a becomes

$$R_{net} - G \approx H\left(1 + \frac{1}{B}\right). \qquad \text{(IV.1b)}$$

Assuming R_{net} to be constant within the 30 min stationary (cloud-free) periods, the coherent structure induced H variation should then be balanced by G.

Though the measured T_s is of the most representative of grass, we solved the 3D transient heat conduction equation (Equations II.4) using the thermal properties of the homogeneous clay soil with 40% volumetric water content. The resulting normalized ground heat flux ($G/<G>$) will be independent of surface thermal property as the heat conduction equation is linear.

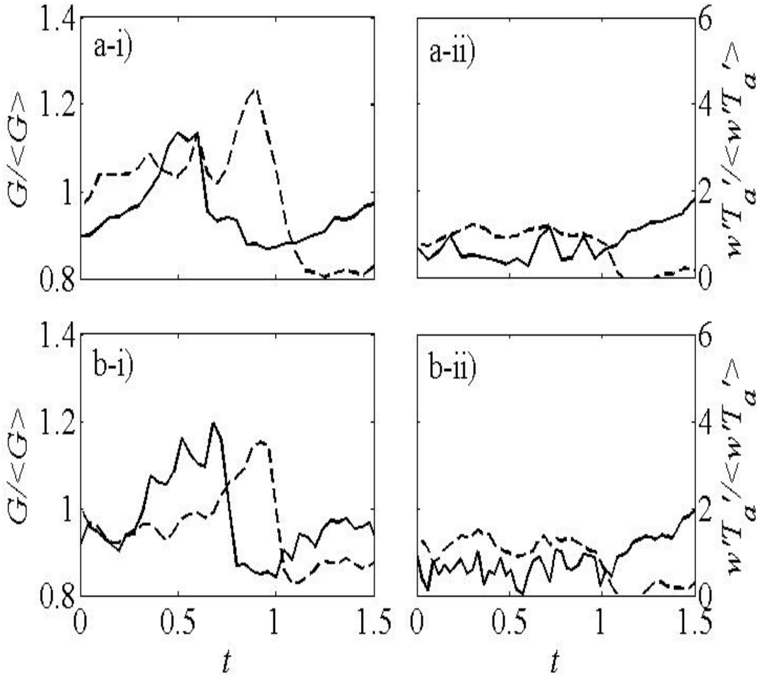

Figure IV.9. Evolution of normalized ground heat flux ($G/<G>$, solid line, left axes) and normalized turbulent heat flux at 8 m above the ground ($w'T_a'/<w'T_a'>$, broken line, right axes) during (i) ejection and (ii) sweep events for L = (a) −6.68 m and (b) −14.33 m. The time axes are normalized by the length of individual ejection and sweep events such that t = 0, 1 represents the start and end of the ejection and sweep event at 8 m a.g.l. for panels (i) and (ii) respectively.

During ejection and sweep events, computed G and measured $w'T_a'$ at 8 m a.g.l. show similar behaviour for different stationary periods (Figure IV.9). The majority of heat transport from the surface to air occurs during the end of the ejection event (reference also Figure IV.5). Thus G attains a minimum during this time following Equation IV.1b. During the initial phase of the ejection, $w'T_a'$ increases and the ground heat flux, G, attains a maximum. During the sweep event cold air descends to the ground, heat transport from surface to air decreases compared to the ejection period (since the ground is cold, cf Figure IV.6), and G is also depressed. As these cold air parcels near the surface warm up, even less heat will be transferred from the surface to the air, and G starts to increase. Thus the ground heat flux succeeds the turbulent heat flux. For our data, during the ejection event turbulent coherent structures cause the turbulent heat flux to be about 4 times the average and the ground heat flux to be about 1.2 times the average.

Since high frequency humidity data were not available, we could not demonstrate the behavior of latent heat transport and how it influences the ground heat flux through a decoupling from the sensible heat flux that violates the assumption in Equation IV.1b. Also, for this comparison we have neglected the influence of mechanical heat transport ($\frac{d}{dx}\int_0^h uTdz$) by horizontal wind (since we are comparing G at $z \approx 0$ m with $w'T_a'$ at $z =$ 8.22 m). Since during the sweep event the fluid velocity is high with low temperature and during the ejection event the fluid velocity is low with high temperature, the missing dynamical estimates of latent heat and mechanical heat transport can account for the imperfect balance between *G* and *H* which has been discussed in the context of Equation IV.1b.

IV.3 Conclusions

In this work we studied turbulent coherent structures and their influence on the surface temperature and ground heat flux in a CBL experimentally for a wide range of stabilities and found that the larger scales of turbulent heat transport dominate the surface temperature variations. Surface layer turbulence is dominated by plumes/ejections and sweep events. During sweep events, cold air descends, while during ejection events plumes of warm air ascend from the surface layer through the boundary layer due to buoyancy. Near the surface small scale plumes are overlaid on a large scale plume and these small scale plumes merge with each other to create a large plume in the upper surface layer. Thus the temperature trace across the ejection and sweep event in the middle part of the surface layer is constant during the sweep, slowly increases during the transition from sweep to ejection, attains a maximum during the ejection and then drops quickly during the transition from ejection to sweep (ramp like pattern). In the upper surface layer the trace during the sweep-ejection-cycle is similar with the exception that temperature is constant during the ejection. The sweep-ejection-cycle can also be explained using surface renewal analysis (Paw U et al. 1995). Thus the temperature probability density function shows an exponentially decaying short negative tail with a long positive tail except near the surface. Near the surface a greater abundance of small scale plumes and sweeps makes the temperature pdf close to Gaussian. The spectral density in small scale or high frequency fluctuations decays with height, whereas the spectral density in low frequency fluctuations remains similar with height.

Sweep and ejection events account for most of the temperature and vertical velocity variance and turbulent heat flux, with the majority of the contribution from ejection events. The durations of sweep and ejection events are generally similar except in the lower surface layer (time scales for sweep events are larger near the surface). The durations increase with height and the combination of a sweep and an ejection is close to the convective eddy turn-over time in the mixed layer.

The unique aspect of our study was the observation that these coherent structures – from the lower and upper surface layer and the mixed layer – imprint on the ground heat flux and surface temperature. The ground heat flux precedes the turbulent heat flux and shows a similar pattern during sweeps and ejections, but the surface temperature increases and decreases more gradually, which is distinct from the ramp pattern in air temperature. Similar patterns of temperature of air and surface were also observed in direct numerical simulations (at much lower Reynolds number) by Hunt et al. (2003). We also found that small scale plumes do not imprint on the surface, which might be due to the larger thermal inertia of the ground.

Near-surface air temperature standard deviations deviate from the surface layer similarity theory (Wyngaard et al. 1971). Previous studies by De Bruin et al. (1993); Andreas et al. (1998); Liu et al. (1998); Tampieri et al. (2009); Ramana et al. (2004) reported that the normalized air temperature fluctuation asymptotes to about $3-6$ for small stability (parameterized as *z/L*). Although the measured standard deviation from the near-surface thermocouple data may suffer from missing high frequency components (the lowest thermocouple is at the height of the roughness elements), the asymptotic value is greater than 3. Surface temperature fluctuations show a similar power law exponent with z/L as in surface layer similarity theory.

Present state-of-the-art large eddy simulations use constant heat flux or constant temperature at the surface. Atmospheric and laboratory scale observations demonstrate that neither choice of the boundary conditions is realistic. Direct numerical simulations by Tiselj et al. (2001); Hunt et al. (2003) reveal that the near surface turbulence characteristics are functions of surface thermal properties. The present study demonstrates through measurements that both the surface temperature and ground heat flux show evidence of turbulent coherent structures. This proves the necessity of improved wall functions for modeling turbulent heat transport.

Acknowledgements: Content of this chapter has been published in Garai A, & Kleissl J, 2013, Interaction between coherent structures and surface temperature and its effect on ground heat flux in an unstably stratified boundary layer. *J. Turbul.*, in press. The dissertation author was primary investigator and author of this paper.

Chapter V

Surface temperature and boundary layer instability

V.1 Introduction

The fluid temperature trace in turbulent heat transfer over a flat surface shows the characteristics of periodic activities comprised of alternating large fluctuations and periods of quiescence (Townsend, 1959; Howard, 1966). Sparrow et al. (1970) observed that these periodic activities are due to mushroom-like structures of ascending warm fluid caused by instability due to buoyant forcing (Howard, 1966). Similar structures consisting of ascending warm fluid are also observed in the surface-layer of a convective boundary layer (CBL) and known as surface-layer plumes. These plumes have diameters on the order of the surface-layer height, advection velocities close to the average wind-speed over their depth, are tilted by about 45^0 due to wind shear, and are responsible for the majority of total momentum and heat transport (Kaimal and Businger, 1970; Wyngaard et al. 1971; Kaimal et al. 1976; Wilczak and Tillman, 1980; Wilczak and Businger, 1983; Renno et al. 2004). As these plumes ascend through the CBL, they combine with each other to create thermals in the mixed-layer.

Conditional averaging of surface-layer plumes by Schols (1984) and Schols et al. (1985) revealed that the resulting air-temperature trace shows ramp-like patterns. Gao et al. (1989), Paw U et al. (1992), Braaten et al. (1993) and Raupach et al. (1996) studied these temperature ramp patterns over different canopies and modelled the transport process using the surface renewal method. The surface renewal method conceptualizes the heat exchange process to occur based on coherent structures: a cold air parcel descends to the ground during the sweep event, while it remains close to the ground it is heated, and when it achieves sufficient buoyancy the warm air parcel ascends during the ejection event. The surface renewal method has been successfully employed to estimate sensible and latent heat-fluxes over different canopies by Paw U et al. (1995), Snyder et al. (1996), Spano et al. (1997, 2000), Castellvi et al. (2002), Castellvi (2004) and Casstellvi and Snyder (2009).

The effect of coherent structures on the surface-temperature was first observed by Derksen (1974) and Schols et al. (1985) who found streaky patterns of surface-temperature with about a 2 ℃ heterogeneity along the wind-direction using an airborne thermal infra-red (IR) camera. Hetsroni and Rozenblit (1994), Hetsroni et al. (2001), and Gurka et al. (2004) observed a similar streaky structure in surface-temperature in a laboratory convective water flume experiment at different Reynolds numbers. High surface-temperature streaks corresponded to low velocity fluid streaks in the boundary layer and the distance between streaks increased with Reynolds number. Using an IR temperature sensor Paw U et al. (1992), Katul et al. (1998) and Renno et al. (2004) observed surface-temperature fluctuations in the CBL with an amplitude of 0.5 ℃ over 2.6-m high maize crops, greater than 2 ℃ over 1-m high grass, and 2 – 4 ℃ over a desert area, respectively. Using IR imagery, Ballard et al. (2004), Vogt (2008) and Christen et al. (2012) observed spatial heterogeneities in the magnitude of surface-temperature fluctuations over a grass canopy, a bare field, and in an urban environment, respectively.

Direct numerical simulation (DNS) of turbulent heat transfer coupled with heat conduction in the adjacent solid by Tiselj et al. (2001) revealed that the magnitude of surface-temperature fluctuations depends on the wall thickness and relative strength of thermal response times for the solid and fluid. Balick et al. (2003) identified similar key parameters for the coupled heat transfer process at the earth’s surface. Hunt et al. (2003) observed different forms of coherent structures (plumes and puffs) by varying the surface thermal properties in their DNS of the solid-fluid coupled turbulent heat transport process. Ballard et al. (2004) hypothesized that high frequency surface-temperature fluctuations are caused by turbulent mixing. Katul et al. (1998) and Renno et al. (2004) argued that surface-temperature fluctuations are caused by inactive eddy motion and convective mixed-layer processes. Christen and Voogt (2009, 2010) visualized the spatial surface-temperature field in a suburban street canyon and qualitatively attributed the vertical heat transport to the observed coherent structures that were shown to move along the wind-direction.

Garai and Kleissl (2011) examined surface-temperature structures and heat transport processes over an artificial turf field using 1-Hz IR imagery. Although the camera field-of-view was smaller (48 m x 15 m) than the scale of the largest surface-temperature structures, different surface-temperature characteristics were identified corresponding to different phases of the surface renewal process. The surface-temperature field showed large cold structures during sweep events, small patches of warm structures in a cold background during the transition from sweep to ejection, large warm structures during the ejection events, and small patches of cold structures in a warm background during the transition from ejection to sweep. Sequential animation of the surface-temperature showed growth and merging of thermal footprints moving along the wind-direction. Garai and Kleissl (2011) speculated that these atmospheric turbulence driven surface-temperature fluctuations can induce physical “noise” in different applications of remote sensing, such as the identification of land mines, illegal land-fills and the determination of evapotranspiration for irrigation management. For example, several remote sensing models (e.g. the Surface Energy Balance Algorithm for Land (SEBAL) by Bastiaanssen et al., 1998a,b) estimate sensible heat-flux and evapotranspiration using Monin-Obukhov similarity theory, which relies on mean differences between the surface- and air-temperatures. Thus, the substantial deviation of instantaneous surface-temperature measurement by remote sensing platforms from the true mean can degrade the accuracy of local evapotranspiration estimates. The main objective for the present experimental set-up was to address the main limitation of Garai and Kleissl (2011) by increasing the small field-of-view of the IR camera. Furthermore turbulence measurements were collocated at different heights that allowed further investigation of the cause and manifestation of surface-temperature structures as a function of atmospheric stability and the interaction between thermal footprints and lower surface-layer turbulence.

V.2 Results

Data from BLLAST field experiment was used for this study. Details of the experimental campaign and meteorological condition are discussed in Chapter II.3.3.

V.2.1 *Spatial and temporal evolution of surface- and air-temperatures and comparison to similarity functions*

We have chosen the time periods with $L = -10.2$ m and -19.5 m (Chapter II.5) to illustrate stability dependence of surface-temperature and air turbulence data, as they are representative of more unstable and less unstable conditions in our dataset with different wind-directions (177° for $L = -10.2$ m and 91° for $L = -19.5$ m). Structures in the spatial surface-temperature fluctuation field are aligned with the wind-direction (Figure V.1) demonstrating that the observed surface-temperature structures are not an artefact of surface heterogeneity or topography. With time these surface-temperature structures grow, merge with each other, and move along with the airflow.

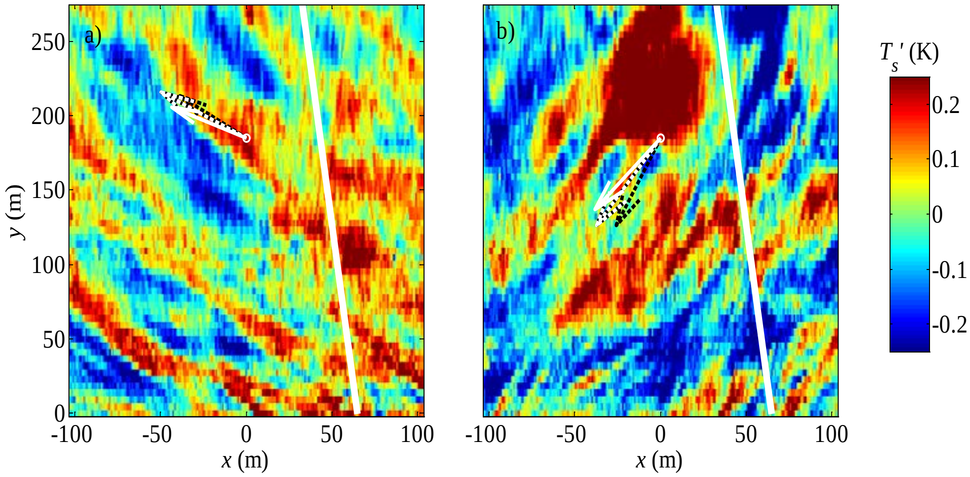

Figure V.1. Snapshots of surface-temperature fluctuations for L = a) −10.2 m at 27 June 0838 UTC, and b) −19.5 m at 26 June 1124 UTC. Arrow lines represent 1-s averaged wind vectors (scaled to the distance covered in 25 sec) at 8 m (black solid), 5 m (black dashed), 3 m (white solid) and 2 m (white dashed) a.g.l. at the measurement location (white circle) respectively. The thick white line represents data excluded due to the road.

The temporal evolutions of surface-temperature and air-temperature fluctuations at different heights are then compared in Figure V.2. The surface-temperature is the average across the scalar footprint of the 2-m CSAT with a cut-off of 10% of the maximum value of the scalar footprint function. Figure V.2 shows that air-temperature and surface-temperature are highly cross-correlated and air-temperature lags surface-temperature since the footprint is upstream: when the surface is cold the air cools and when the surface is warm the air warms. Also, the air-temperature at a lower altitude shows more small-scale fluctuations compared to the surface-temperature. This is due to the fact that the surface-temperature is spatially averaged across the footprint; and not as affected by the small-scale events as air-temperature, since the former has larger thermal intertia compared to the later. Comparing Figures V.2a and V.2b reveals that both surface-temperature and air-temperature show more small-scale fluctuations as the boundary layer becomes more unstable. Similar results are obtained for all other stationary conditions.

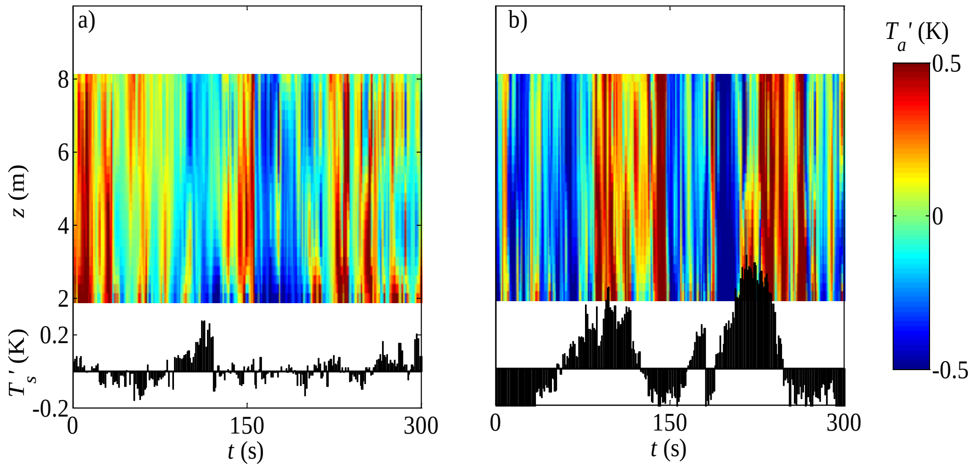

Figure V.2. Time series of air-temperature (colour bar) and footprint-averaged surface-temperature (bar plot) for L = a) −10.2 m at 27 June 0833 − 0838 UTC and b) −19.5 m at 26 June 1122 − 1127 UTC. Air-temperatures were vertically interpolated using spline interpolation. The footprint is the area with greater than 10% of the maximum value of the scalar footprint function of the 2-m CSAT.

Figure V.3 shows temperature standard deviations normalized by the surface-layer temperature scale, T_*^{SL}, for all stationary periods. Normalized σ_{Ta} for 2 m and 8 m a.g.l. decrease with increasing height and stability closely following the surface-layer similarity theory, ${}^{\sigma_{Ta}}/_{T_*^{SL}} = -0.95\left(-{}^{z}/_{L}\right)^{-1/3}$ (Wyngaard et al., 1971). σ_{Ts} is smaller than σ_{Ta} at 8 m a.g.l. and satisfies ${}^{\sigma_{Ts}}/_{T_*^{SL}} = -0.36(-\zeta)^{-0.39}$.

DNS of the solid-fluid coupled turbulent heat transfer by Tiselj et al. (2001) showed that σ_{Ts} depends on the solid thickness and the thermal properties of solid and fluid as in the thermal activity ratio, $TAR = \frac{k_f}{k_s}\sqrt{\frac{\alpha_s}{\alpha_f}}$, where k and α are the thermal conductivity and thermal diffusivity of the fluid (subscript "f") and the solid (subscript

"s"). They found that a fluid-solid combination with low *TAR* does not allow imprints of fluid-temperature fluctuations on the solid surface. Balick et al. (2003) also derived a similar parameter for a coupled land-atmosphere heat transfer model. For our measurement site, one can assume the fluid-solid coupled heat transport to occur between air and homogeneous clay soil, or between air and grass leaves or a combination of both. Assuming k_f = 0.025 W m^{-1} K^{-1} and α_f = 20 mm^2 s^{-1}, for homogeneous clay soil with 40% volumetric water content *TAR* = 0.0044 and for grass leaves with 1000 leaves m^{-2} and a weight of 10^{-3} kg per leaf (i.e. k_s = 0.38 W m^{-1} K^{-1} and α_s = 19.62 mm^2 s^{-1}, Jayalakshmy and Philip (2010)) *TAR* = 0.07. Under these conditions according to Tiselj et al. (2001) σ_{Ts} would be less than 1% for soil and about 10% for grass of its iso-flux counterpart, which corresponds to $TAR \rightarrow \infty$. Thus the air-grass leaf coupled heat transport mechanism better fits our data, as Tiselj et al. (2001) and Hunt et al. (2003) reported non-dimensional surface-temperature standard deviation of 2 when temperature is modelled as passive scalar (normalized by $\frac{H}{\rho_a c_{p,a} u_*}$) and about 3 when wind shear is absent (normalized by $\frac{H}{\rho_a c_{p,a} w_*}$) for their corresponding DNSs, respectively. However, DNS results may not apply to the field measurements, as in them the Reynolds number was low, different strength of stability was used and transport of water vapour was neglected.

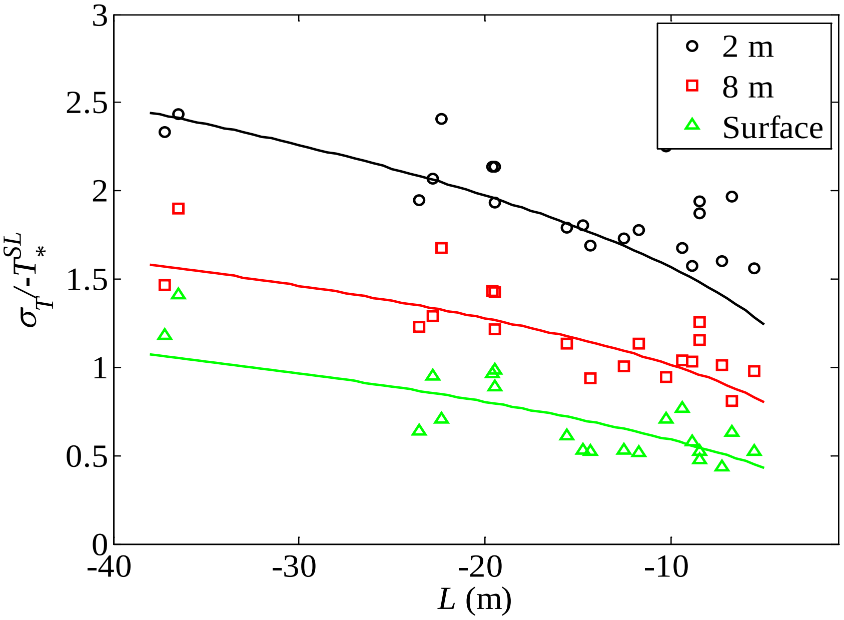

Figure V.3. Normalized variances of surface-temperature and air-temperature as a function of L. The markers are measurements for the periods in Table 1, the black and red solid lines are fitted according to the surface-layer similarity theory $\sigma_{Ta}/T_*^{SL} = -0.95\left(-z/L\right)^{-1/3}$ and the green line is the fitted to the surface-temperature standard deviation: $\sigma_{Ts}/-T_*^{SL} = 0.36(-\zeta)^{-0.39}$.

V.2.2 *Spatial scale of surface-temperature structures*

The spatial scale of surface-temperature structures (as seen in Figure V.1) can be investigated by considering the spatial correlation for each image using

$$\rho_{xy}(\Delta x, \Delta y, t) = \frac{\overline{T_s'(x,y,t)T_s'(x+\Delta x,y+\Delta y,t)}}{\sigma_{Ts}^2} \tag{V.1}$$

where the overbar indicates a spatial average. Figure V.4 shows the temporal average of the spatial correlation of the surface-temperature structures ($\langle\rho_{xy}(\Delta x, \Delta y, t)\rangle$) for L = (a) -10.2 m, and (b) -19.5 m. The surface-temperature correlation structures are shaped as ellipsoids with the major axis aligned with the streamwise direction.

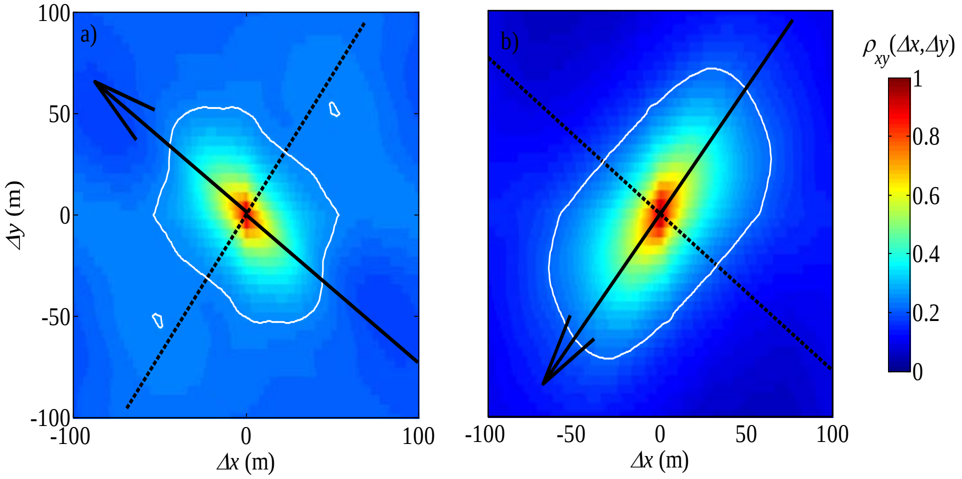

Figure V.4. Mean spatial correlation of surface-temperature for L = (a) −10.2 m, and (b) −19.5 m (in the camera coordinate system). The solid and broken black lines indicate averaged streamwise and spanwise directions over 2, 3, 5 and 8 m a.g.l., respectively. The white contour line indicates a correlation of 0.25.

The spatial properties of coherent structures in a boundary layer flow depend on shear and buoyancy. For a shear-dominated boundary layer, the structures become elongated in the wind-direction and streaky, whereas for a buoyancy-dominated boundary layer, they become more circular. We consider u_* as a measure of shear and ζ as a relative measure of buoyancy to study their effect on the surface-temperature structures. Figure V.5 shows (i) the streamwise correlation length (l_{stream}), and (ii) the aspect ratio ($AR = l_{stream}/l_{span}$, where l_{span} is the spanwise correlation length) against ζ and u_* for all stationary periods. The correlation length is defined as twice the distance from the centre where the correlation becomes 0.25 in the streamwise and spanwise directions (Figure V.4). Though the quantitative values of the streamwise and spanwise lengths will depend on the chosen cut-off correlation, the qualitative behaviour of the streamwise and spanwise lengths with stability and friction velocity are independent of the chosen correlation cut-off value. The spatial scales of surface-temperature structures will also depend on the averaging period, as the camera field-of-view could not capture the largest possible structure in CBL. A 30-min averaging period resulted in structures 20 to 40% larger than those computed using a 5-min averaging period. With increasing stability the structures become streakier. Thus *AR* is close to unity for the more unstable cases and larger than unity for the less unstable cases. Hommema and Adrian (2003) and Li and Bou-Zeid (2011) also reported that as the boundary layer becomes more unstable, the dominant coherent structures in the surface-layer change from long streaky structures due to hairpin packets to surface-layer plumes. l_{stream} does not show any recognizable trend against u_*, but *AR* increases from 1.5 for small u_* to more than 2 for larger u_*. Wilczak and Tillman (1980) reported similar streamwise sizes of coherent structures based on the time traces of air-temperature at 4 m a.g.l.

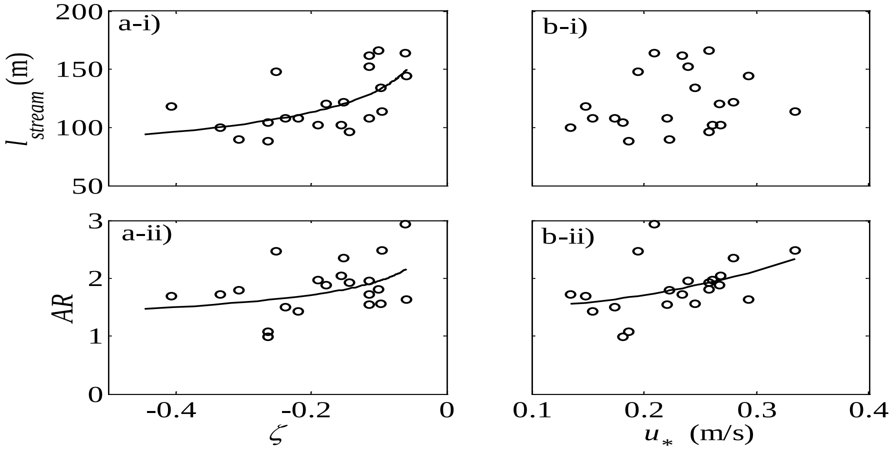

Figure V.5. (i) Streamwise correlation length l_{stream}, and (ii) aspect ratio *AR* of the mean surface-temperature structure with (a) ζ and (b) u_*. Markers represent the measurements and solid lines represent fits: $l_{stream} = 78.03(-\zeta)^{-0.23}, AR = 1.26(-\zeta)^{-0.19}, AR = 11.43u_*^2 - 1.5u_* + 1.55$ with 48.6%, 28.0% and 27.7% coefficient of determination respectively. No trend was observed and no line was fitted for b-i.

V.2.3 *Surface- and air-temperature correlation*

Since the footprint-averaged surface-temperature is correlated with air-temperature (Figure V.2), spatial maps of cross-correlation between surface-temperature and air-temperature were generated using

$$\rho_{Ts,Ta}(x, y, \Delta t) = \frac{\langle T_s'(x,y,t) T_a'(x_o,y_o,t+\Delta t) \rangle}{\sigma_{Ts}\sigma_{Ta}} \quad \text{(V.2),}$$

where x_o and y_o are the coordinates of the sonic tower and the two vectors are lagged by up to $\Delta t = 60$ sec. To reduce noise in the cross-correlation maps, an ensemble average of three cross-correlation maps for each 10-min interval in a 30 min-stationary period was computed. Spatial maps of maximum cross-correlations between surface-temperature and air-temperature at (i) 2 m, and (ii) 8 m a.g.l. are shown in Figure V.6. The region of maximum cross-correlation between surface-temperature and air-temperature is elongated in the wind-direction. The upwind correlation region and the scalar footprint function show significant overlap (however, note the footprint obviously only extends upwind while the correlation region extends upwind and downwind). Specifically, the cross-wind spread of the maximum correlation region is similar to that of the footprint function. The maximum correlation coefficient, size of the correlation region, and the footprint increase when the 8-m air-temperature is correlated with the surface-temperature. Similar trends are also observed for the other stationary periods.

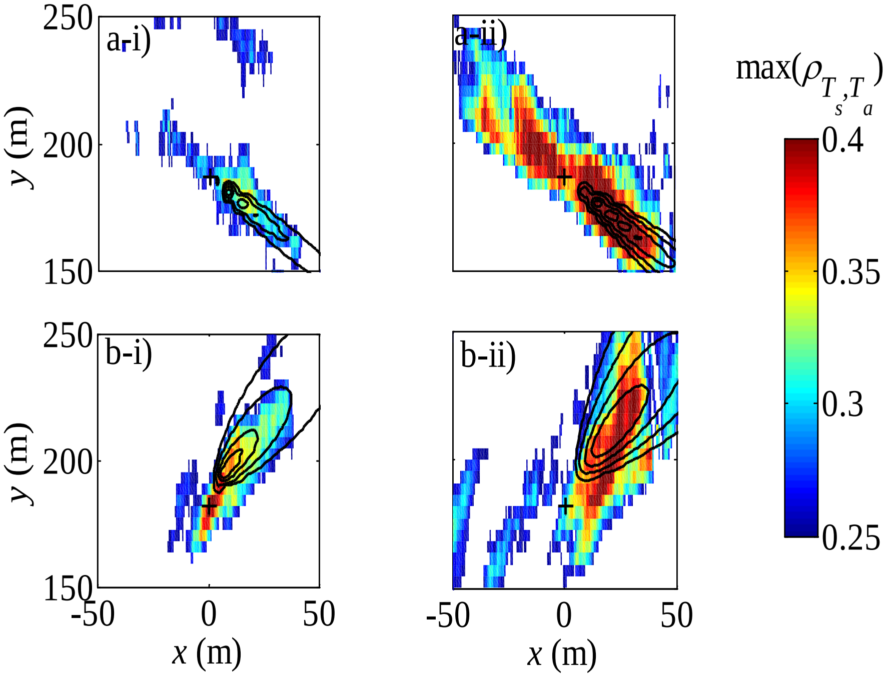

Figure V.6. 30-minute maximum cross-correlation between surface-temperature and air-temperature at (i) 2 m and (ii) 8 m with scalar footprint model (Eq. 3, black contours) for L = (a) −10.2 m, and (b) −19.5 m. White pixels represent surface- and air-temperature correlation less than 0.25 or unreasonable lags (absolute lag greater than 60 s). The black contour lines represent 10, 25, 50 and 75% of the maximum of scalar footprint function. The black '+' sign marks the location of the sonic tower (x_o = 0.4 m and y_o = 185 m).

Along the wind-direction cross-correlations between the air-temperature at 8 m a.g.l. and the lagged surface-temperature (Figure V.6ii) are then plotted in Figure V.7i. Here, positive r indicates the downwind direction and positive lags indicate that the surface is preceding the air and vice versa. The largest cross-correlations for the upwind (downwind) correlation region occur at a positive (negative) lag (shown in Figure V.7i). Thus the upwind surface-temperature is affecting the air-temperature at the measurement location and the air-temperature at the measurement location is affecting the downwind surface-temperature, consistent with Garai and Kleissl (2011). Cross-correlations between *surface-temperatures* along the wind-direction are shown in Figure V.7ii as calculated using

$$\rho_{Ts,Ts}(r, \Delta t\colon x_*, y_*) = \frac{\langle {T_S}'(x_*+r\cos\theta, y_*+r\sin\theta, t+\Delta t){T_S}'(x_*, y_*, t)\rangle}{\sigma_{Ts}^2} \qquad \text{(V.3)},$$

where x_*, y_* and θ are arbitrary coordinates in the image and wind-direction. To reduce the noise of the cross-correlation between surface-temperatures, ensemble averages from 15 different (x_*, y_*) positions were computed. Note the distinction between these cross-correlations versus the spatial correlations $\rho_{xy}(\Delta x, \Delta y, t)$ described in Chapter V.2.2; the former 'tracks' surface-temperature structures by co-varying space (r) and time (Δt), while the latter correlates structures that are not time shifted across space. Therefore, $\rho_{xy}(\Delta x, \Delta y, t)$ represents the typical spatial extent of surface-temperature structures at a given time and $\rho_{Ts,Ts}(r, \Delta t\colon x_*, y_*)$ represents the spatio-temporal region of influence of a given structure. If a structure remained unchanged as it moves across the image, $\rho_{Ts,Ts}(r, \Delta t\colon x_*, y_*)$ would be large.

For the correlations between surface-temperatures, a positive lag indicates that the upwind surface-temperature is preceded by downwind surface-temperature. The cross-correlations between the surface-temperatures in Figure V.7ii are larger compared to the cross-correlations between air-temperature and surface-temperature in Figure V.7i as the latter is calculated between two different variables and heights. Since the spatial extent of the high correlation region between the air-temperature and surface-temperature depends on the air-temperature measurement height, it is not useful to compare quantitatively the spatial extents of the high correlation regions for air-temperature and surface-temperature with that for the surface-temperatures at a given stability. Qualitatively, as the stability of the boundary layer increases, the spatial extent of the high correlation region between air-temperature and surface-temperature; and between surface-temperatures increases. A less unstable boundary layer will contain longer turbulence structures which is manifested in the larger footprints in Figure V.7i. The cross-correlations between air-temperature and surface-temperature; and between surface-temperatures allow tracking the advection speed of the structures responsible for land-atmosphere exchange.

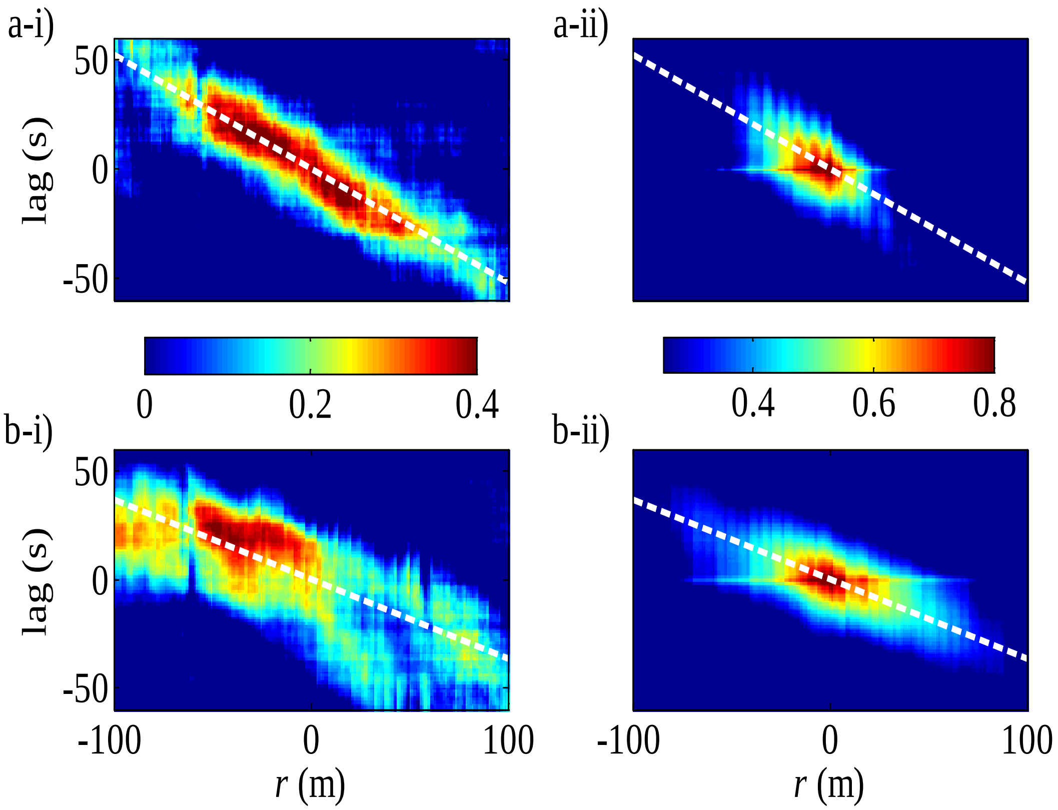

Figure V.7. Left panels: Cross-correlation between air-temperature at 8 m with surface-temperature along the 8-m wind-direction at different lags. Right panels: Cross-correlation amongst surface-temperature along the 8-m wind-direction at different lags. (a) $L = -10.2$ m, and (b) $L = -19.5$ m. The white dashed line represents the slope of the cross-correlation area.

V.2.4 *Advection speed of the surface-temperature structures*

The cross-correlation surfaces between air-temperature and surface-temperature; and between surface-temperatures in Figure V.7 show similar slopes for a given stationary period, which is further evidence for the advective nature of the surface-temperature coherent structures. The slope of the cross-correlation indicates the advection speed u_s of the surface-temperature structures (or rather the turbulent coherent structures that leave an imprint on the surface) along the wind-direction. The estimated advection speeds for all stationary periods are plotted in Figure V.8. The scatter in the plot is mostly due to the uncertainty in estimating the slope; for some wind-directions the high correlation region is discontinuous (as seen in Figure V.6bii, V.7bi) due to surface heterogeneity. The advection speeds are similar to the wind-speed at 8 m a.g.l. with a decreasing trend in less unstable conditions.

Wilczak and Tillman (1980) also reported that the speeds of surface-layer plumes are greater than the wind-speed at 4 m a.g.l. with a small decreasing trend with stability. As the surface-layer becomes less unstable, the strength of buoyant production decreases compared to shear production, resulting in less turbulent mixing. This causes a larger vertical gradient of horizontal wind-speed in the upper part of the surface-layer and also a smaller effective plume height. The advection speed, i.e. the mean wind-speed over the height of the surface-layer plume, should be identical to u_s of the surface-temperature coherent structures. Thus, with increase in the stability of the boundary layer u_s decreases compared to the wind-speed at a sufficiently large altitude (e.g. 8 m a.g.l. in this case). Also as seen in Figure II.5b, except for 25 June the mixed-layer wind-speed is similar to the wind-speed at 8 m a.g.l. Consequently, one can conclude that u_s is similar to the mixed-layer wind-speed. This is consistent with Katul et al. (1998) and Renno et al. (2004), who in the absence of thermal imagery, resorted to more elaborate spectral analysis to suggest that surface-temperature structures are caused by mixed-layer turbulence.

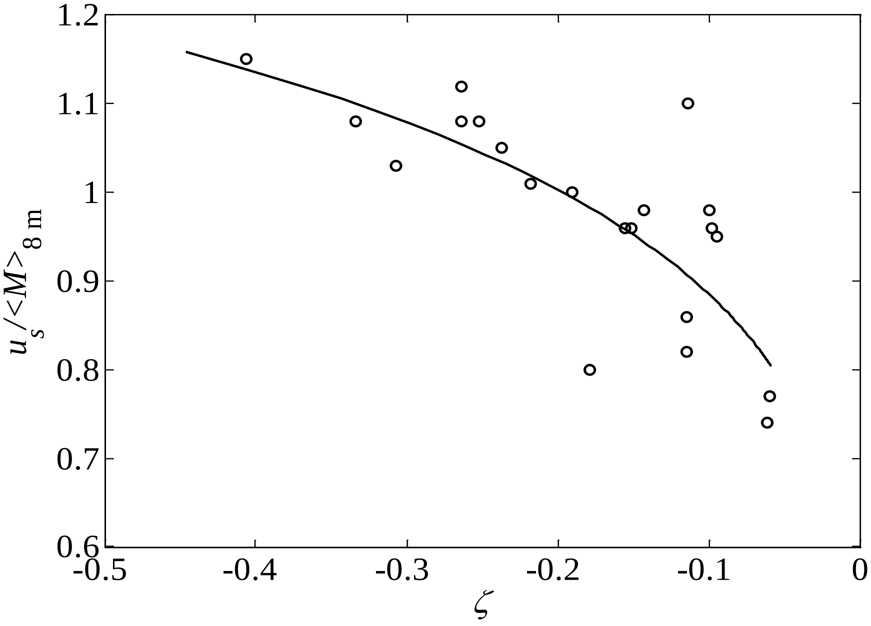

Figure V.8. Advection velocity of the surface-temperature structures (determined from Figure V.7) versus the 8-m wind-speed as a function of ζ. Markers represent the measurements and the solid line represents the fitted equation $u_s/\langle M\rangle_{8\text{ m}} = 1.34(-\zeta)^{0.18}$ with 57.1% coefficient of determination.

V.2.5 *Conditional averaging of ejection events*

To study the coupling between surface-temperature and near surface coherent structures in more detail, conditional averaging was employed. Events are classified as strong ejection events if $w'T_a'{}_{8m} > 0.5\langle w'T_a'\rangle_{8m}$, w' is positive, and the minimum duration of the event is 3 s. Also, if two consecutive events are separated by less than 5 s, they are merged into a single event. The events are then verified by visual inspection of the time series to avoid false identification. These criteria result in 20 to 30 ejection events per stationary period with time scales ranging from 3 s to 45 s. Since the duration of each ejection event is different, time was normalized by the individual ejection time scale such that t = 0 and 1 indicates the start and end of the ejection event at 8 m a.g.l. respectively.

The events cover around 20 to 25% of each 30-min stationary period, but are responsible for 60 to 70% of the sensible heat-flux. The ejection event is initiated by surface heating (Figure V.9i). Since net radiation is nearly constant during the short duration of the event, the increase in ground heat-flux associated with surface heating has to be balanced by decreases in the convective fluxes. Thus before the ejection event, $w'T_a'$ is small. During the ejection event (Figure V.9i) the warm air rises due to buoyancy, forming a surface-layer plume. The majority of the vertical heat-flux occurs at the end of the ejection event (Figure V.9ii) and buoyant production increases compared to shear production (Figure V.9iii). After the ejection event, a downward flow of cold air occurs as a sweep event. The large convective heat-flux during the ejection leads to cooling of the surface and as a result the ground heat-flux decreases until the end of the sweep event. Also, note that though air-temperature shows a ramp-like pattern (air-temperature remains almost constant during the sweep, gradually increases during the sweep to ejection transition, attains maximum at the ejection and drops sharply during the ejection to sweep transition), the change in surface-temperature is smoother (gradual increase and decrease during sweep to ejection and to sweep events). This might be attributed to the higher thermal inertia of the surface compared to the air, so that small scale variations average out over the surface.

Though air-temperature and surface-temperature follow similar trends, there is a time lag; the surface-temperature reaches its maximum before the air-temperature and its minimum after the air-temperature consistent with Garai & Kleissl (2011). Also, from Figure V.9i, it is evident that the plumes are slightly tilted due to wind shear. Since the shear production decreases more rapidly with height than buoyant production, the magnitude of Ri_f increases with height (Figure V.9iii). Also, the magnitude of Ri_f during the ejection event decreases with increasing stability of the boundary layer. Similar results are obtained for the other stationary periods.

Although the magnitude of *G* depends on the thermal properties of the ground, the ground heat-flux normalized by the mean, $G^* = {}^{G}/_{\langle G \rangle}$, is independent of ground thermal properties as the ground conduction model is linear. Figure V.9ii show that the ejection and sweep events cause variations of up to 0.3 times the mean ground heat-flux.

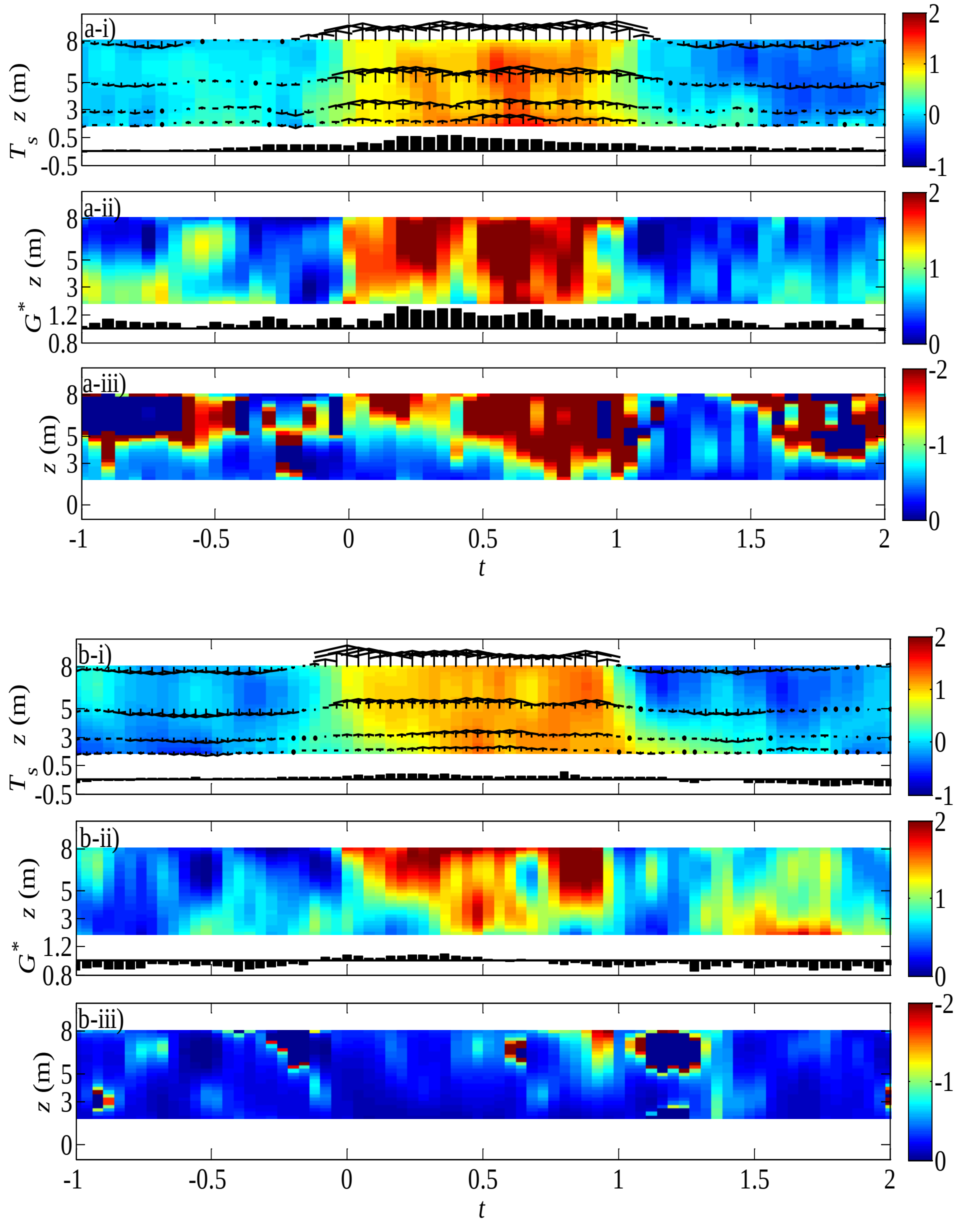

Figure V.9. Conditional average of ejection events occurring for L = (a) −10.2 m, and (b) −19.5 m. (i) air-temperature (colour), and surface-temperature (bars), both normalized by $-T_*^{SL}$. Vertical velocity vectors are overlayed (the largest vectors correspond to 0.4 m s^{-1}). To convert surface-temperature to a time series, Taylor's frozen turbulence hypothesis was applied using the advection speed of surface-temperature structures (Figure V.7). (ii) $w'T_a'$ normalized by $\langle w'T_a' \rangle_{2m}$ (colour) and modelled ground heat-flux normalized by mean ground heat-flux (G^*, bars). (iii) Ri_f. The time axes are normalized such that t = 0 and 1 correspond to the start and the end of the ejection event at 8 m a.g.l., respectively. Note that the surface-temperature is not from the footprint of the air-temperature, but rather the temperature directly below the air-temperature measurements.

V.3 Discussion and conclusion

Coupled land-atmosphere heat transfer was examined using lower surface-layer eddy-covariance measurements and IR surface-temperature imagery for a range of unstable conditions in the CBL. The sequential IR images of surface-temperature show that temperature patterns in the surface grow, combine with each other and move along with the wind. These surface-temperature patterns can be interpreted to be the imprints of turbulent coherent structures on the surface in a CBL (Derksen, 1974; Schols et al. 1985; Paw U et al. 1992; Katul et al. 1998; Balick et al. 2003; Ballard et al. 2004; Renno et al. 2004; Vogt, 2008; Christen and Voogt, 2009, 2010; Christen et al. 2011; Garai and Kleissl, 2011). When the surface-temperature standard deviation is compared with the air-temperature standard deviation, this follows a similar trend with respect to stability and the former is smaller in magnitude than the latter at 8 m a.g.l. The normalized σ_{Ts} gives a similar power-law exponent (0.39) compared to surface-layer similarity theory (Wyngaard et al., 1971); the coefficient of proportionality differs significantly (for our data, 0.36), but it should depend on the surface thermal property (Tiselj et al., 2001; Balick et al., 2003). Different σ_{Ts} over different surfaces (σ_{Ts} over metallic roofs > lawns > roads > building walls) were also reported by Christen et al. (2012) for an urban measurement site.

Cross-correlating surface-temperature and air-temperature, the maximum correlation region is aligned with the wind-direction. The cross-wind span of the correlation region increases with the standard deviation of the wind-direction. The upwind correlation region corresponds well to the scalar footprint formulated from the model by Hsieh et al. (2000). The lag associated with the maximum correlation reveals that the upwind surface-temperature fluctuations affect the air-temperature fluctuations at the measurement tower and the air-temperature fluctuations at the measurement tower affect the downwind surface-temperature fluctuations. This indicates that vertically coherent structures advect cold and warm fluid downwind and these structures leave a temperature footprint on the surface. The correlation between footprint-averaged surface-temperature with air-temperature increases from 2 m to 8 m. All these observations point to the surface-temperature fluctuations being caused by turbulent coherent structures in the atmospheric boundary layer.

The mean streamwise size of the surface-temperature structures (or rather the turbulent coherent structures that leave an imprint on the surface) decreases with ζ. The aspect ratio (*AR*) of the structures increases with both u_* and ζ. Wilczak and Tillman (1980) also reported similar sizes of coherent structures and their advection speed in the CBL by considering the time trace of air-temperature at 4 m a.g.l.. These findings further substantiate that the surface-temperature patterns reflect common properties of turbulent coherent structures in the boundary layer. More unstable flows cause more circular and shorter coherent structures while more neutral flows give rise to longer, streaky patterns, consistent with the observations of Hommema and Adrian (2003) and Li and Bou-Zeid (2011). Katul et al. (2011) related the change in the coherent structures with instability to the Businger-Dyer relationships.

The advection speed of the structures was of the order of the wind-speed at 8 m a.g.l. and it decreased with stability. The mixed-layer wind-speed was almost the same as the wind-speed at 8 m a.g.l.. Similar results were reported by Christen and Voogt (2009, 2010) and Garai and Kleissl (2011). Katul et al. (1998) and Renno et al. (2004) inferred that high frequency surface-temperature fluctuations were caused by mixed-layer turbulence.

The surface-temperature coherent structures are finally interpreted in the context of the surface renewal method. While the Lagrangian concept of the surface renewal method cannot be conclusively demonstrated in the Eulerian measurement framework, the observations give rise to the following interaction between coherent structures and the surface. During the sweep event, a cold air parcel descends and the surface cools due to enhanced temperature differences and heat transfer between surface and air. The cooler surface results in a smaller ground heat-flux during this time (Figure V.9i and ii; $t > 1$ or $-1 < t < -0.5$). As the air parcel remains in contact with the surface it warms gradually, reducing heat transfer between the surface and the air. The ground heat-flux increases during this time. Thus, the surface starts to warm (Figure V.9i and ii; $-0.5 < t < 0$). As the air parcel warms up, it gains buoyancy (Figure V.9iii). With sufficient buoyancy (and possibly assisted by mixed-layer turbulence) the air parcel ascends in an ejection event. During the initial period of the ejection event, the ground heat-flux reaches a maximum (Figure V.9i; $0 < t < 0.5$). As the ejection event continues greater heat transfer occurs between the surface and the air (Figure V.9ii; $0 < t < 0.5$). Afterwards the surface starts to cool and the ground heat-flux starts to decrease (Figure V.9ii; $t > 0.5$).

In Garai and Kleissl (2011), we also analyzed surface-temperature structures during different phases of the surface renewal cycle. In this study, with the larger camera field-of-view and availability of air-temperature at different heights, we have successfully visualized surface renewal events both in the surface-layer and on the surface. However, due to the larger camera field-of-view in this study, a single image contains several surface renewal events at different stages (Figure V.1). Thus the size of the surface-temperature structure for each individual surface renewal event is averaged out when spatial correlation within an image is considered. While it cannot be demonstrated in this study, we expect the temporal evolution of the structure size to be similar, as found in Garai and Kleissl (2011): during the ejection event there will be a large warm surface-temperature structure, during the sweep event there will be a large cold surface-temperature structure, at the transition from ejection to sweep there will be small patches of cold surface-temperature structures, and at the transition from sweep to ejection there will be small patches of warm surface-temperature structures. These surface-temperature structures grow, combine with each other and move along the higher altitude wind. Strong sweep events are followed by ejection events and the heat transfer mechanism repeats itself. We observed that the surface reaches maximum temperature before the air and minimum temperature after the air. The majority of heat transport occurs during the ejection event (about 60 to 70% of the total sensible heat-flux), which also causes ground heat-flux variations (about 30% of the mean ground heat-flux) through the surface energy budget.

These surface-temperature coherent structures with spatial scales of several hundred metres and temperature variations of 0.5 – 1 K, depending on the boundary layer instability, can reduce the accuracy of different remote sensing applications. The turbulence-induced surface-temperature variations should also be accounted for in numerical models, since they produce considerable surface energy budget anomalies.

Acknowledgements: Content of this chapter has been published in Garai A, Pardyjak E, Steeneveld G-J, & Kleissl J, 2013, Surface temperature and surface-layer turbulence in a convective boundary layer. *Boundary-Layer Meteorol.*, **148**, 51-72. The dissertation/thesis author was primary investigator and author of this paper.

Chapter VI

Numerical simulations of surface temperature

VI.1 Introduction

In the atmospheric boundary layer, daytime solar heating causes the ground surface to be warmer than the air, resulting in a convectively unstable flow. The strength of this convective instability depends on the relative magnitude of buoyant production to shear production of turbulence kinetic energy. As the ground becomes warmer, air near the surface becomes more buoyant and the boundary layer becomes more unstable.

Instability favours the development of turbulent coherent structures that promote and are caused by ascending of near surface warm air during ejection events, and descending of cold air during sweep events. The convective boundary layer has a great influence on moisture transport, cloud formation, pollutant transport, and the urban energy balance.

Kaimal & Businger (1970); Wyngaard et al. (1971); Wilczak & Tillman (1980); Wilczak & Businger (1983); and Renno et al. (2004) studied the logarithmic region, known as surface layer in the atmospheric science community, of a convective atmospheric boundary layer over flat terrain. The majority of the turbulent transport was found to be the result of intermittent events of warm rising air, known as surface layer plumes, and weaker downdraft of cold air from the upper part of the boundary layer. Sawtooth or ramp like air temperature patterns were considered to be the manifestation of these turbulent structures (Schols 1984; Schols et al. 1985; and Gao et al. 1989). The surface layer plumes have diameters on the order of the surface layer height, move with their depth-averaged wind speed, and are tilted by wind shear (Wilczak & Tillman 1980).

As the surface layer plumes ascend through the atmosphere, they merge with each other to form thermals in the outer layer of the convective boundary layer, known as the mixed layer in the atmospheric science community. LeMone (1973); Kaimal et al. (1976); Lenschow & Boba Stankov (1986); Young (1988a, b); Cohn et al. (1998); Drobinski et al. (1998); and Lothon et al. (2006) found that the warm thermals and cold downdrafts form roll vortices in the mixed layer, and create intense turbulence mixing that results in constant wind speed, potential temperature and moisture in the outer layer.

These turbulent structures influence the solid-fluid interfacial temperature. The interfacial temperature fluctuations were observed in the laboratory experiments of neutral channel flow by Hetsroni & Rozenblit (1994); Hetsroni et al. (2001); and Gurka et al. (2004), and in unstable atmospheric flows using single point infra-red sensor, and air-borne or tower-mounted infra-red camera over grass, artificial turf, deserts and urban areas by Schols et al. (1985); Derksen (1974); Gao et al. (1989); Katul et al. (1998); Ballard et al. (2004); Renno et al. (2004); Vogt (2008); Christen & Voogt (2009, 2010); Garai & Kleissl (2011, 2013); Christen et al. (2012); and Garai et al. (2013). Time-lapsed animations of spatial fields of interfacial temperature show warm and cold "structures" on the surface that grow, merge with each other and move along with the mean wind (Garai & Kleissl 2013). The observed interfacial temperature fluctuations were attributed to be driven by the turbulent eddies and they are a function of the flow instability and the ground thermal properties (Garai et al. 2013). Some remote sensing applications, e.g. irrigation management, identification of land mines and illegal land-fills etc. often rely on spatial anomalies in a single infra-red image, and the turbulence induced surface temperature fluctuations reduce the effectiveness of the remote sensing technique.

Transient heat conduction models reveal that when two dissimilar materials with different temperatures are attached, the interfacial temperature depends on the thermal inertia ($\sqrt{(k\rho C_p)}$, where ρ, k, C_p are density, thermal conductivity and specific heat of a material, respectively) ratio and the thickness of the materials (Carslaw & Jaeger 1959). Now, for a turbulent flow over a solid wall, heat transport from the surface is essentially driven by diffuson in the conduction sublayer of the turbulent flow. Therefore the key parameters of the solid-fluid coupled heat transport mechanism are expected to be the solid thickness and the thermal inertia ratio of the solid and fluid, termed the thermal activity ratio (Eqn. VI.1)

$$TAR = \frac{\sqrt{(k\rho C_p)_f}}{\sqrt{(k\rho C_p)_s}}, \qquad \text{(VI.1)}$$

where subscripts "f" and "s" stand for fluid and solid respectively. Tiselj et al. (2001) and Balick et al. (2003) found that the solid-fluid combinations with large *TAR* exhibit large interfacial temperature variation. Hunt et al. (2003) observed different types of turbulent structures (plumes, puffs) for different solid thermal properties in their direct numerical simulation of purely convective driven turbulence.

The main objective of the present direct numerical simulations is to study the solid-fluid coupled heat transport mechanism in a convectively unstable environment by varying the strength of convective instability, the *TAR* and the solid thickness. Since direct numerical simulation (DNS) of atmospheric boundary layer is prohibitive due to a friction Reynolds number of 10^7, we considered channel flow of smaller friction Reynolds number with convective instability. The computationally feasible alternative, large eddy simulation, was not considered due to the lack of physical understanding of wall functions for wall bounded flows. Though the simulated friction Reynolds number is much smaller than that of the atmospheric boundary layer, the results will give a better understanding of the solid-fluid coupled heat transport mechanism. To the authors' knowledge, Lida & Kasagi (1997) is the only peer-reviewed paper on convectively unstable channel flow. Besides the solid-fluid coupling mechanism, the present simulations differ from the simulations in Lida & Kasagi (1997) by the magnitude of Grashof number (an order higher for the most unstable case). The remainder of the article is arranged in following manner: § VI.2, VI.3, VI.4, and VI.5 describe the employed numerical methods for solid-fluid coupling, different numerical simulations, analysis of the numerical results, and conclusion, respectively.

VI.2 Numerical technique

The continuity equation, Boussinesq approximated Navier-Stokes equations and heat transport equation for an incompressible fluid; and the transient heat conduction equation for a solid were solved numerically in the fluid and solid domain separately:

$$\frac{\partial u_i}{\partial x_i} = 0, \tag{VI.2a}$$

$$\frac{\partial u_i}{\partial t} + u_j \frac{\partial u_i}{\partial x_j} = -\frac{1}{\rho}\frac{\partial p}{\partial x_i} + \upsilon \frac{\partial^2 u_i}{\partial x_j^2} + g\beta(T - \bar{T})\delta_{i2}, \tag{VI.2b}$$

$$\frac{\partial T}{\partial t} + u_j \frac{\partial T}{\partial x_j} = \alpha_f \frac{\partial^2 T}{\partial x_j^2}, \tag{VI.2c}$$

$$\frac{\partial T_s}{\partial t} = \alpha_s \frac{\partial^2 T_s}{\partial x_i^2}, \tag{VI.2d}$$

where x_i is the coordinate system with i = 1, 2, 3 as streamwise (x), wall normal (y) and spanwise (z) direction, u_i are the streamwise (u), wall normal (v) and spanwise (w) velocity, T is the fluid temperature and T_s is the solid temperature. ρ, υ, β, α_f , α_s and g are the fluid density, kinematic viscosity, volumetric thermal expansion coefficient, thermal diffusivity, the solid thermal diffusivity and the gravitational constant, respectively. We assumed fluid Prandtl number, Pr, to be unity and the solid thermal properties (mainly thermal conductivity) were varied to obtain a desirable thermal activity ratio. The nonlinear advection terms (in the fluid domain) were discretized using the 5th order Wicker and Skamarock scheme (Wicker & Skamarock 2002), the diffusion terms (fluid and solid domain) were discretized using 2nd order central difference, and time (fluid and solid domain) was advanced by a 3rd order low-storage Runge-Kutta scheme (Williamson 1979). Due to large stencil for the 5th order Wicker and Skamarock scheme, a lower order (1st and 3rd) Wicker and Skamarock scheme was used near the wall boundaries (Raasch & Etling 1991).

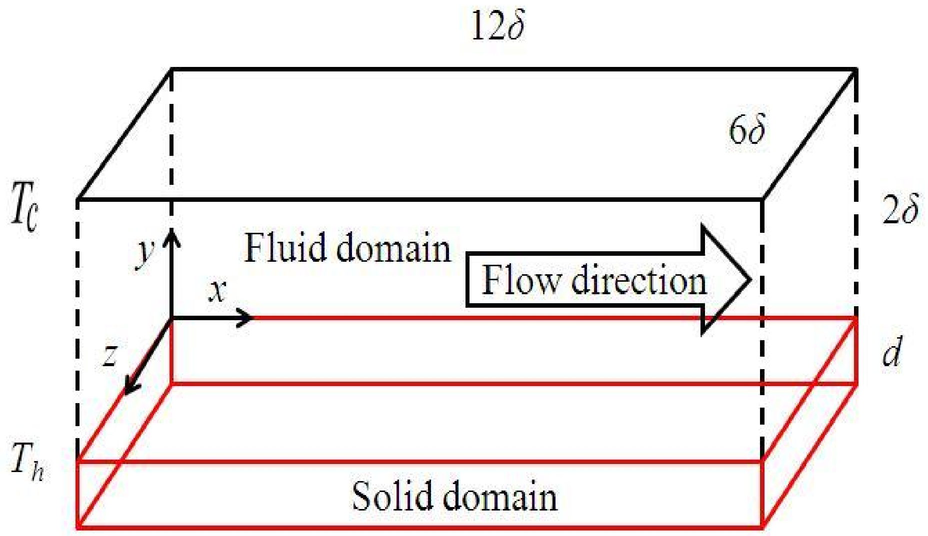

Figure VI.1. The simulated fluid and solid domain.

The fluid domain size was chosen to be 12δ x 2δ x 6δ in the streamwise, wall normal and spanwise direction (Figure VI.1), where δ is the fluid channel half-height, and coupled with a solid domain of thickness d, which is normalized by the heat penetration depth ($\sqrt{\alpha_s \tau}$) derived using the fluid eddy turn-over time τ. To create a simplified representation of the atmospheric boundary layer the solid domain was coupled with the fluid domain only at the bottom fluid boundary. No slip and no penetration boundary conditions were used at the bottom and top boundaries for the fluid domain and periodic boundary conditions were used at the streamwise and spanwise boundaries for both the fluid and solid domains. For convectively unstable flows, the enforced pressure gradient was such that the shear Reynolds number, $Re_\tau = \frac{u_* \delta}{\upsilon}$, would be 180 without any convective instability, and the fluid temperatures at the bottom boundary (T_h) and at the top boundary (T_c) were enforced to deliver a desired Grashof number, $Gr = \frac{g\beta(T_h - T_c)(2\delta)^3}{\upsilon^2}$. The shear Reynolds number increases beyond 180 due to buoyancy effects with increasing Grashof number (Table VI.1). We also simulated one case with a fluid temperature difference between bottom and top boundary and Re_τ = 0, i.e. purely convective turbulence. The eddy turn-over time was defined by $\tau = \frac{2\delta}{u_*}$ and $\frac{2\delta}{v_*}$ for convectively unstable cases and purely convective case respectively, where u_* (= $\sqrt{\frac{\tau_w}{\rho}}$, where τ_w is the wall shear stress) and v_* (= $\sqrt[3]{g\beta q_o(2\delta)}$, where q_o is the wall heat flux) are friction velocity and convective velocity respectively.

The grid spacings are 7.8, 4.75 (all grid spacings are in wall units) along the streamwise and spanwise direction respectively. Along the wall normal direction the grid spacing is 0.18 out to 9 wall units and then uniformly stretched to 5.5 for the highest achievable Re_τ. These grid spacings are also sufficient for the simulated purely convective case, based on Shishkina et al. (2010). This results in 320 x 198 x 288 grid points in the fluid domain. The fluid velocity and temperature were initialized with a constant centre-line velocity ($\approx U_b + 2.4u_*$, where U_b, the bulk velocity, can be estimated from $Re = \frac{U_b 2\delta}{\upsilon} = \left(\frac{Re_\tau}{0.09}\right)^{1/0.88}$ for neutral channel flow, Pope 2000) and bulk temperature ($= \frac{T_h + T_c}{2}$) including random disturbances in the fluid domain except at the boundaries, and after the fluid domain numerical simulation became well developed (about 2 eddy turn-over times), the solid domain temperature was initialized using T_h and q_o as the solid-fluid interface temperature and the wall heat flux ($= -\alpha_f \frac{d\bar{T}}{dy} + \overline{vT'}$ at y = 0, where the overbar indicates averaging over the *xz* cross-section). Then the solid domain bottom temperature was kept fixed at the calculated initial temperature (= $T_h + \frac{(\rho C_p)_f q_0}{k_s} d\sqrt{\alpha_s \tau}$) for the rest of the simulation and the solid domain was discretized using the same grid spacing as the fluid domain resulting in 320 x 288 grid points in the horizontal direction and 13 – 101 in the wall normal direction depending on d for the solid domain. The solid and fluid domain was coupled by equating heat flux $k_s \frac{\partial T_s}{\partial y}_{y=0} = k_f \frac{\partial T_f}{\partial y}_{y=0}$; and temperature $T_{s,y=0} = T_{f,y=0}$ at the interface after each time step. After the start of the solid-fluid coupling, the simulation was run for another 2 eddy turnover times to spin up the solid-fluid coupling. After the wall shear, the wall heat flux and the solid-fluid interfacial temperature converge, the proceeding 6 - 7 eddy turnover times were used to gather data for further analysis.

VI.3 Suite of simulations

Nine simulations were used to study the effect of (i) flow instability by changing *Gr* and Re_τ; and (ii) solid conduction on the fluid flow characteristics by changing the solid thermal properties (*TAR*), and the solid thickness (*d*). The shear Reynolds number, convective Reynolds number ($Re_c = \frac{v_* \delta}{\upsilon}$), friction temperature ($T_* = \frac{q_o}{u_*}$), convective temperature ($T_{**} = \frac{q_o}{v_*}$), Obukhov length ($L = -\frac{u_*^3}{\kappa g \beta q_o}$) and shear Richardson number ($Ri_\tau = -\frac{\kappa g \beta q_o (2\delta)}{u_*^3}$) for different simulated cases are tabulated in Table VI.1. For reference, we also simulated convectively unstable flow without any solid coupling (Case no-c). With increasing convective instability and buoyancy, the fluid flow becomes more turbulent increasing Re_τ. The Obukhov length, a virtual length scale above which buoyant production dominates over shear production of turbulent energy, decreases with the increase in *Gr*, and hence the shear Richardson number ($Ri_\tau = \frac{2\delta}{L}$) also increases. We have used typical near wall scaling laws for normalization of the variables and the normalized variables are denoted by superscript '+' for the convectively unstable case (all Cases except ssRi and llRi) and neutral cases (Case ssRi). Note that as friction Reynolds number is zero for purely convective turbulence (Case llRi), the velocities and temperature were normalized by convective velocity and temperature scales, and the lengths are normalized by thermal boundary layer (defined by Shishkina et al. 2010); and the normalized variables are denoted by superscript '++', unlike other cases.

The numerical fluid-solid coupling procedure does not result any change in the turbulent parameters except the *Gr*. With increasing *TAR* and *d*, the solid-fluid interfacial temperature decreases from the initial temperature (T_h) in Case no-c, resulting in a drop in the *Gr*. In numerical simulations of Rayleigh-Bénard convection (RBC), Verzicco & Sreenivasan (2008) also found that the wall temperature decreased when a constant wall heat flux boundary condition was used instead of constant wall temperature and inferred that scatter in Nusselt numbers amongst different experimental studies of RBC was due to the use of different solid materials. As the present interfacial boundary condition is in-between the two extreme boundary conditions, isothermal and isoflux, we believe that the decrease in interfacial temperature with solid thermal property and thickness is not an artefact of the numerical coupling.

Table VI.1. Turbulence characteristics of the direct numerical simulations. For the case naming 'c' stands for coupling, 's' stands for small, 'ss' stands for very small, 'l' stands for large, and 'll' stands for very large. Note that for case naming of different unstable cases, we have used absolute value of Ri_τ to define large, small etc.

Case	Gr (x10^5)	TAR	d	Re_τ	Re_c	T_* (K)	T_{**} (K)	L (m)	Ri_τ
no-c	325	--	--	193	414	3.46	1.61	−0.25	−4.04
base	320	1	1	192	411	3.40	1.62	−0.25	−4.04
ssTAR	325	0.01	1	192	411	3.40	1.62	−0.25	−4.04
sTAR	324	0.1	1	192	411	3.41	1.62	−0.25	−4.04
sd	324	1	0.1	192	414	3.42	1.61	−0.25	−4.04
ld	315	1	10	192	410	3.36	1.63	−0.25	−4.04
sRi	163	1	1	187	305	1.44	0.88	−0.57	−1.77
ssRi	3	1	1	183	65	0.015	0.04	−54.14	−0.02
llRi	325	1	1	0	450	∞	1.94	0	−∞

VI.4 Results

Since the novelty of our paper not only lies in the solid-fluid coupling, but also the simulation of convectively unstable channel flow, both the effect of the instability and the solid-fluid coupling will be discussed in the following subsections.

VI.4.1 Effect of convective instability

Instantaneous snapshots of temperature (Figure VI.2) show warm and cold regions at the solid-fluid interface. These regions are aligned with and move along the streamwise direction for unstable and neutral cases and lie beneath the warm updrafts and cold downdrafts for all the cases. Updrafts of warm fluid and downdrafts of cold fluid constitute most of the heat transport and their activity increases with the increase of buoyant production. The interfacial temperature patterns and hence the turbulent coherent structures are different for unstable, neutral and purely convective case. While in the unstable cases the strongest turbulent ejection and sweep structures tend to align one after another forming streamwise roll vortices, in the neutral case the interfacial temperature appears similar to the skin friction structure for a neutral channel flow (Kim et al. 1987), and for the purely convective case the interfacial temperature structures tend to be cell like (Verzicco & Sreenivasan 2008). Hetsroni & Rozenblit (1994) observed the similar elongated interfacial temperature structures in an open channel neutral flow experiment with $Re_\tau = 290 - 500$.

The swirling strength criteria (Zhou et al. 1999; Pierce et al. 2013) in Figures VI.2-ii show that strong vortex cores are predominantly in the updraft regions compared to the downdraft regions. Details of these turbulent structures and their implication on the interface temperature will be discussed in the following sections.

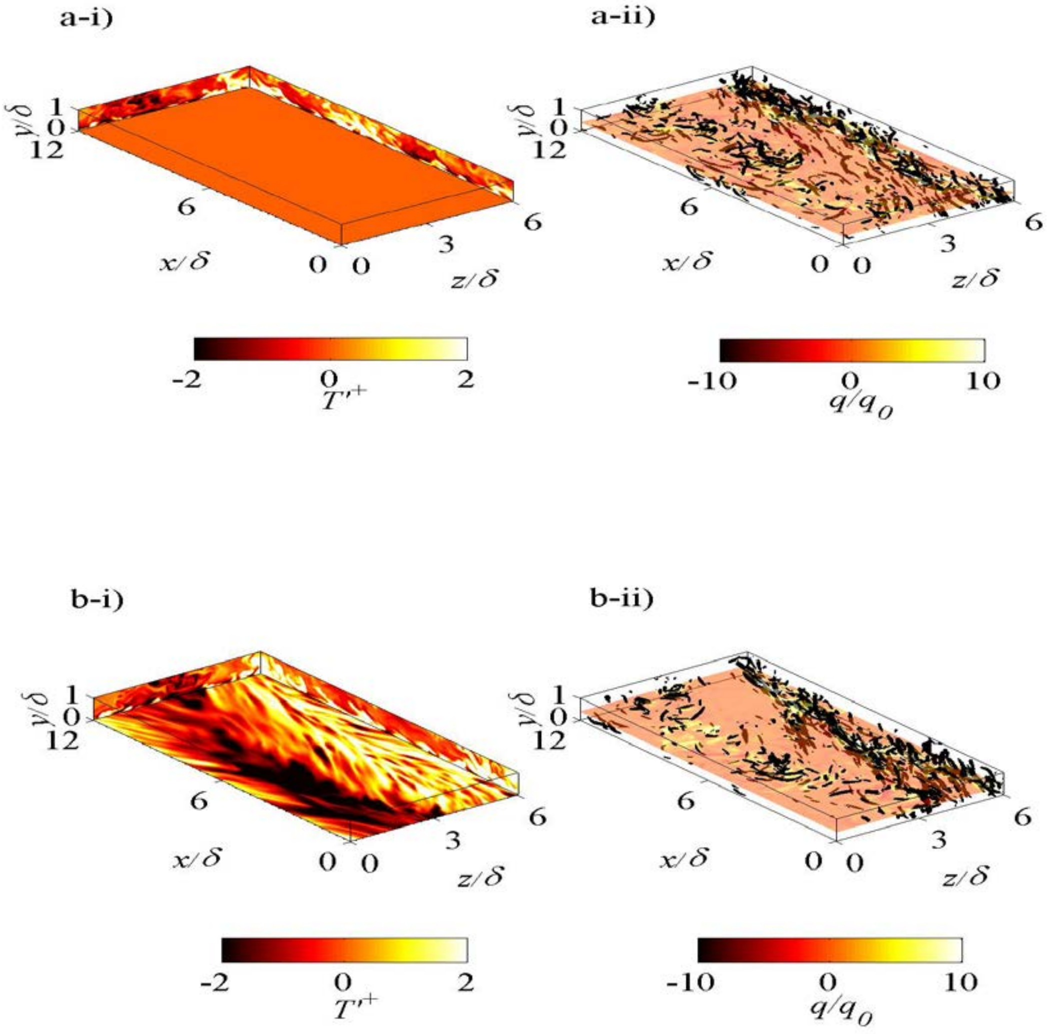

Figure VI.2. Instantaneous snapshots of (i) temperature at the domain boundaries; and (ii) strong vortex cores (identified using isosurfaces of swirling strength) with total heat flux at $y = 0.4\delta$ for (a) Case no-c (no coupling) with constant interfacial temperature; (b) the Case base; (c) Case ssRi and (d) Case llRi. The cut-off value for swirling strength was $3.5 \times 10^{-2} \left(\frac{\partial u}{\partial y}\right)_{y=0}^{-2}$ for Cases no-c, base, and ssRi; and $5.5 \times 10^{-4} \left(\frac{v_*^2}{\upsilon}\right)_{y=0}^{-2}$ for Case llRi.

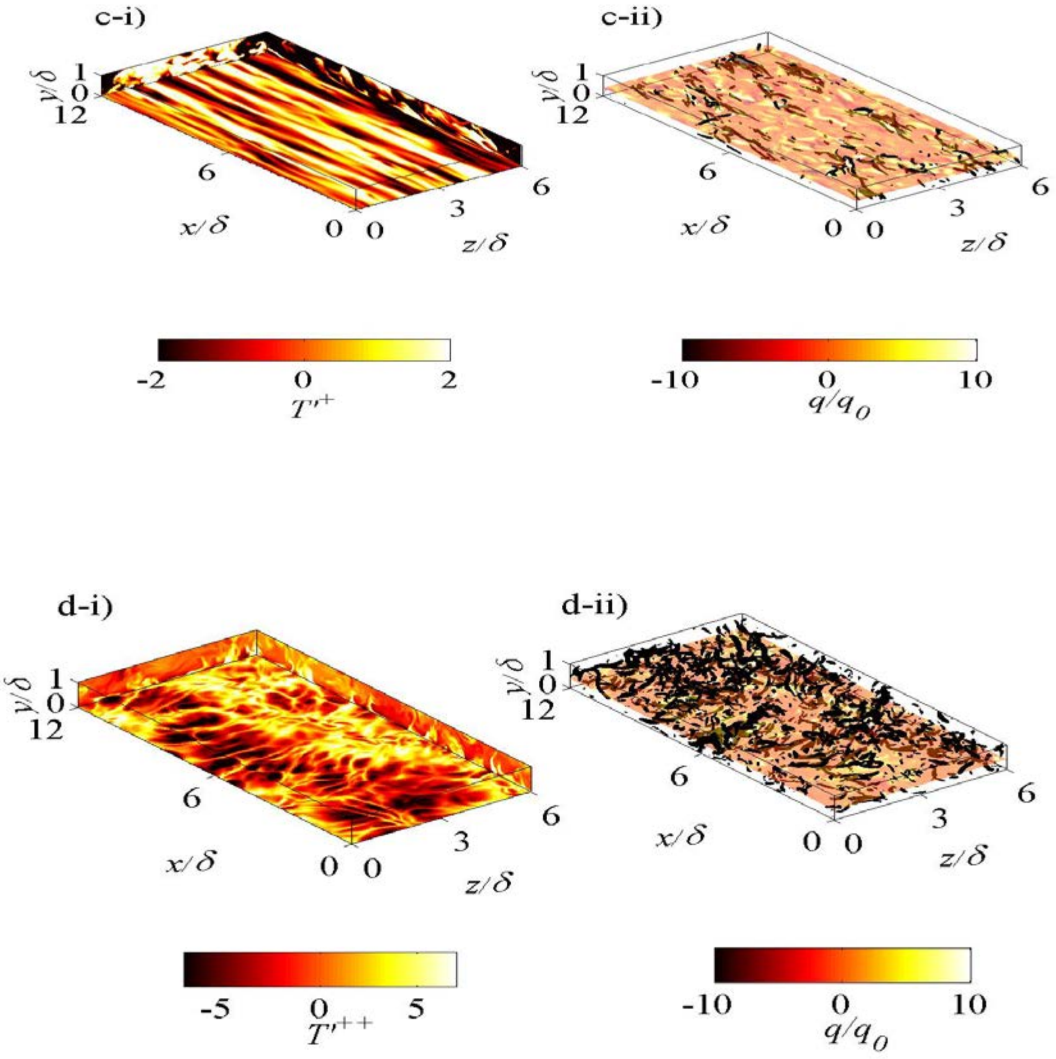

Figure VI.2. Cont.

<u>VI.4.1.a Mean profiles</u>

The mean streamwise velocity increases linearly with wall normal distance in the viscous sublayer region (Figure VI.3a). Similarly the temperature decreases in the conduction sublayer with a slope of *Pr* (Figure VI.3b). Note that the viscous and conduction sublayer thicknesses are similar due to unity *Pr* fluid. In the log law region, convective instability causes enhanced turbulent mixing. Thus the velocity and temperature profiles deviate from the neutral log law formulation, $u^+ = \frac{1}{\kappa}\log y^+ + 5.5$ (Kim et al. 1987), $T^+ = 2.12\log y^+ + \left(\left(3.85Pr^{1/3} - 1.3\right)^2 + 2.12\log Pr\right)$ (Kader 1981), for all the Cases except ssRi and llRi; instead they follow Monin-Obukhov similarity theory, $u^+ = \frac{1}{\kappa}\left(\log y^+ + \psi_m(y/L)\right) + C_m$, $T^+ = \frac{1}{\kappa}\left(\log y^+ + \psi_h(y/L)\right) + C_h$ (Monin & Obukhov 1954), where $\psi_m(y/L)$ and $\psi_h(y/L)$ are the stability correction factor for momentum and heat flux respectively and are given by $\psi_m(y/L) = -2\log\left(\frac{1+X}{2}\right) - \log\left(\frac{1+X^2}{2}\right) + 2\tan^{-1}X - \frac{\pi}{2}$ and $\psi_h(y/L) = -2\log\left(\frac{1+X^2}{2}\right)$, where $X = \left(1 - 16\frac{y}{L}\right)^{1/4}$ (Paulson 1970), derived using Businger-Dyer relationships (Högström 1988) for convectively unstable cases. The mean temperature profile for Case llRi matches the literature of Rayleigh-Bénard convection (Ahlers et al. 2009). Also note that the normalizations differ for purely convection driven turbulence (Case llRi), which has been described in § VI.3. For the neutral case (Case ssRi), the log law profile was recovered for the mean velocity, but neither the log law profile nor Monin-Obukhov similarity describes the mean temperature profile successfully. We speculate that the turbulence, for $Re_\tau = 183$, may not be strong enough to homogenize the temperature in the bulk region. The mean solid temperature increases linearly with distance from the solid-fluid interface and the slope depends on the solid thermal properties and thickness (not shown).

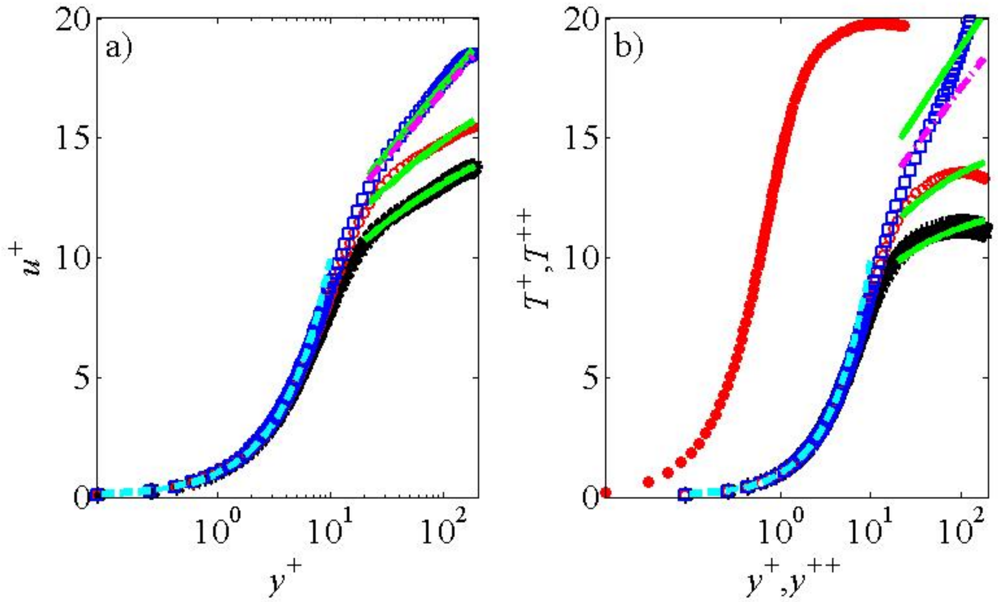

Figure VI.3. Comparison of mean a) streamwise velocity and b) temperature profiles for Cases no-c (black prism); base (black cross); ssTAR (black plus); sTAR (black star); sd (black upper triangle); ld (black lower triangle) (all black symbols fall on top of each other); sRi (red circle); ssRi (blue square); and llRi (filled red circle) with the viscous/conduction sublayer linear profile (cyan broken), (neutral) log law (magenta solid dotted) and (unstable) Monin-Obukhov similarity law (green solid).

Since Monin-Obukhov similarity theory was derived for the log layer of the atmospheric convective boundary layer over surface roughness, we included the constants C_m and C_h for the channel flow cases (Figure VI.3). C_m and C_h were estimated using a least square method for the $y^+ > 20$ and $y < \delta$ regions (Table VI.2) and the values increase to the neutral channel flow value for smaller Richardson number. The accuracy of the estimated values of C_m and C_h suffers from the limited extent of the log layer region at small Re_τ. Jiménez (2012) mentioned that for a substantial log region in a turbulent wall bounded flow Re_τ should be greater than 750.

Table VI.2. Best fit values of the constant offsets in the velocity and temperature profiles for different simulated cases.

Case	C_m (-)	C_h (-)
no-c	4.4	4.5
base	4.4	4.5
ssTAR	4.4	4.5
sTAR	4.4	4.5
sd	4.4	4.5
ld	4.4	4.5
sRi	5.2	5.3
ssRi	5.5	7.0
llRi	-	-

VI.4.1.b Root mean square (r.m.s.) profiles

The r.m.s. profiles of velocity for convectively unstable flows are significantly different from the profiles for the neutral and purely convective channel flow (Figure VI.4a-c). In a neutral channel flow (Case ssRi), u' is the most energetic component, r.m.s. of u' reaches a maximum value of $2.65u_\tau$ at $y^+ = 14$ and in the outer region ($0.2 < y/\delta < 0.85$) all three velocity components decreases linearly consistent with Kim et al. (1987) and Moser et al. (1999). For purely convectively driven turbulence (Case llRi) the horizontal velocities peak at the thermal boundary layer thickness, and the wall normal velocity peaks at the middle of the channel. For the convectively unstable flows (all

Cases except ssRi and llRi) the spanwise velocity component *w'* is the most energetic below y/δ = 0.6. The increase in the spanwise r.m.s. velocity with increase in the convective instability, can be explained by studying the pressure-rate-of-strain tensor (a measure of redistributive effect of fluctuating pressure). Unlike in the neutral case (Case ssRi) where energy is transferred from the streamwise component to both the spanwise and wall normal components, in unstable cases (all Cases except ssRi and llRi) the energy is transferred from both the streamwise and wall normal components to the spanwise component by the fluctuating pressure (not shown). The streamwise r.m.s. velocity peaks where the shear production term in the turbulent kinetic energy budget peaks and both move closer to the solid-fluid interface as the magnitude of Ri_τ increases for unstable cases. On the other hand, the peak location of spanwise r.m.s. velocity does not change with Ri_τ. Similar observations were also made by Lida & Kasagi (1997) for Re_τ = 150 and $Gr \approx 10^6$. With the exception of Case ssRi and llRi, we do not observe a decay of *u'* in the $y/\delta > 0.25$ region for the convectively unstable cases; instead *u'* r.m.s. remain constant (~ $1.6u_\tau$) in this region. The wall normal component *v* increases as y^{+2} in the viscous sublayer, but due to the increase in the buoyant production term of the turbulent kinetic energy budget in the outer region it continues to increase until the channel half-height for the convectively unstable cases (inset of Figure VI.4c). This increase in v in the $y/\delta > 0.25$ region can be successfully described by $\frac{\langle v^2\rangle^{1/2}}{u_*} = 1.9\left(-\frac{y}{L}\right)^{1/3}$ (Wyngaard et al. 1971).

The fluid temperature r.m.s. value peaks in the buffer region, at a similar location where the streamwise r.m.s. velocity peaks (right panel of Figure VI.5). This similarity is due to the unity Pr fluid. In the convectively unstable cases (all Cases except ssRi and llRi), the decay of the fluid temperature r.m.s. between $0.2 < y/\delta < 1$ can also be described by similarity theory: $\frac{\langle T'^2 \rangle^{1/2}}{T_*} = 0.95\left(-\frac{y}{L}\right)^{-1/3}$ (Wyngaard et al. 1971). For the purely convection driven turbulence (Case llRi), the fluid temperature r.m.s. also decreases as $y^{-1/3}$ beyond the thermal boundary layer region. On the other hand, for the neutral case (Case ssRi) the fluid temperature r.m.s. value oscillates around 3 due to non-zero production term of the fluid temperature variance budget equation at the mid channel. Similar result for neutral case was found by several authors, and this behaviour was attributed to the asymmetric mean fluid temperature profile (e.g. Johansson & Wikström 1999; Armenio & Sarkar 2002; Morinishi et al. 2007). De Bruin et al. (1993) also reported that the fluid temperature r.m.s. asymptotes to 3 in large Re_τ atmospheric boundary layers for near neutral cases. Effect of the asymmetric mean fluid temperature on the fluid temperature variance production term gets nullified for convectively unstable and purely convective cases, due to the buoyancy generated enhanced turbulence mixing.

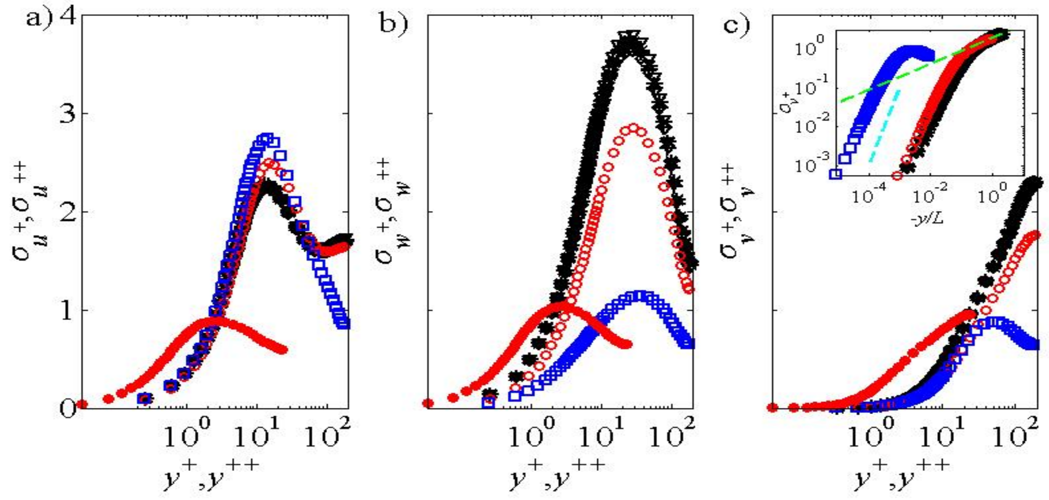

Figure VI.4. Normalized r.m.s. profiles of (a) streamwise, (b) spanwise and (c) wall normal velocity components for Cases no-c (black prism); base (black cross); ssTAR (black plus); sTAR (black star); sd (black upper triangle); ld (black lower triangle); sRi (red circle); ssRi (blue square); and llRi (filled red circle). The inset shows the comparison of wall normal r.m.s. velocity for unstable and neutral cases with the similarity formulation by Wyngaard et al. (1971) (green broken line) and y^{+2} slope line (cyan solid line).

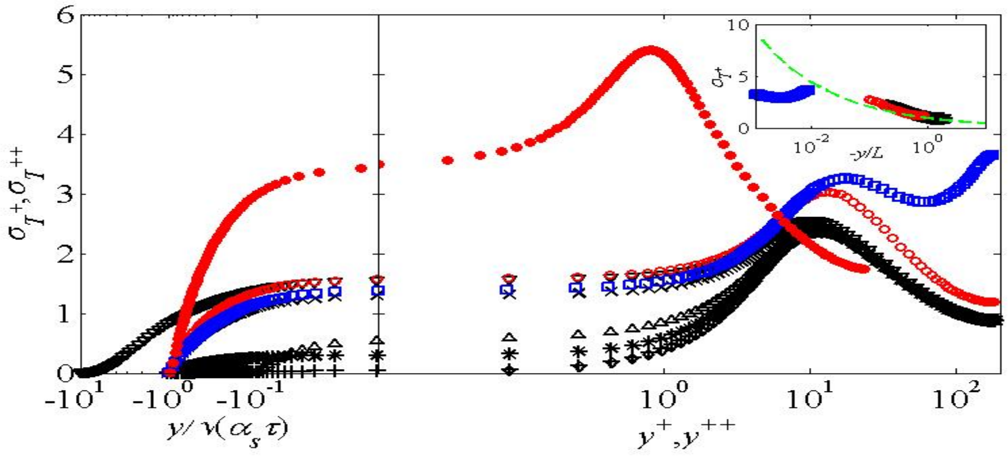

Figure VI.5. The normalized r.m.s. temperature profile of the solid (left panel) and the fluid (right panel) for Cases no-c (black prism), base (black cross), ssTAR (black plus), sTAR (black star), sd (black upper triangle), ld (black lower triangle), sRi (red circle), ssRi (blue square), and llRi (red filled circle). The inset of the figure shows the fluid temperature standard deviation in the $y^+ > 20$ region for unstable and neutral cases with the similarity theory by Wyngaard et al. (1971) (green broken line).

VI.4.1.c Temperature probability density function (p.d.f.)

The probability density function (p.d.f.) of the fluid temperature fluctuations as a function of wall normal distance is now examined to gain insight into the manifestation of coherent structures (Figure VI.6). Conditionally averaged wall normal velocities, *v*, are also shown. The wall normal velocity and the fluid temperature are highly correlated outside the conduction region.

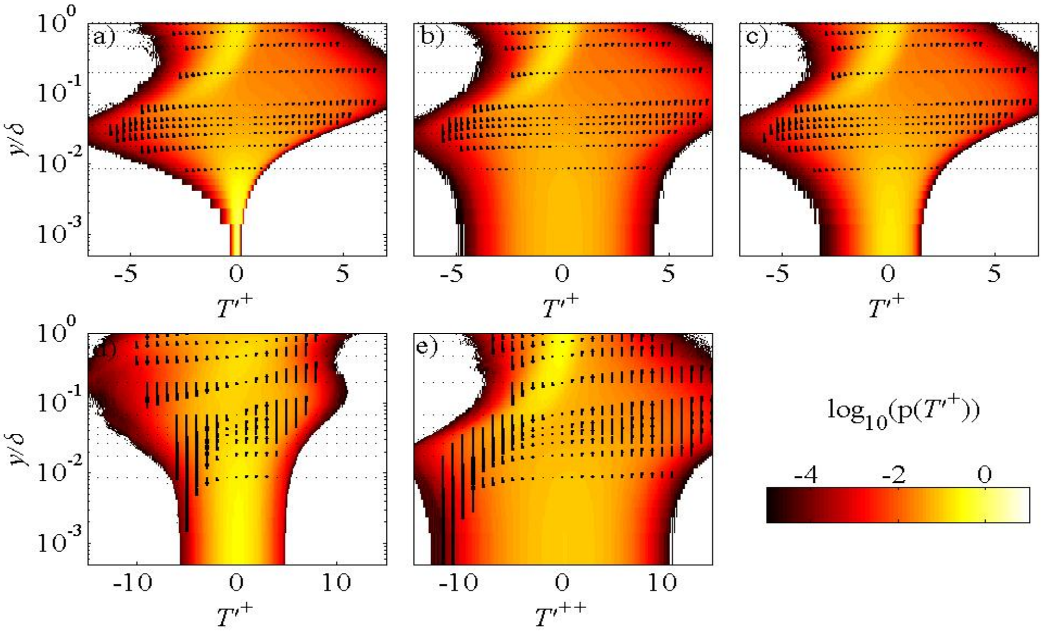

Figure VI.6. Fluid temperature probability density functions versus wall normal distance for Case (a) ssTAR; (b) base; (c) sd; (d) ssRi; and (e) llRi. The black vectors represent conditionally averaged normalized wall normal velocity over the temperature fluctuation bin. The largest magnitude of the velocity vectors is $5u_*$ for Cases ssTAR, base, ld; $1.5u_*$ for Case ssRi; and $2v_*$ for Case llRi.

In the region $y/\delta > 0.1$ but near the warm bottom boundary, the fluid temperature p.d.f.s for convectively unstable and purely convection driven cases show (i) a short tail of negative temperature but with a high probability density, and (ii) a long tail of positive temperature. The high probability density region shifts towards smaller temperatures near

y/δ = 0.1, because of the increase in the temperature difference of cold sweeps versus the warm background. On the positive T' side, as the fluid near the warm bottom wall warms, it will accelerate upwards due to buoyancy; these events manifest in intermittent ejection events. The magnitude of the wall normal velocity associated with sweep events also decreases with the proximity to the wall. The characteristics of the p.d.f. for $y/\delta > 0.1$ remain similar for warm bottom wall and cold top wall, except that near the top the positive temperature fluctuation region assumes the characteristics of the negative temperature fluctuation region near the warm bottom wall (upper half of the channel not shown in Figure VI.6). Since the fluid temperature acts as a passive scalar for the neutral case (Case ssRi in Figure VI.6d), the fluid temperature p.d.f. in the region $y > 0.1\delta$ changes to become more Gaussian (positive and negative tails exhibit similar lengths) irrespective of wall normal distance and its spread increases with the wall normal distance. On the other hand, the fluid temperature p.d.f. changes to a Gaussian behaviour inside the conduction region ($y < 0.1\delta$) for all cases, since there molecular diffusion process are dominant over the turbulent transport processes.

VI.4.1.d Conditional averaging

The above mentioned fluid temperature p.d.f. characteristic can be further explained by studying the turbulent structures using conditional averaging. Different events were identified using thresholds of (i) the total heat flux $(-\alpha_f \frac{\partial T}{\partial y} + vT')$ as q_o, (ii) the absolute value of the wall normal velocity as u_* (for the purely convective case v_* was used instead), and (iii) the horizontal cross-sectional area as $0.028\delta^2$ at a given time. The ejection and sweep events were differentiated by the sign of the wall normal velocity (positive indicates ejection and negative indicates sweep). The search for coherent structures that meet the conditions was repeated for different time instants with a minimum separation of 0.2τ, since the temporal decorrelation length at the mid-channel height was 0.4τ for the Case base.

For $y/\delta < 0.1$, sweeps and ejections could not be identified by the previously mentioned criteria, as the wall normal velocity fluctuations in this region are small (Figure VI.4). With increase in wall normal distance, the number of ejection and sweep events increases and the numbers plateau above 0.2δ. Also the turbulent heat transport mechanism dominates over molecular heat transport above 0.2δ. For unstable cases, the ejection and sweep events cover only about 20 and 15% of the horizontal domain respectively, but together they are responsible for almost all of (about 100%) of the heat transport. The ejection events carry most of the heat transport (about 75%) compared to the sweep events (about 25%) near the bottom wall (at 0.2δ), but the relative contributions of the sweeps increase with wall normal distance. In the mid-channel region both ejection and sweep events contribute equally (about 45%) to heat transport.

The majority of the temperature *variance* occurs due to the ejection events (about 50%) compared to the sweep events (about 10%) at $y = 0.2\delta$. The ejection and sweep contributions increase to about 70% and 25% of temperature variance, respectively, at 0.7δ, and then the ejection contributions decrease, whereas the sweep contributions continue to increase up to channel half-height (δ). Ejection and sweep events contribute equally (about 35% each) to the wall normal velocity variance irrespective of wall normal distance.

On the other hand for Case ssRi, the neutral case, ejection and sweep events cover only about 5% of the horizontal domain and contribute less towards the heat flux, temperature and wall normal velocity variance. For Case llRi, the purely convective case, ejection and sweep events cover about 10% of the horizontal domain, and contribute slightly less toward the heat flux, temperature and wall normal velocity variance, than for the unstable cases. The criteria used to identify turbulent events effect the quantitative statistics provided here, but the qualitative behaviour will remain the same.

Next we studied detailed 3D structures of the ejection and sweep events identified at $y = 0.4\delta$ for Cases base, ssRi, and llRi. The streamwise, spanwise and wall normal distances of the turbulent structures were normalized by their streamwise length at $y = 0.4\delta$, and scaled such that ‘0’ marks the start of an event in the streamwise and spanwise directions and ‘1’ marks the end of an event in the streamwise direction. Events that extended to the boundary of the numerical domain were excluded.

In the unstable flow cases, for sweep events (Figures VI.7i) as the cold fluid parcels approach the solid-fluid interface, they encounter a warmer background causing the temperature difference to increase. This causes a colder region to appear near the bottom surface (Figures VI.7i) and can also be seen in the fluid temperature p.d.f. (Figure VI.6) as a high probability region at negative temperature. The wall-normal velocity of the cold fluid parcel goes to zero as it approaches the wall due to the no penetration boundary condition. This results in a diverging flow pattern in horizontal directions during sweep events near the bottom wall (Figures VI.7ii). On the other hand, ejection events (Figures VI.7iii) are caused by fluid heating near the bottom wall. With sufficient buoyancy, the warm fluid parcel then ascends through the channel and causes a converging flow pattern in the horizontal directions (Figures VI.7iv). The largest ejections and sweeps have streamwise lengths of about 6δ for both Ri_τ = -4.04 and -1.77; and ejections are smaller in the spanwise direction than sweeps.

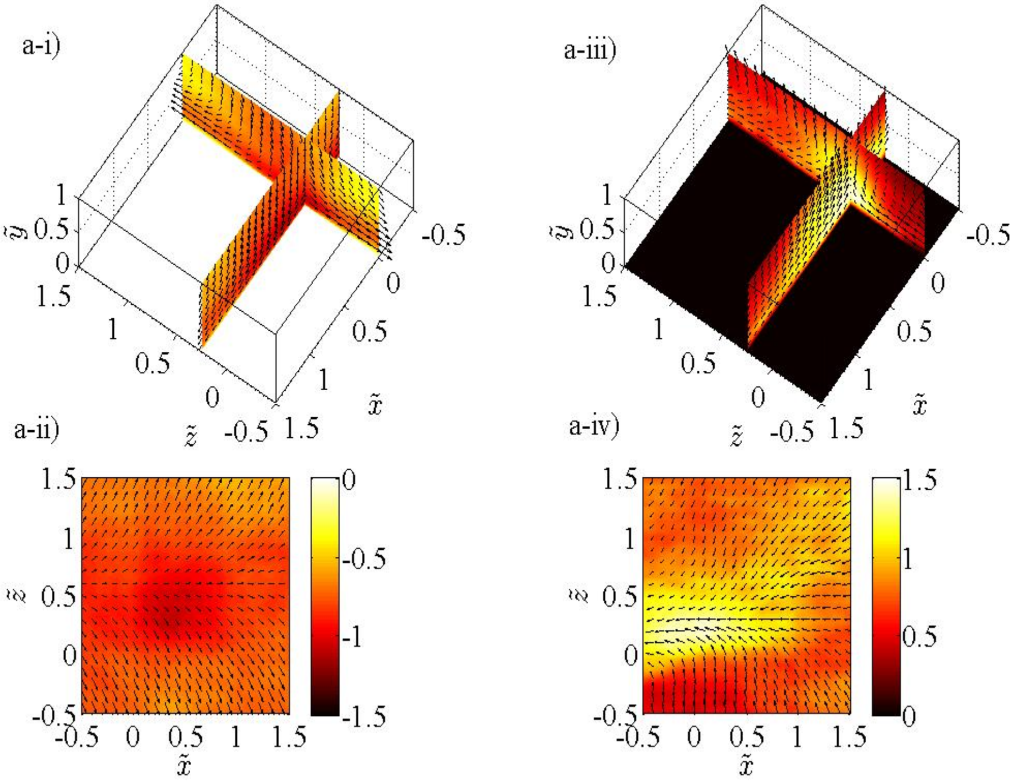

Figure VI.7. 3D structure and $\tilde{x}\tilde{z}$ cross-sectional view at $\tilde{y}$ = 0.25 of the conditionally averaged (i and ii) sweep event and (iii and iv) ejection event for Case (a) no-c; (b) base; (c) ssRi; and (d) llRi. The colorscale represents the conditionally averaged temperature, and the black vectors represent the conditionally averaged in-plain fluid velocity. Curly overbars represent distance normalized by the streamwise lengths of the ejection (sweep) events. Note that the colorscales for the sweep and ejection event are different.

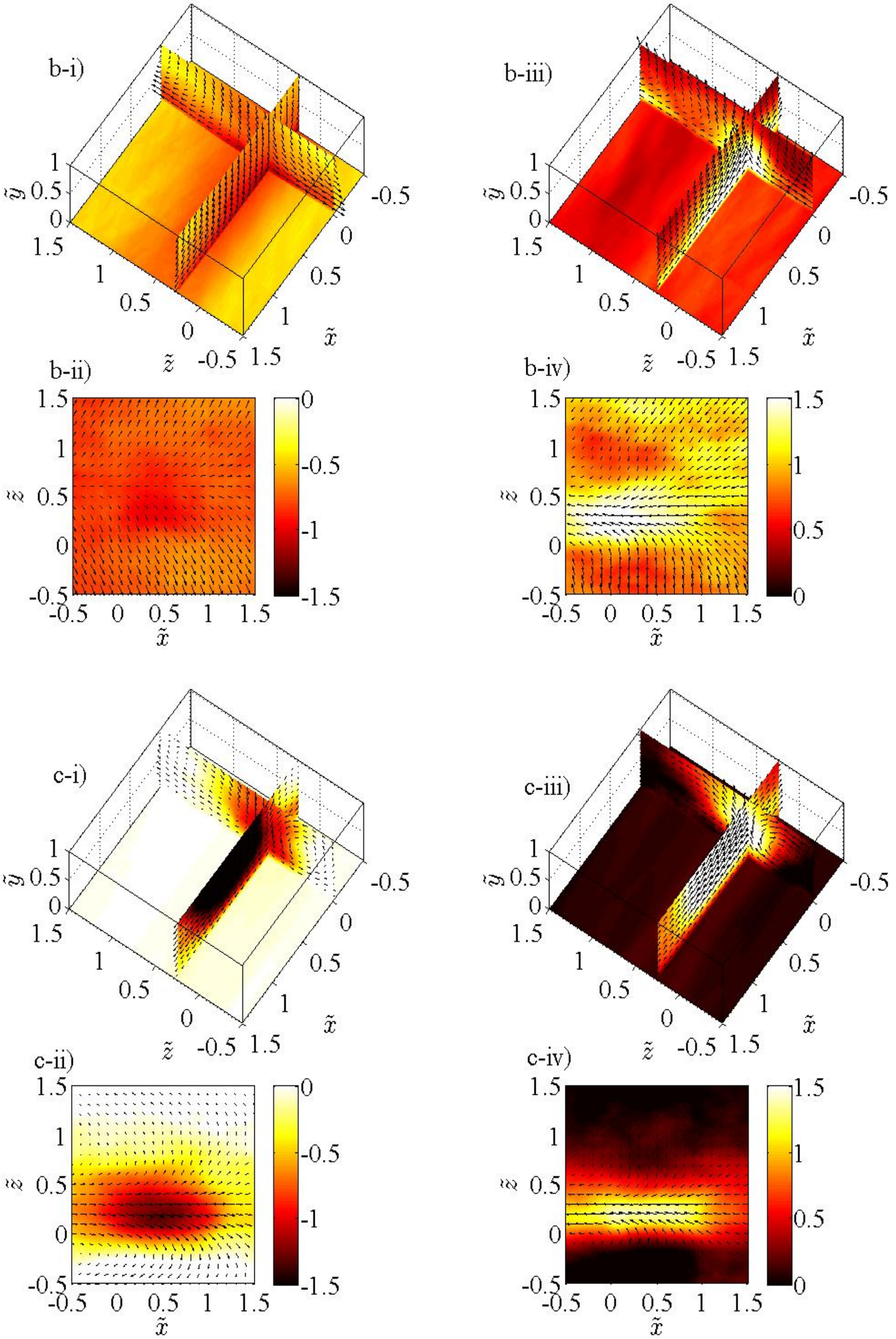

Figure VI.7. Cont.

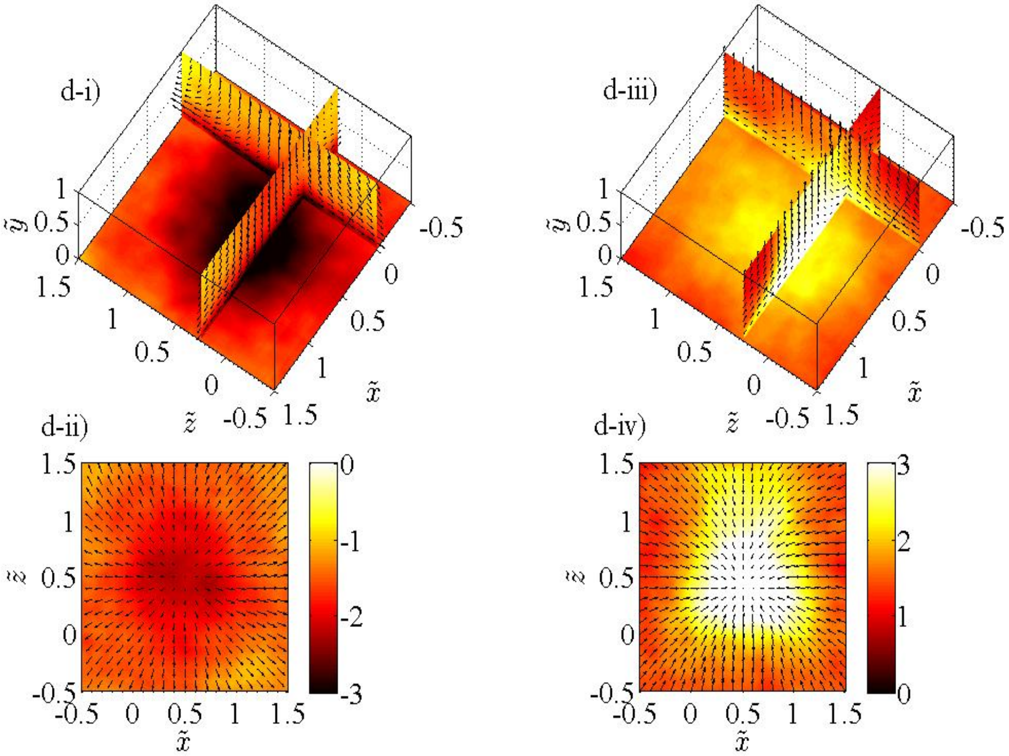

Figure VI.7. Cont.

Fluid temperature acts mostly as passive scalar for the neutral case, Case ssRi, and thus the turbulent characteristics of the ejection and sweep events change (Figure VI.7c), and they look similar to the near wall low and high momentum regions for neutral channel flow cases. The streamwise and spanwise lengths of largest ejection and sweep events are only 1.5δ. The conditionally averaged fluid temperatures vary minimally with wall normal distance, the ejection and sweep events have similar spanwise length, and the horizontal divergence and convergence flow patterns triggered by the ejection and sweep events become weaker.

For Case llRi the absence of shear leads to cellular like structures with maximum streamwise and spanwise lengths of about 2δ. The conditionally averaged fluid temperatures of ejection and sweep events show similar behaviour with wall-normal distance compared to the unstable cases. The horizontal convergence and divergence flow patterns in case of purely convective flow is the strongest amongst the studied cases.

VI.4.1.e 3D spatial temperature cross-correlation

The typical size of the turbulent structures at a given instant was then studied by considering cross-correlation of the fluid temperatures at different wall normal distances with respect to the fluid temperature at a wall normal distance of 0.4δ (Figure VI.8). For the iso-surface a correlation coefficient of e^{-1} was chosen. The structure size depends on this value, but qualitative features are not affected.

The 3D structures of temperature correlation for the unstable cases have some distinct characteristics: (a) In the outer region their spanwise extent is smaller than their streamwise extent and they have a longer tail in the upstream direction, (b) In the viscous/conduction sublayer, the upstream and downstream spatial extents are similar, and (c) Shear near the wall tilts the temperature correlation structures in the flow direction. Strong horizontal convergence and divergence flow patterns are responsible for the increase in the spatial extent of the high correlation region near the surface.

For the neutral case (Case ssRi), the influence of buoyant forcing decreases and temperature behaves more like a passive scalar. Thus the wall normal velocity is less effective in transporting fluid temperature fluctuations compared to the convectively unstable cases. This results in a smaller high correlation region in all three directions.

For the purely convective case (Case llRi), the horizontal extent of the high correlation region is smaller while its wall normal extent is comparable to the unstable cases. In the high correlation region the signature of convergence and divergence flow pattern in horizontal cross sections near the wall is also present in purely convective case, but with a smaller wall normal extent.

The tilt of the high correlation region depends on both the shear and buoyancy forcing. For the neutral case, the correlation region near the surface is tilted by 45^0 since the near wall turbulent structures are driven by the wall shear. For the purely convective case, the high correlation region is normal to the wall, as buoyancy causes enhanced vertical mixing. For unstable cases the tilt is in-between these two extreme, depending on the relative strength of buoyancy and shear: in specific tilt angles of 57^0, and 50^0 for $Ri_\tau = -4.04, -1.77$ are observed. In the bulk region away from the wall the turbulent structures tend to be more normal to the wall since buoyancy increases while wall shear decreases in the bulk region.

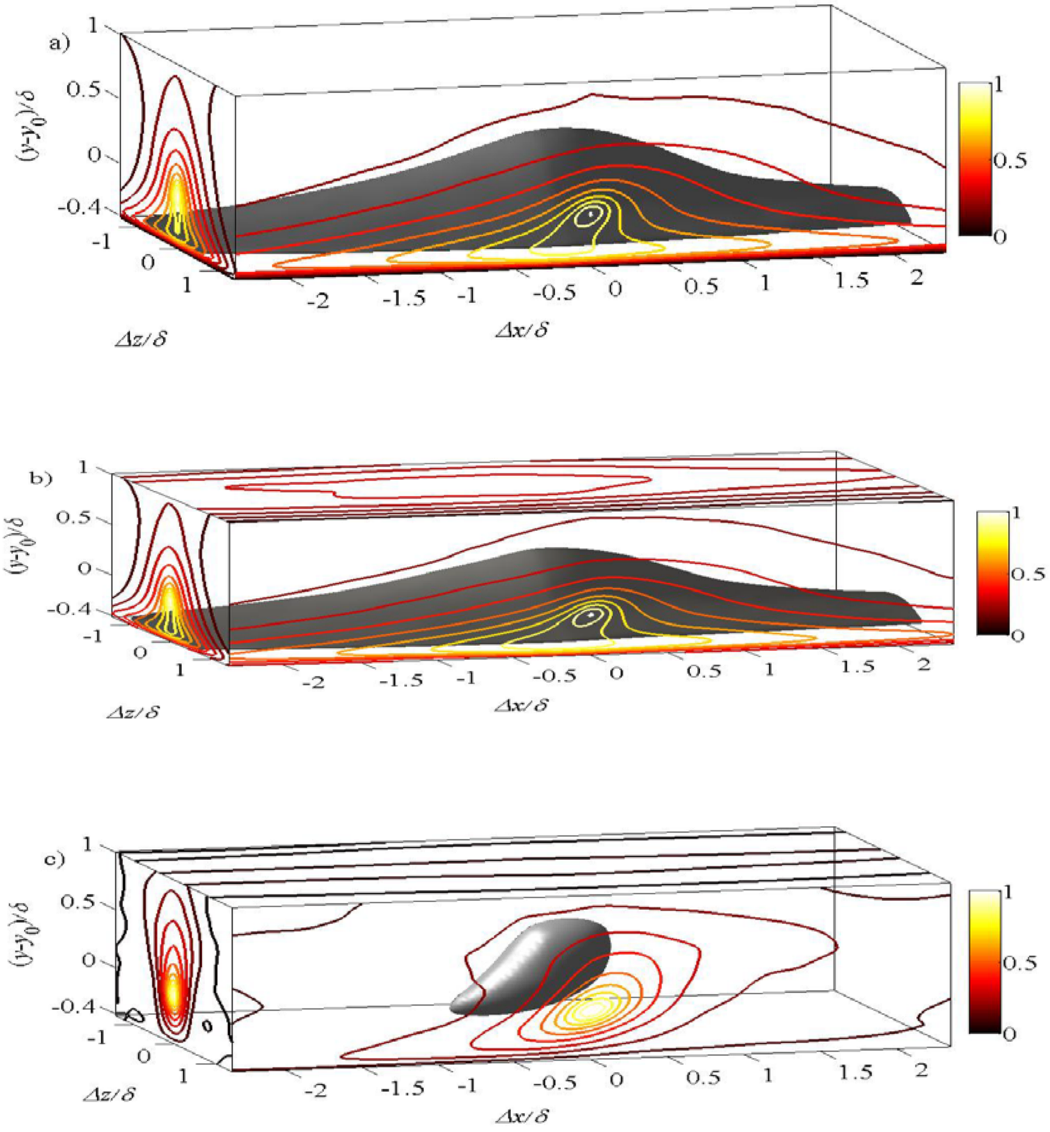

Figure VI.8. Maximum temperature cross-correlation at different wall normal distances with the fluid temperature at $y_0 = 0.4\delta$ wall normal distance from the solid-fluid interface for Case (a) no-c; (b) base; (c) ssRi; and (d) llRi. The black iso-surface shows the 3D structure of cross-correlation = e^{-1}. The contours in the *x*-*y*, *y*-*z* and *x*-*z* plains show cross-correlations at $\Delta z = 0$, $\Delta x = 0$ and $\Delta y = -0.4\delta$, respectively and are displaced for visual clarity. The negative Δx denotes the upstream region and vice-versa. There is no contour line on the top surface of (a), as the interfacial temperature fluctuation is zero for Case no-c.

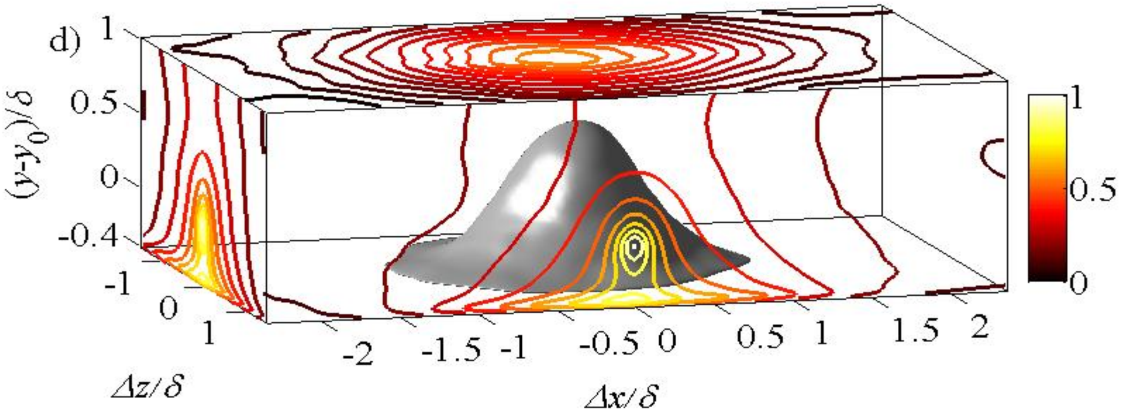

Figure VI.8. Cont.

VI.4.2 Effect of solid-fluid coupling

The solid thermal properties and thickness do not influence the mean fluid velocity (Figure VI.3a) and fluid temperature (Figure VI.3b), except for a small change in the interfacial mean temperature (described in § VI.3); and turbulent velocity fluctuations (Figure VI.4). They only affect the fluid temperature fluctuations in the $y^+ < 20$ region (Figure VI.5) and interfacial temperature structures (Figure VI.2). The normalized interfacial temperature varies spatially by about ±14 for the Case base (Figure VI.2b) and by ±0.1 for Case ssTAR (Figure VI.2c).

Increase in the interfacial temperature and conduction sublayer region fluid temperature variances with *TAR* were also observed by Tiselj et al. (2001). As the solid thermal inertia ($\sqrt{(k\rho C_p)_s}$) increases, it will homogenize the interfacial temperature structures through conduction and internal heat storage. Thus, the solid-fluid coupled heat transport mechanism behaves as isothermal with high surface heat flux variation for $TAR \rightarrow 0$; and as isoflux with high surface temperature variation for $TAR \rightarrow \infty$ (Table VI.3). With increasing *TAR*, larger turbulent structures more effectively imprint on the fluid-solid interface. “Small” scale fluctuations fail to imprint on the surface, but the definition of “small” depends on the *TAR* as the thermal inertia acts like a physical filter.

Table VI.3. The solid-fluid interfacial temperature and heat flux variances as a function of solid thermal properties, thickness and flow instability. For Case llRi, the interfacial temperature r.m.s. is normalized by convective temperature scale.

Case	$\boldsymbol{\sigma_{T^+{}_{y=0}}}$ (-)	$\boldsymbol{\sigma_{q_o}/q_o}$ (-)
no-c	0	0.39
ssTAR	0.03	0.39
sTAR	0.30	0.36
base	1.30	0.20
sd	0.56	0.29
ld	1.54	0.20
sRi	1.58	0.19
ssRi	1.39	0.22
llRi	3.46	0.23

Besides *TAR*, the solid thickness also influences the spectral decay of fluid temperature fluctuations in the conduction sublayer. The isothermal boundary condition imposes zero temperature fluctuation at the solid bottom boundary and thus the solid thickness influences the interfacial heat transport process. This mechanism is related to the heat penetration depth of the turbulent eddy footprints. With a thinner solid (d = 0.1), the "larger" turbulent temperature fluctuations cannot "penetrate" the solid, because they are damped by the bottom boundary of the solid. On the other hand, for a thicker solid (d >> 1) the solid-fluid coupled heat transport mechanism becomes independent of the bottom boundary of the solid. This behaviour for thin solids will change if one assumes an isoflux boundary condition at the solid bottom boundary. Applying an isoflux boundary condition and no buoyancy effects, Tiselj et al. (2001) found that for thin solids interfacial temperature fluctuations increase. For a thick solid (d >> 1), however, the isothermal or isoflux boundary condition will not matter, as the turbulent eddy heat penetration depth will be sufficiently smaller than the solid thickness.

Hence the fluid temperature p.d.f. in the conduction sublayer (Figure VI.6a, b, c) changes with the solid-fluid coupling process. Larger *TAR* and d increase the spread of the temperature p.d.f. and decrease the thermal diffusion and dissipation terms in the temperature variance budget equation. As previously described the solid-fluid coupling only influences the fluid temperature in the conduction sublayer through the thermal diffusion process, while the nature of turbulent coherent structures (Figures VI.7) remain unaltered. *TAR* and d only influence the imprint process of the turbulent structures on the solid-fluid interface (Figure VI.7a and b) resulting change in the cross-correlation between interfacial temperature and fluid temperature (Figure VI.8a and b). The decay of the temperature cross-correlation in the wall normal direction depends largely on the *TAR* and solid thickness. Larger *TAR* causes the correlation to remain larger near the interface, as the fluid temperature imprints on the surface more effectively. The maximum cross-correlation between the temperatures at the solid-fluid interface with $y = 0.4\delta$ decreases from 0.34 to 0.08 to 0.01 as *TAR* decreases from 1 to 0.1 to 0.01. The solid thickness has a similar effect on the correlation decay due to its correlation with heat penetration depth. With increasing solid thickness from 0.1 to 1 to 10, the maximum cross-correlation between the solid-fluid interfacial temperature with the temperature at $y = 0.4\delta$ increases from 0.11 to 0.34 to 0.46.

VI.5 Conclusions

We expanded on work by Tiselj et al. (2001) on the effect of solid conduction on the heat transport mechanism in a neutral channel flow and work by Lida & Kasagi (1997) on the effect of instability on heat transport in a channel flow. In the present study we have included both the effects of convective instability and solid conduction on the heat transport mechanism to emulate solid-fluid interfacial temperature variations in the atmospheric boundary layer.

Different strengths of instability result in different coherent structures. Low and high momentum flow regions are observed in neutral channel flow. In a purely convective flow, plumes and downdrafts are the major flow features. Stronger ejection and sweep events caused by the plumes and downdrafts show converging and diverging flow patterns in a horizontal cross-section. The convergence and divergence of horizontal flow is much stronger in the purely convective flow compared to the neutral flow. The turbulent structures are long and streaky in a neutral channel flow, compared to cellular like structures in a purely convective flow. In between these two extremes for convectively unstable flow, both buoyancy and shear are important and the plumes (downdrafts) tend to align one after another along the streamwise direction, and cause streamwise roll vortex in the bulk region of the channel flow.

Despite the differences in the Re_τ and Ri_τ between the simulations and atmospheric observations, mean and r.m.s. profiles of velocity and temperature for convective atmospheric boundary layer are recovered. In a convective atmospheric boundary layer, the fluid temperature timeseries show ramp or sawtooth like pattern, consisting of (i) constant temperature during the sweep event, (ii) slow increase in the transition from sweep to ejection, and (iii) a sharp decrease during the ejection event (e.g. Taylor 1958; Kaimal & Businger 1970; Paw U et al. 1995 etc.). The mechanism behind the temperature ramp pattern can be further explained by the surface renewal method (Corino & Brodkey 1969; Brutsaert 1975; Paw U et al. 1995). In a convectively unstable environment as cold fluid descends during a sweep event, the temperature difference compared to the warmer background increases, and its downward velocity also decreases due to the close proximity of the wall. As the fluid parcel remains near the warm wall, heat transfer from the wall to the fluid initially peaks, but then decreases due to heating of the fluid; eventually this leads to warming of the wall. With sufficient buoyancy the warm fluid ascends in an ejection, resulting in large heat transport from the wall to the fluid and decreasing wall temperature. Thus the interface appears to be warm during the ejection, and cold during the sweep. Similar to the atmospheric observation (Garai et al.

2013; Garai & Kleissl 2013) warm and cold structures at the solid-fluid interface are observed in the current DNS.

For the present DNS study, coupling the solid conduction to the fluid affects only the fluid temperature in the viscous or conduction sublayer of a unity *Pr* fluid. The fluid temperature fluctuations influence the interfacial temperature more effectively for the smaller thermal inertia solids (larger *TAR*) with larger thickness. The heat transport mechanism behaves as isothermal with high surface heat flux variation for $TAR \rightarrow 0$, and as isoflux with high interfacial temperature variation for $TAR \rightarrow \infty$ by altering the thermal diffusion and thermal dissipation in the conduction sublayer, consistent with the findings in Tiselj et al. (2001). Since only the larger scales imprint on the surface, the influence of the solid-fluid coupling may be stronger in flows with larger shear Reynolds and Richardson numbers. In the current simulations, the increase in the fluid temperature fluctuations in the conduction layer, depending on *TAR* and *d*, does not influence the turbulent structures, as the buoyant production vanishes in this region. Thus the fluid temperature p.d.f. becomes Gaussian in the conduction sublayer, whereas in the outer layer the distribution is positively skewed with a short negative tail, a long positive tail and a mode in the negative tail near the warm wall.

Though solid thermal properties and thickness do not influence turbulent structures, at least for present DNSs, they influence the solid-fluid interfacial temperatures. The accurate estimation of solid-fluid interfacial temperature is necessary in many environmental and engineering applications, e.g. irrigation management, Nusselt number estimation etc. Accurate prediction of the interfacial temperature variation in an unstable atmospheric boundary layer is important, as it affects the accuracy of remote sensing techniques and wall functions in numerical simulations.

Acknowledgements: Content of this chapter is under consideration for publication in Garai A, Kleissl J & Sarkar S, 2013, Heat transfer in a convectively unstable turbulent channel flow with solid conduction. *J. Fluid Mech*. The dissertation author was primary investigator and author of this paper.

Chapter VII

Summary

In the present dissertation, the influence of turbulent coherent structures on the surface temperature in a convective atmospheric boundary layer was studied experimentally; and in a low Reynolds number flow was studied numerically using direct numerical simulation. The major findings of the research are summarized here.

Atmospheric observations of the surface temperature reveal that warm and cold structures grow and merge with each other. These surface temperature structures are caused by turbulent coherent structures and can be explained by the surface renewal method (Chapter III). As cold air approaches the ground during a sweep event, a large amount of heat will be transferred from the ground to the air, causing a large cold structure on the surface. As the cold air parcel remains near the surface, its temperature increases. This causes small hot patches to appear on the surface. As the air and ground heat up, the warm air will ascend from the surface due to buoyancy causing an ejection event. The majority of the heat and momentum transport occurs during the ejection event that leads to surface layer plumes in the atmospheric surface layer. As the surface layer plumes ascend through the atmosphere, they merge with each other to form thermals in the mixed layer. After the ejection event, the surrounding cold air approaches the ground, and the cycle repeats. The descending of cold air is known as downdraft. Thermal and downdraft together constitute roll vortices in the mixed layer.

The influence of the different turbulent structures (surface layer plumes, thermals, downdrafts, roll vortices) of atmospheric boundary layer with different scales on the surface temperature was then studied (Chapter IV). Coherent structures from the lower surface layer, upper surface layer, mixed layer imprint on the surface temperature and the ground heat flux. Depending on the ground thermal properties, there exists a cutoff scale, below which turbulent structure cannot influence surface temperature. In the atmospheric observations, micro plumes very close to the surface did not leave surface temperature footprints. Although the air temperature trace in the surface layer shows a ramp like pattern, the surface temperature trace shows smooth increases and decreases. The decrease air temperature during the ejection to sweep transition becomes stronger with the height. The turbulent heat flux and the ground heat flux show similar characteristic variations due to the sweep and ejection events.

The focus of Chapter V was to obtain statistics of the surface temperature for different instability of the atmospheric boundary layer. Similar to the r.m.s. air temperature, the r.m.s. surface temperature also follows the –1/3 power law with boundary layer instability z/L. The high correlation region between air and surface temperatures extends in both the upwind and downwind directions from the air turbulent measurement tower; such that the upwind surface temperature influences the air temperature and the air temperature influences the downwind surface temperature. The upwind high correlation region agrees with the scalar footprint function from Hsieh et al. (2000), especially for the cross-wind spread which was modeled assuming a Gaussian profile. The spatial correlation region of the surface temperature is aligned with the mean wind direction; and its streamwise correlation length decreases with increasing boundary layer instability. This is a manifestation of the streamwise long streaky and cellular turbulent structures for the neutral and purely convective boundary layer respectively. The surface temperature "advection speed" - obtained from the slope of the cross-correlations - is similar to the higher level wind speed with a small decreasing trend as boundary layer instability decreases. Wilczak & Tillman (1980) observed similar advection speeds of turbulent coherent structures in the convective atmospheric boundary layer.

While the present study provides a comprehensive dataset and analysis of different aspects of surface temperature fluctuations (e.g. physical explanation of surface temperature structures; effect of different turbulent structures on the surface temperature;

effect of boundary layer instability on the surface temperature) room for future experimental work exists as follows:

a) For the present study, 1 Hz surface temperature data from smaller and larger camera field-of-views from the BLLAST experiment reveal similar spectra and probability density function of the surface temperature. The lack of increase energy in smaller scales for the small field-of-view was attributed to the fact that the large thermal inertia of the ground inhibits small scale turbulence from imprinting on the surface temperature. To test this hypothesis, experiments should be conducted with infra-red cameras at high temporal and spatial resolution.

b) Time-lapsed animation of surface temperatures reveal that the warm and cold structures on the surface move along the mean wind, grow and merge with each other. Thus it should be possible to infer some sort of turbulent velocity field by performing image velocimetry. Present 1 Hz data is inadequate for this exercise. Successful thermal image velocimetry was performed using higher frequency infra-red images by Inagaki et al. (2013) over a building wall and a turf field in a convective atmospheric boundary layer; and by Hetsroni et al. (2001) in a laboratory experiment.

c) In the present study, the largest camera field-of-view was about 200 x 275 m, which is still smaller than the mixed layer structure of atmospheric boundary layer. Thus a larger camera field-of-view over a homogeneous surface is desirable for future studies, which would likely require an airborne sensing system.

d) To confirm the effects of surface thermal properties on the surface temperature, experiments should be performed over different surfaces. Different surface temperature r.m.s. values (metallic roof > lawns > road > building walls) were reported by Christen et al. (2012) for an urban measurement site.

Next interfacial temperature structures in a neutral, purely convective and convectively unstable channel flow were studied with different thermal properties of the solid using direct numerical simulations. Despite the large difference in the friction Reynolds number between the atmospheric observations and the numerical simulations; the results gave a better understanding of the solid-fluid coupled heat transport mechanism. Turbulent coherent structures are strong functions of the flow convective instability. For neutral channel flow long streaky low and high momentum structures dominate, whereas for purely convective flow cellular structures are the most dominant one. For convective unstable flow, plumes (downdrafts) tend to align one after another along the streamwise direction, which result in the formation of roll vortices in the bulk region. Hence the surface temperature structures also represent a pattern of roll vortices. Businger-Dyer relationships and similarity theory for wall normal velocity and fluid temperature for convectively unstable flow were successfully recovered. Fluid temperature p.d.f.s in the log region are positively skewed, whereas in the conduction region pdfs are similar to Gaussian for purely convective and convectively unstable flows; for neutral flows the pdfs are Gaussian like irrespective of wall normal distances. Solid thermal properties and thickness only influence fluid temperature in the conduction region. Solids with larger thermal inertia homogenize the solid-fluid interfacial temperature through thermal diffusion and storage. Isothermal interfacial temperature with high heat flux variation results for smaller thermal activity ratio and isoflux case with high interfacial temperature variation results for larger thermal activity ratio. With a constant temperature boundary condition at the lower solid boundary, thin solids inhibit the imprint of large coherent structures on the interface, resulting in smaller interfacial temperature variations.

Future work for the numerical simulation will be to study the solid-fluid coupled heat transport process for higher Reynolds number flows, more comparable to the real world problems. Direct numerical simulation may not be feasible for these cases due to large computing cost, but wall resolved large eddy simulation model could be attempted instead.

Bibliography

Adrian RJ, 2007, Hairpin vortex organization in wall turbulence. *Phys. Fluids*, **19**, 041301.

Adrian RJ, Ferreira RTDS, & Boberg T, 1986, Turbulent thermal convection in wide horizontal fluid layers. *Exp. Fluids*, **4**, 121-141.

Ahlers G, Grossmann S, & Lohse D, 2009, Heat transfer and large scale dynamics in turbulent Rayleigh-Bénard convection, *Rev. Mod. Phys.*, **81**, 503-537.

Andreas EL, Hill RJ, Gosz JR, Moore DI, Otto WD, & Sarma AD, 1998, Statistics of surface-layer turbulence over terrain with meter-scale heterogeneity. *Boundary-Layer Meteorol.*. **86**, 379-408.

Armenio V, & Sarkar S, 2002, An investigation of stably stratified turbulent channel flow using large-eddy simulation. *J. Fluid Mech.*, **459**, 1-42.

Balick LK, Jeffery CA, & Henderson B, 2003, Turbulence induced spatial variation of surface temperature in high resolution thermal IR satellite imagery. *Proc. SPIE*, **4879**, 221-230.

Ballard JR, Smith JA, & Koenig GG, 2004, Towards a high temporal frequency grass canopy thermal IR model for background signatures. *Proc. SPIE*, **5431**.

Bastiaanssen WGM, Menenti M, Feddes RA, & Holtslag AAM, 1998a, A remote sensing surface energy balance algorithm for land (SEBAL) 1. Formulation. *J. Hydrol.*, **212-213**, 198-212.

Bastiaanssen WGM, Pelgrum H, Wang J, Ma Y, Moreno JF, Roerink GJ, Roebeling RA, & van der Wal T, 1998b, A remote sensing surface energy balance algorithm for land (SEBAL) 2. Validation. *J. Hydrol.*, **212-213**, 213-229.

Bernard PS, & Wallace JM, 2002, Turbulent flow: analysis, measurement and prediction. *John Wiley & Sons Inc.*, New Jersey, USA.

Braaten DA, Shaw RH, & Paw U KT, 1993, Boundary-layer flow structures associated with particle reentrainment. *Boundary-Layer Meteorol.*, **65**, 255-272.

Brutsaert W, 1975, A theory for local evaporation (or heat transfer) from rough and smooth surfaces at ground level. *Water Resour. Res.*, **11**, 543-550.

Businger JA, Wyngaard JC, Izumi Y, & Bradley EF, 1971, Flux-profile relationships in the atmospheric surface layer. *J. Atmos. Sci.*, **28**, 181-189.

Campbell GS, & Norman JM, 1998, An introduction to environmental biophysics. *Springer Verlag*, New York, USA, 286 pp.

Carslaw HS, & Jaeger JC, 1959, Conduction of heat in solids, *Oxford University Press*, London, UK.

Castellvi F, 2004, Combining surface renewal analysis and similarity theory: a new approach for estimating sensible heat flux. *Water Resour. Res.*, **40**, W05201.

Castellvi F, Perez PJ, & Ibanez M, 2002, A method based on high-frequency temperature measurements to estimate the sensible heat flux avoiding the height dependence. *Water Resour. Res.*, **38**, 20(1-9).

Castellvi F, & Snyder RL, 2009, Combining the dissipation method and surface renewal analysis to estimate scalar fluxes from the time traces over rangeland grass near Ione (California). *Hydrol. Process.*, **23**, 842-857.

Caughey SJ, & Palmer SG, 1979, Some aspects of turbulence structure through the depth of the convective boundary layer. *Quart. J. R. Meteorol. Soc.*, **105**, 811-827.

Christen A, Meier F, & Scherer D, 2012, High-frequency fluctuations of surface temperatures in an urban environment. *Theor. Appl. Climatol.*, **108**, 301-324.

Christen A, & Voogt JA, 2009, Linking atmospheric turbulence and surface temperature fluctuations in a street canyon. Paper no. A3-6. *The 7th International Conference on Urban Climate*, Yokohoma, Japan.

Christen A, & Voogt JA, 2010, Inferring turbulent exchange process in an urban street canyon from high-frequency thermography. Paper no. J3A.3. *9th Symposium on the Urban Environment*, Keystone, Colorado, USA.

Cohn SA, Mayor SD, Grund CJ, Weckwerth TM, & Senff C, 1988, The lidars in flat terrain (LIFT) experiment. *Bull. Amer. Meteorol. Soc.*, **79**, 1329-1343.

Corino ER, & Brokey RS, 1969, A visual investigation of the wall region in turbulent flow. *J. Fluid Mech.*, **37**, 1-30.

Deardorff JW, 1970, Convective velocity and temperature scales for the unsteady planetary boundary layer and for Rayleigh convection, *J. Atmos. Sci.*, **27**, 1211-1213.

Deardorff JW, 1972, Numerical investigation of neutral and unstable planetary boundary lyers. *J. Atmos. Sci.*, **29**, 91-115.

Deardorff JW, 1980, Stratocumulus-capped mixed layers derived from a three-dimensional model. *Boundary-Layer Meteorol.*, **18**, 495-527.

Deardorff JW, Willis GE, & Lilly DK, 1969, Laboratory investigation of non-steady penetrative convection. *J. Fluid Mech.*, **35**, 7-31.

Deardorff JW, & Willis GE, 1985, Further results from a laboratory model of the convective planetary boundary layer, *Boundary-Layer Meteorol.*, **32**, 205-236.

De Bruin HAR, Kohsiek W, & Van Den Hurk JJM, 1993, A verification of some methods to determine the fluxes of momentum, sensible heat, and water vapour using standard deviation and structure parameter of scalar meteorological quantities. *Boundary-Layer Meteorol.*, **63**, 231-257.

Derksen DS, 1974, Thermal infrared pictures and the mapping of microclimate. *Neth. J. Agric. Sci.*, **22**, 119-132.

Drobinski P, Brown RA, Flamant PH, & Pelon J, 1998, Evidance of organized large eddies by ground based Doppler lidar, sonic anemometer and sodar. *Boundary-Layer Meteorol.*, **88**, 343-361.

Dyer AJ, 1974, A review of flux-profile relationships. *Boundary-Layer Meteorol.*, **7**, 363-372.

Etling D, & Brown RA, 1993, Roll vortices in the planetary boundary layer: a review. *Boundary-Layer Meteorol.*, **65**, 215-248.

Finnigan JJ, 2010, Waving plants and turbulent eddies. *J. Fluid Mech.*, **652**, 1-4.

Foken T, Wimmer F, Mauder M, Thomas C, & Liebethal C, 2006, Some aspects of the energy balance closure problem. *Atmos. Chem. Phys.*, **6**, 4395-4402.

Gao W, Shaw RH, & Paw U KT, 1989, Observation of organized structure in turbulent flow within and above a forest canopy. *Boundary-Layer Meteorol.*, **47**, 349-377.

Garai A, & Kleissl J, 2011, Air and surface temperature coupling in the convective atmospheric boundary layer. *J. Atmos. Sci.*, **68**, 2945-2954.

Garai A, & Kleissl J, 2013, Interaction between coherent structures and surface temperature and its effect on ground heat flux in an unstably stratified boundary layer. *J. Turbul.* (in press).

Garai A, Kleissl J, & Llewellyn Smith SG, 2010, Estimation of biomass heat storage using thermal infrared imagery: application to a walnut orchard. *Boundary-Layer Meteorol.*, **137**, 333-342.

Garai A, Pardyjak E, Steenveld G-J, & Kleissl J, 2013, Surface temperature and surface layer turbulence in a convective boundary layer. *Boundary-Layer Meteorol.*, **148**, 51-72.

Garai A, Kleissl J, & Sarkar S, 2013, Heat transfer in a convectively unstable turbulent channel flow with solid conduction. *J. Fluid Mech.*, under review.

Glendening JW, 1996, Lineal eddy features under strong shear conditions. *J. Atmos. Sci.*, **53**, 3430-3449.

Gurka R, Liberzon A, & Hetsroni G, 2004, Detecting coherent patterns in a flume by using piv and ir imaging technique. *Expt. Fluids*, **37**, 230-236.

Head MR, & Bandyopadhyay P, 1981, New aspects of turbulent boundary-layer structure. *J. Fluid Mech.*, **107**, 297-338.

Hetsroni G, Kowalewski TR, Hu B, & Mosyak A, 2001, Tracking of coherent thermal structures on a heated wall by means of infrared thermography. *Expt. Fluids*, **30**, 286-294.

Hetsroni G, & Rozenblit R, 1994, Heat transfer to a liquid-solid mixture in a flume. *Int. J. Multiphase Flow*, **20**, 671-689.

Högström ULF, 1988, Non-dimensional wind and temperature profiles in the atmospheric surface layer: a re-evaluation. *Boundary-Layer Meteorology*, **42**, 55-78.

Hommema SE, & Adrian RJ, 2003, Packet structure of surface eddies in the atmospheric boundary layer. *Boundary-Layer Meteorol*, **106**, 147-170.

Howard LN, 1966, Convection at high Rayleigh number. *Proc. 11th Int. Cong. Appl. Mech.*, Berlin, Germany.

Hsieh C-I, Katul G, & Chi T, 2000, An approximate analytical model for footprint estimation of scalar fluxes in thermally stratified atmospheric flows. *Adv. Water Resour.*, **23**, 765-772.

Hudgins L, Friehe CA, & Mayer ME, 1993, Wavelet transforms and atmospheric turbulence. *Phys. Rev. Lett.*, **71**, 3279-3282.

Hunt JCR, Vrieling AJ, Nieuwstadt FTM, & Fernando HJS, 2003, The influence of the thermal diffusivity of the lower boundary on eddy motion in convection. *J. Fluid Mech.*, **491**, 183-205.

Inagaki A, Kanda M, Onomura S, & Kumemura H, 2013, Thermal image velocimetry. *Boundary-Layer Meteorol.*, DOI 10.1007/s10546-013-9832-z.

Jayalakshmy MS, & Philip J, 2010, Thermophysical properties of plant leaves and their influence on the environment temperature. *Int. J Thermophys.*, **31**, 2295-2304.

Jiménez J, 2012, Cascade in wall-bounded turbulence. *Annu. Rev. Fluid Mech.* **44**, 27-45.

Johansson AV, & Wikström PM, 1999, DNS and modelling of passive scalar transport in turbulent channel flow with a focus on scalar dissipation rate modelling. *Flow Turbul. Combust.*, **63**, 223-245.

Kader BA, 1981, Temperature and concentration profiles in fully turbulent boundary layers. *Int. J. Heat Mass Transfer*, **24**, 1541-1544.

Kaimal JC, 1978, Horizontal velocity spectra in an unstable surface layer. *J. Atmos. Sci.*, **35**, 18-24.

Kaimal JC, & Businger JA, 1970, Case studies of a convective plume and a dust devil. *J. Appl. Meteorol.*, **9**, 612-620.

Kaimal JC, Wyngaard JC, Haugen DA, Cote OR, & Izumi Y, 1976, Turbulence structure in the convective boundary layer. *J. Atmos. Sci.*, **33**, 2152-2169.

Katul GG, Albertson JD, Hsieh C-I, Conklin PS, Sigmon JT, Parlange MB, & Knoerr KR, 1996, The “inactive” eddy motion and the large scale turbulent pressure fluctuations in the dynamic sublayer. *J. Atmos. Sci.*, **53**, 2512-2524.

Katul GG, Konings AG, & Porporato A, 2011, Mean velocity profile in a sheared and thermally stratified atmospheric boundary layer. *Phys Rev Lett*, **107**, 268502.

Katul GG, Schieldge J, Hsieh C-I, & Vidakovic B, 1998, Skin temperature perturbations induced by surface layer turbulence above a grass surface. *Water Resour. Res.*, **34**, 1265-1274.

Khanna S, & Brasseur JG, 1998, Three-dimensional buoyancy- and shear-induced local structure of the atmospheric boundary layer. *J. Atmos. Sci.*, **55**, 710-743.

Kim J, Moin P, & Moser R, 1987, Turbulence statistics in fully developed channel flow at low Reynolds number. *J. Fluid Mech.*, **177**, 133-136.

Kline SJ, Reynolds WC, Schraub FA, & Runstadler PW, 1967, The structure of turbulent boundary layers. *J. Fluid Mech.*, **30**, 741-773.

Kormann R, Meixner FX, 2001, An analytical footprint model for non-neutral stratification. *Boundary-Layer Meteorol.*, **99**, 207-224.

Kowalewski TA, Hetsroni G, Hu B, & Mosyak A, 2000, Tracking of thermal structures from infrared camera by piv method. Paper no. 131, *9th International Symposium on Flow Visualization*, Edinburgh, United Kingdom.

Kowalewski TA, Mosyak A, & Hetsroni G, 2003, Tracking of coherent thermal structures on a heated wall. 2. DNS simulation. *Expt. Fluids*, **34**, 390-396.

Kustas WP, Prueger JH, & Hipps LE, 2002, Impact of using different time-averaged inputs for estimating sensible heat flux of riparian vegetation using radiometric surface temperature. *J. Appl. Meteorol.*, **41**, 319-332.

LeMone MA, 1973, The structure and dynamics of horizontal roll vortices in the planetary boundary layer. *J. Atmos. Sci.*, **30**, 1077-1091.

LeMone MA, 1976, Modulation of turbulence energy by longitudinal rolls in an unstable planetary boundary layer. *J. Atmos. Sci.*, **33**, 1308-1320.

Lenschow DH, & Boba Stankov B, 1986, Length scales in the convective boundary layer. *J. Atmos. Sci.*, **43**, 1198-1209.

Lenschow DH, Wyngaard JC, & Pennell WT, 1980, Mean-field and second-moment budgets in a baroclinic convective boundary layer. *J. Atmos. Sci.*, **37**, 1313-1326.

Li D, & Bou-Zeid E, 2011, Coherent structures and the dissimilarity of turbulent transport of momentum and scalars in the unstable atmospheric surface layer. *Boundary-Layer Meteorol.*, **140**, 243-262.

Lida O, & Kasagi N, 1997, Direct numerical simulation of unstably stratified turbulent channel flow. *J. Heat Transfer*, **119**, 53-61.

Lilly DK, 1967, The representation of small-scale turbulence in numerical simulation experiments. *Proc. IBM Sci. Computing Symp. Environmental Sci.*

Lin C-L, 2000, Local pressure-transport structure in a convective atmospheric boundary layer. *Phys. Fluids*, **12**, 1112-1128.

Liu L, Hu F, & Cheng X-L, 2011, Probability density functions of turbulent velocity and temperature fluctuations in the unstable atmospheric surface layer. *J. Geophys. Res.*, **116**, D12117.

Liu WT, & Businger JA, 1975, Temperature profile in the molecular sublayer near the interface of a fluid in turbulent motion. *Geophys. Res. Lett.*, **2**, 403-404.

Liu X, Tsukamoto O, Oikawa T, & Ohtaki E, 1998, A study of correlations of scalar quantities in the atmospheric surface layer. *Boundary-Layer Meteorol.*, **87**, 499-508.

Lohse D, & Xia K-Q, 2010, Small-scale properties of turbulent Rayleigh-Bénard convection. *Annu. Rev. Fluid Mech.*, **42**, 335-364.

Lothon M, Lenschow DH, & Mayor SD, 2006, Coherence and scale of vertical velocity in the convective boundary layer from a Doppler lidar. *Boundary-Layer Meteorol.*, **121**, 521-536.

Lothon M, Lohou F, Durand P, Couvreux Sr. F, Hartogensis OK, Legain D, Pardyjak E, Pino D, Reuder J, Vilà Guerau de Arellano J, Alexander D, Augustin P, Bazile E, Bezombes Y, Blay E, van de Boer A, Boichard JL, de Coster O, Cuxart J, Dabas A, Darbieu C, Deboudt K, Delbarre H, Derrien S, Faloona I, Flament P, Fourmentin M, Garai A, Gibert F, Gioli B, Graf A, Groebner J, Guichard F, Jonassen M, van de Kroonenberg A, Lenschow D, Martin S, Martinez D, Mastrorillo L, Moene A, Moulin E, Pietersen H, Piguet B, Pique E, Román-Cascón C, Said F, Sastre M, Seity Y, Steeneveld G-J, Toscano P, Traullé O, Tzanos D, Wacker S, & Yagüe C, 2012, The boundary layer late afternoon and sunset turbulence 2011 filed experiment. Paper no. 14B.1, *The 20th Symposium on Boundary Layers and Turbulence*, Boston, Massachusetts, USA.

Mahrt L, 1991, Eddy asymmetry in the sheared heated boundary layer. *J. Atmos. Sci.*, **48**, 472-492.

Mason PJ, 1989, Large-eddy simulation of the convective atmospheric boundary layer. *J. Atmos. Sci.*, **46**, 1492-1516.

Meneveau C, & Katz J, 2000, Scale-invariance and turbulence models for large-eddy simulation. *Annu. Rev. Fluid Mech.*, **32**, 1-32.

Moeng C-H, 1984, A large-eddy-simulation model for the study of planetary boundary layer turbulence. *J. Atmos. Sci.*, **41**, 2052-2062.

Moeng C-H, & Sullivan PP, 1994, A comparison of shear- and buoyancy-driven planetary boundary layer flows. *J. Atmos. Sci.*, **51**, 999-1022.

Moeng C-H, & Wyngaard JC, 1988, Spectral analysis of large-eddy simulations of the convective boundary layer. *J. Atmos. Sci.*, **45**, 3573-3587.

Monin AS, & Obukhov AM, 1954, Basic laws of turbulent mixing in the surface layer of the atmosphere. *Tr. Akad. Nauk SSSR Geophiz. Inst.*, **24**, 163-187.

Morinishi Y, Tamano S, & Nakamura E, 2007, New scaling of turbulence statistics for incompressible thermal channel flow with different total heat flux gradients. *Int. J. Heat Mass Transfer*, **50**, 1781-1789.

Moser RD, Kim J, & Mansour NN, 1999, Direct numerical simulation of turbulent channel flow up to $Re_\tau = 590$. *Phys. Fluids*, **11**, 943-945.

Nieuwstadt FTM, Mason PJ, Moeng C-H, & Schumann U, 1991, Large-eddy simulation of the convective boundary layer: a comparison of four computer codes. *8th Symp. Turbulent Shear Flow*.

Oke TR, 1987, Boundary layer climates. *Methuen*, London, UK, 435 pp.

Paulson CA, 1970, The mathematical representation of wind speed and temperature profiles in the unstable atmospheric surface layer. *J. Appl. Meteorol.*, **9**, 857-861.

Paw U KT, Brunet Y, Collineau S, Shaw RH, Maitani T, Qiu J, & Hipps L, 1992, On coherent structures in turbulence above and within agricultural plant canopies. *Agric. For. Meteorol.*, **61**, 55-68.

Paw U KT, Qiu J, Su HB, Watanabe T, & Brunet Y, 1995, Surface renewal analysis: a new method to obtain scalar fluxes. *Agric. For. Meteorol.*, **74**, 119-137.

Pierce B, Moin P, & Sayadi T, 2013, Application of vortex identification schemes to direct numerical simulation data of a transitional boundary layer. *Phys. Fluids.*, **25**, 015102.

Pope SB, 2000, Turbulent Flows. *Cambridge University Press*, New York, USA.

Raasch S, & Etling D, 1991, Numerical simulation of rotating turbulent thermal convection. *Beitr. Phys. Atmosph.*, **64**, 185-199.

Ramana MV, Krishnan P, & Kunhikrishnan PK, 2004, Surface boundary-layer characteristics over a tropical inland station: seasonal features. *Boundary-Layer Meteorol.*, **111**, 153-175.

Raupach MR, Finnigan JJ, & Brunet Y, 1996, Coherent eddies and turbulence in vegetation canopies: the mixing-layer analogy. *Boundary-Layer Meteorol.*, **78**, 351-382.

Renno NO, Abreu VJ, Koch J, Smith PH, Hartogensis OK, De Bruin HAR, Burose D, Delory GT, Farrell M, Watts CJ, Garatuza J, Parker M, & Carswell A, 2004, MATADOR 2002: A pilot field experiment on convective plumes and dust devils. *J. Geophys. Res.*, **107**, E07001.

Schmidt H, & Schumann U, 1989, Coherent structure of the convective boundary layer derived from large-eedy simulations. *J. Fluid Mech.*, **200**, 511-562.

Schols JLJ, 1984, The detection and measurement of turbulent structures in the atmospheric surface layer. *Boundary-Layer Meteorol.*, **29**, 39-58.

Schols JLJ, Jansen AE, & Krom JG, 1985, Characteristics of turbulent structures in the unstable atmospheric surface layer. *Boundary-Layer Meteorol.*, **33**, 173-196.

Shishkina O, Stevens RJAM, Grossmann S, & Lohse D, 2010, Boundary layer structure in turbulent thermal convection and its consequences for the required numerical resolution. *New J. Phys.*, **12**, 075022.

Smagorinsky J, 1963, General circulation experiments with the primitive equations I. the basic experiment. *Mon. Wea. Rev.*, **91**, 99-164.

Snyder RL, Spano D, & Paw U KT, 1996, Surface renewal analysis for sensible and latent heat flux density. *Boundary-Layer Meteorol.*, **77**, 249-266.

Spano D, Snyder RL, Duce P, & Paw U KT, 1997, Surface renewal analysis for sensible heat flux density using structure functions. *Agric. For. Meteorol.*, **86**, 259-271.

Spano D, Snyder RL, Duce P, & Paw U KT, 2000, Estimating sensible and latent heat flux densities from grapevine canopies using surface renewal. *Agric. For. Meteorol.*, **104**, 171-183.

Sparrow EM, Husar RB, & Goldstein RJ, 1970, Observation and other characteristics of thermals. *J. Fluid Mech.*, **41**, 793-800.

Stull RB, 1997, An introduction to boundary layer meteorology. *Kluwer Academic Publishers*, USA.

Sykes RI, & Henn DS, 1989, Large-eddy simulation of turbulent sheared convection. *J. Atmos. Sci.*, **46**, 1106-1118.

Tampieri F, Maurizi A, & Viola A, 2009, An investigation on temperature variance scaling in the atmospheric surface layer. *Boundary-Layer Meteorol.*, **132**, 31-42.

Taylor RJ, 1958, Thermal structures in the lowest layers of the atmosphere. *Austr. J. Phys.*, **11**, 168-176.

Thomas DB, & Townsend AA, 1957, Turbulent convection over a heated horizontal surface. *J. Fluid Mech.*, **2**, 473-492.

Tiselj I, Bergant R, Makov B, Bajsić I, & Hestroni G, 2001, DNS of turbulent heat transfer in channel flow with heat conduction in the solid wall. *J. Heat Transfer*, **123**, 849-857.

Townsend AA, 1959, Temperature fluctuation over a heated horizontal surface. *Fluid Mech.*, **5**, 209-241.

Townsend AA, 1961, Equilibrium layers and wall turbulence. *J. Fluid Mech.*, **11**, 97-120.

Verzicco R, & Sreenivasan KR, 2008, A comparison of turbulent thermal convection between conditions of constant temperature and constant heat flux. *J. Fluid Mech.*, **595**, 203-219.

Vogt R, 2008, Visualisation of turbulent exchange using a thermal camera. Paper no. 8B.1. *18th Symposium on Boundary Layer and Turbulence*, Stockholm, Sweden.

Wicker LJ, & Skamarock WC, 2002, Time-splitting methods for elastic models using forward time schemes. *Mon. Wea. Rev.*, **130**, 2088-2097.

Wilczak JM, & Businger JA, 1983, Thermally indirect motions in the convective atmospheric boundary layer. *J. Atmos. Sci.*, **40**, 343-358.

Wilczak JM, Oncley SP, & Stage SA, 2001, Sonic anemometer tilt correction algorithms. *Boundary-Layer Meteorol.*, **99**, 127-150.

Wilczak JM, & Tillman JE, 1980, The three-dimensional structure of convection in the atmospheric surface layer. *J. Atmos. Sci.*, **37**, 2424-2443.

William AG, & Hacker JM, 1993, Interactions between coherent eddies in the lower convective boundary layer. *Boundary-Layer Meteorol.*, **64**, 55-74.

Williamson JH, 1980, Low storage Runge-Kutta schemes. *J. Comput. Phys.*, **35**, 48-56.

Willis GE, & Deardorff JW, 1974, A laboratory model of the unstable planetary boundary layer, *J. Atmos. Sci.*, **31**, 1297-1307.

Willis GE, & Deardorff JW, 1979, Laboratory observation of turbulent penetrative-convection planforms, *J. Geophys. Res.*, **84**, 295-302.

Wilson DK, 1996, Empirical orthogonal function analysis of the weakly convective atmospheric boundary layer. Part I: eddy structure. *J. Atmos. Sci.*, **53**, 801-823.

Wilson DK, & Wyngaard JC, 1996, Empirical orthogonal function analysis of the weakly convective atmospheric boundary layer. Part II: eddy energetic. *J. Amos. Sci.*, **53**, 824-841.

Wyngaard JC, Coté OR, & Izumi Y, 1971, Local free convection, similarity and the budgets of shear stress and heat flux. *J. Atmos. Sci.*, **28**, 1171-1182.

Young GS, 1987, Mixed layer spectra from aircraft measurements. *J. Atmos. Sci.*, **44**, 1251-1256.

Young GS, 1988a, Turbulence structure of the convective boundary layer. Part I: Variability of normalized turbulence statistics. *J. Atmos. Sci.*, **45**, 712-719.

Young GS, 1988b, Turbulence structure of the convective boundary layer. Part II: Phoenix 78 aircraft observations of thermals and their environment. *J. Atmos. Sci.*, **45**, 727-735.

Young GS, 1988c, Convection in the atmospheric boundary layer. *Earth Sci. Rev.*, **25**, 179-198.

Young GS, Kristovich DAR, Hjelmfelt MR, & Foster RC, 2002, Rolls, streets, waves and more: a review of quasi-two-dimensional structures in the atmospheric boundary layer. *Bull. Amer. Meteorol. Soc.*, **83**, 997-1001.

Zhou J, Adrian RJ, Balachandar S, & Kendall TM, 1999, Mechanisms for generating coherent packets of hairpin vortices in channel flow. *J. Fluid Mech.*, **387**, 353-396.